FERMILAB-PUB-15-646-APC
ACCEPTED

Beam Instabilities

E. Métral, T. Argyropoulos, H. Bartosik, N. Biancacci, X. Buffat, J. F. Esteban Muller, W. Herr, G. Iadarola, A. Lasheen, K. Li, T. Pieloni, D. Quartullo, G. Rumolo, B. Salvant, E. Shaposhnikova, C. Tambasco, H. Timko, C. Zannini, (CERN, Geneva, Switzerland), A. Burov (FNAL, Chicago, USA), D. Banfi, J. Barranco, N. Mounet, (EPFL, Lausanne, Switzerland), O. Boine-Frankenheim (GSI and TUD, Darmstadt, Germany), U. Niedermayer (TUD, Darmstadt, Germany), V. Kornilov (GSI, Darmstadt, Germany) and S. White (ESRF, Grenoble, France)

***Abstract*—Beam instabilities cover a wide range of effects in particle accelerators and they have been the subject of intense research for several decades. As the machines performance was pushed new mechanisms were revealed and nowadays the challenge consists in studying the interplays between all this intricate phenomena, as it is very often not possible to treat the different effects separately. The aim of this paper is to review the main mechanisms, discussing in particular the recent developments of beam instability theories and simulations.**

***Index Terms*—Beam coupling impedance, wake field, coherent instability, Landau damping, chromaticity, transverse damper/feedback, octupoles, stability diagram, electron cloud, beam-beam, space charge.**

I. INTRODUCTION

As the beam intensity increases, the beam can no longer be considered as a collection of non-interacting single particles: in addition to the "single-particle phenomena", "collective effects" become significant [1,2]. At low intensity a beam of charged particles moves around an accelerator under the Lorentz force produced by the "external" electromagnetic fields (from the guiding and focusing magnets, RF cavities, etc.). However, the charged particles also interact with themselves (leading to space charge effects) and with their environment, inducing charges and currents in the surrounding structures, which create electromagnetic fields called wake fields. In the ultra-relativistic limit, causality dictates that there can be no electromagnetic field in front of the beam, which explains the term "wake". It is often useful to examine the frequency content of the wake field (a time domain quantity) by performing a Fourier transformation on it. This leads to the concept of impedance (a frequency domain quantity), which is a complex function of frequency. The charged particles can also interact with other charged particles present in the accelerator (leading to two-stream effects, and in particular to electron cloud effects in positron/hadron machines) and with the counter-rotating beam in a collider (leading to beam-beam effects). As the beam intensity increases, all these "perturbations" should be properly quantified and the motion of the charged particles will eventually still be governed by the Lorentz force but using the total electromagnetic fields, which are the sum of the external and perturbation fields. Note that in some cases a perturbative treatment is not sufficient and the problem has to be solved self consistently. These perturbations can lead to both incoherent (i.e. of a single particle) and coherent (i.e. of the centre of mass) effects, in the longitudinal and in one or both transverse directions, leading to beam quality degradation or even partial or total beam losses. Fortunately, stabilizing mechanisms exist, such as Landau damping, electronic feedback systems and linear coupling between the transverse planes (as in the case of a transverse coherent instability, one plane is usually more critical than the other).

The first collective effect is space charge. In fact, two space charge effects are distinguished: the direct space charge and the indirect (or image) one [1-5 and references therein]. The direct space charge comes from the interaction between the particles of a single beam, without interaction with the surrounding vacuum chamber. Consider two particles with the same charge (for instance protons) in vacuum. They will feel two forces: the Coulomb repulsion (as they have the same charge) and the magnetic attraction (as they represent currents moving in the same direction, leading to an azimuthal magnetic field). Let's assume that a particle (1) is moving with some speed (smaller than the speed of light) with respect to the laboratory frame. In its rest frame, the particle produces only an electrostatic field, which can be computed, and applying the relativistic transformation of the electromagnetic fields between the rest and laboratory frames, the magnetic contribution can be obtained. Note that there is no magnetic contribution in the longitudinal plane, which means that the longitudinal Lorentz force is equal to the elementary charge times the longitudinal electric field. The transverse (horizontal and vertical) Lorentz force on a second particle (2), moving with a different speed with respect to the laboratory frame, is written

$$F_{x,y} = e\, E_{x,y} \left| \begin{array}{ll} \left(1-\beta_1\,\beta_2\right) & , \quad \text{if 2 moves in same direction as 1} \\ \left(1+\beta_1\,\beta_2\right) & , \quad \text{if 2 moves in oppo. direction as 1} \end{array} \right. , \tag{1}$$

where e is the elementary charge, E the electric field and β the relativistic velocity factor. The first case corresponds to the space charge case where both particles move in the same

Date on which I submitted this paper for review: 16/06/2015.
Email: Elias.Metral@cern.ch.

Operated by Fermi Research Alliance, LLC under Contract No. De-AC02-07CH11359 with the United States Department of Energy.

direction, while the second corresponds to the beam-beam case (in a collider) where the particles move in opposite direction. In both cases, the first term comes from the electric field while the second comes from the magnetic one. The main difference between the two regimes is that for the space charge case there is a partial compensation of the two forces, while for the beam-beam case the two forces add. The space charge force is maximum at low energy and vanishes at high energy, while the beam-beam force is maximum at high energy. Considering a bunch of particles (in the space charge regime, and e.g. Gaussian in the three dirrections), it can be seen that the space charge forces are highly nonlinear and that the radial force is proportional to the longitudinal density while the longitudinal one is proportional to the derivative of the longitudinal density. The transverse space charge force is linear for small amplitudes and always defocusing, leading to negative betatron tune shifts and a global tune spread (plotted in the tune diagram it is called a tune footprint), as all the particles do not have the same tune shift (the maximum space charge tune shift is obtained for the small amplitudes). The transverse betatron and longitudinal synchrotron linearized incoherent space charge tune shifts are given by (with the assumptions made before, assuming also a round beam for simplicity)

$$\Delta Q_t^{\mathrm{Lin}} = -\frac{N_b \, r_p}{4\pi \beta \gamma^2 \varepsilon_{tn} B},$$

$$\Delta Q_s^{\mathrm{Lin}} = \frac{\eta \, N_b \, e^2 \, R^2}{8\pi\sqrt{2\pi}\, \varepsilon_0 \, E_{total} \, \beta^2 \gamma^2 \sigma_s^3 \, Q_{s0}} \left[1 + 2\ln\left(\frac{b}{\sqrt{2}\,\sigma_t} \right) \right], \tag{2}$$

where N_b is the number of protons in the bunch, r_p the classical proton radius, ε_{tn} the transverse normalized rms emittance, γ the relativistic mass factor, B the bunching factor (equal to 1 in the case of a debunched beam), R the average machine radius, ε_0 the permittivity of vacuum, E_{total} the total particles' energy, σ_s the rms longitudinal bunch size, Q_{s0} the unperturbed (low-intensity) synchrotron tune, b the surrounding beam pipe radius, σ_t the rms transverse bunch size, and η the slip factor (describing the distance to the transition energy), given by (with α_p the momentum compaction factor)

$$\eta = \alpha_p - \frac{1}{\gamma^2} = \frac{1}{\gamma_{tr}^2} - \frac{1}{\gamma^2}. \tag{3}$$

The direct space charge alone cannot drive the beam unstable but as will be seen later its effect on beam instabilities can be important and this is still a subject of intense research. Contrary to the transverse case, the longitudinal space charge is defocusing (which reduces the bucket height and increases the bunch length) below transition and focusing (which increases the bucket height and reduces the bunch length) above. Therefore, there is an intensity-dependent step in the equilibrium bunch length at transition, which leads to a longitudinal mismatch and subsequent quadrupolar oscillations. If these bunch shape oscillations are not damped they will eventually result in filamentation and longitudinal emittance blow-up. Crossing transition (or working close to transition) makes the beam very sensitive to beam instabilities as will be discussed later, and this is why transition is usually avoided in the new accelerator designs.

The second space charge effect is the indirect space charge. In the case of a beam off-axis in a perfectly conducting circular beam pipe, a coherent (or dipolar, i.e. of the centre of mass) force arises, which can be found by using the method of the images (to satisfy the boundary condition on a perfect conductor, i.e. of a vanishing tangential electrical field). The electric field is always assumed to be non-penetrating. However, for the magnetic field, the situation is more complicated as it may or may not penetrate the vacuum chamber: the high-frequency components, called "ac" will not penetrate, while the low-frequency ones, called "dc" will penetrate and form images on the magnet pole faces (if there are some; otherwise they will go to infinity and will not act back on the beam). This leads to transverse forces, which are linear (for small displacement in the beam pipe) with the transverse displacements of the centre of mass and with a coefficient, which is similar to the transverse incoherent term. The same analysis can be performed for instance in the case of two infinite (horizontal) parallel plates. Compared to the circular case, the coherent force is smaller by $\pi^2/24$ in the horizontal plane and $\pi^2/12$ in the vertical one. Furthermore, in the case of asymmetric chambers, there is a second incoherent (or quadrupolar, as it is linear with the particle position) term with opposite sign in both planes. The coefficients are linked to the Laslett coefficients usually used in the literature [6], and they are the same as the ones obtained by Yokoya [7] in the case of a resistive beam pipe under some assumptions (see the section on impedance below). General formulae exist for the real tune shifts of coasting or bunched beams in pipes with different geometries, considering both the ac and dc magnetic parts and can be found for instance in Refs. [4,5]. The important point here is that the indirect space charge alone cannot drive the beam unstable as it leads only to real tune shifts. To drive a beam unstable one needs something, which can lead to an "imaginary tune shift" as we are looking for coherent motions proportional to

$$e^{j\omega_c t} = e^{j(\omega_R + j\omega_i)t} = e^{j\omega_R t} \, e^{\frac{t}{\tau}}, \tag{4}$$

where j is the imaginary unit, t the time, ω_c the coherent betatron (angular) frequency and τ the beam instability rise-time. This is the case with impedances, which appear if the surrounding beam pipe is not perfectly conducting and smooth. If the wall of the beam pipe is perfectly conducting and smooth, as it was the case discussed above, a ring of negative charges (for positive charges travelling inside) is formed on the walls of the beam pipe where the electric field ends, and these induced charges travel at the same pace with the particles, creating the so-called image (or induced) current, which leads to real tune shifts as discussed before. But, if the wall of the beam pipe is not perfectly conducting or contains discontinuities, the movement of the induced charges will be slowed down, thus leaving electromagnetic fields (which are proportional to the beam intensity) mainly behind. The latter will create complex tune shifts leading to beam instabilities.

This paper is structured as follows: Section II reviews the recent progress in the beam-coupling impedance computations, simulations and (bench-) measurements while Section III discusses the beam instability theories and simulations. In Section IV, comparisons between theory, simulations and beam-based measurements are analysed for two CERN accelerators. The recent developments in beam instabilities are then discussed in Section V where several important mechanisms have been included in the analysis, such as (i) transverse damper, (ii) space charge, (iii) beam-beam and (iv) electron cloud. Section VI concludes this paper.

II. BEAM-COUPLING IMPEDANCE

What needs to be computed are the wake fields at a distance z behind a source particle and their effects on the test or witness particles that compose the beam. The computation of these wake fields is quite involved and two fundamental approximations are generally introduced: (i) the rigid-beam approximation (the beam traverses a piece of equipment rigidly, i.e. the wake field perturbation does not affect the motion of the beam during the traversal of the impedance. The distance of the test particle behind some source particle does not change) and (ii) the impulse approximation (as the test particle moves at a fixed velocity through a piece of equipment, the important quantity is the impulse, i.e. the integrated force, and not the force itself). Starting from the four Maxwell equations for a particle in the beam and taking the rotational of the impulse, it can be shown that for a constant β (which does not need to be 1)

$$\vec{\nabla} \times \Delta \vec{p}\left(x,y,z \right) = 0,$$

(5)

which is known as Panofsky-Wenzel theorem. This relation is very general, as no boundary conditions have been imposed. Only the two fundamental approximations have been made. Another important relation can be obtained when β is equal to 1 (taking the divergence of the impulse), which is

$$\vec{\nabla}_{\perp} \cdot \Delta \vec{p}_{\perp} = 0. \qquad (6)$$

Considering the case of a cylindrically symmetric chamber (using the cylindrical coordinates r, θ, z) and as a source charge density (which can be decomposed in terms of multipole moments) a macro-particle of charge $Q = N_b\, e$ moving along the pipe (in the s-direction) with an offset $r = a$ in the θ direction and with velocity $\upsilon = \beta\, c$ (with c the speed of light), the whole solution can be written, for $\beta = 1$ (with q the charge of the test particle and L the length of the structure)

$$\begin{aligned}
\upsilon \Delta p_s\left(r,\theta,z \right) &= \int_0^L F_s\, ds = -\, q\, Q\, a^m\, r^m \cos m\theta \;\; W'_m\left(z \right), \\
\upsilon \Delta p_r\left(r,\theta,z \right) &= \int_0^L F_r\, ds = -\, q\, Q\, a^m\, m r^{m-1} \cos m\theta \;\; W_m\left(z \right), \\
\upsilon \Delta p_\theta\left(r,\theta,z \right) &= \int_0^L F_\theta\, ds = q\, Q\, a^m\, m r^{m-1} \sin m\theta \;\; W_m\left(z \right).
\end{aligned} \qquad (7)$$

The function W_m is called the transverse ($\perp$) wake function and its derivative is called the longitudinal (//) wake function of azimuthal mode m. They describe the shock response (Green function) of the vacuum chamber environment to a $\delta-$function beam which carries an mth moment. The integrals (on the left) are called wake potentials (these are the convolutions of the wake functions with the beam distribution; here it is just a point charge). The Fourier transform of the wake function is called the impedance. The idea of representing the accelerator environment by an impedance was introduced by Sessler and Vaccaro [8]. As the conductivity, permittivity and permeability of a material depend in general on frequency, it is usually better (or easier) to treat the problem in the frequency domain, i.e. compute the impedance instead of the wake function. It is also easier to treat the case $\beta \neq 1$. Then, an inverse Fourier transform is applied to obtain the wake function in the time domain. Two important properties of impedances can be derived. The first is a consequence of the fact that the wake function is real, which leads to

$$\left[Z_m^{//}\left(\omega \right) \right]^* = Z_m^{//}\left(-\omega \right), \qquad -\left[Z_m^{\perp}\left(\omega \right) \right]^* = Z_m^{\perp}\left(-\omega \right), \qquad (8)$$

where $*$ stands for the complex conjugate and $\omega = 2\,\pi f$. The second is a consequence of Panofsky-Wenzel theorem (with the wave number $k = \omega\, /\, \upsilon$)

$$Z_m^{//}\left(\omega \right) = k\, Z_m^{\perp}\left(\omega \right). \qquad (9)$$

Another interesting property of the impedances is the directional symmetry (Lorentz reciprocity theorem): the same impedance is obtained from both sides if the entrance and exit are the same. In the case of a cavity, an equivalent RLC circuit can be used (with three parameters which are the longitudinal shunt impedance R_{sh}, the capacity and the inductance). In a real cavity, these three parameters cannot be separated easily and some other related parameters are used, which can be measured directly such as the resonance frequency f_r, the quality factor Q and the damping rate. When the quality factor is equal to 1, the resonator impedance is called "broad-band", and this model was extensively used in the past in many analytical computations. Finally, all the transverse impedances (dipolar or driving and quadrupolar or detuning) should be weighted by the betatron function at the location of the impedances, as this is what matters for the beam dynamics.

The situation is more involved in the case of non axi-symmetric structures (due in particular to the presence of the quadrupolar wake field, already discussed before) and for $\beta \neq 1$, as in this case some electromagnetic fields also appear in front of the source particle. In the case of axi-symmetric structures, a current density with some azimuthal Fourier component creates electromagnetic fields with the same azimuthal Fourier component. In the case of non axi-symmetric structures, a generalized notion of impedances was introduced by Tsutsui [9], where a current density with some azimuthal Fourier component may create an electromagnetic field with various different azimuthal Fourier components. If the source particle 1 and test particle 2 have the same charge, and in the ultra-relativistic case, the transverse wake potentials can be written (taking into account only the linear terms with respect to the source and test particles and neglecting the coupling terms) [10]

$$\begin{aligned} \int_0^L F_x \, ds &= -q^2 \left[\, x_1 \, W_x^{\text{driving}}\left(z \right) - x_2 \, W^{\text{detuning}}\left(z \right) \, \right], \\ \int_0^L F_y \, ds &= -q^2 \left[\, y_1 \, W_y^{\text{driving}}\left(z \right) + y_2 \, W^{\text{detuning}}\left(z \right) \, \right], \end{aligned} \tag{10}$$

where the driving term is used here instead of dipolar and detuning instead of quadrupolar (or incoherent). In the frequency domain, Eq. (10) leads to the following generalized impedances

$$\begin{aligned} Z_x \left[\, \Omega \, \right] &= x_1 \, Z_x^{\text{driving}} - x_2 \, Z^{\text{detuning}} \, , \\ Z_y \left[\, \Omega \, \right] &= y_1 \, Z_y^{\text{driving}} + y_2 \, Z^{\text{detuning}} \, . \end{aligned} \tag{11}$$

Note that in the case $\beta \neq 1$, another quadrupolar term is found [11] (see later). From Eqs. (10) and (11), the procedure to simulate or measure the driving and detuning contributions can be deduced. In the time domain, using some time-domain electromagnetic codes like for instance CST Particle Studio [12], the driving and detuning contributions can be disentangled. A first simulation with $x_2 = 0$ gives the driving part while a second one with $x_1 = 0$ provides the detuning part. It should be noted that if the simulation is done with $x_2 = x_1$, only the sum of the driving and detuning parts is obtained. The situation is more involved in the frequency domain, which is used for instance for impedance measurements on a bench [13]. Two measurement techniques can be used to disentangle the transverse driving and detuning impedances, which are both important for the beam dynamics (this can also be simulated with codes like Ansoft-HFSS [14]). The first uses two wires excited in opposite phase (to simulate a dipole), which yields the transverse driving impedance only. The second consists in measuring the longitudinal impedance, as a function of frequency, for different transverse offsets using a single displaced wire. The sum of the transverse driving and detuning impedances is then deduced applying the Panofsky-Wenzel theorem in the case of top/bottom and left/right symmetry [15]. Subtracting finally the transverse driving impedance from the sum of the transverse driving and detuning impedances obtained from the one-wire measurement yields the detuning impedance only. If there is no top/bottom or left/right symmetry the situation is more involved [16].

A. The New Regime Of The CERN LHC Collimators

Both longitudinal and transverse resistive-wall impedances were already calculated forty years ago by Laslett, Neil and Sessler [17]. However, a new physical regime was revealed by the LHC collimators (used to collimate the circulating beams and protect the machine from unwanted particle losses in cold areas). A small aperture paired with a large wall thickness asks for a different physical picture of the transverse resistive-wall effect from the classical one. The first unstable betatron line in the LHC is around 8 kHz (due to the very low revolution frequency f_0 = 11.245 kHz), where the skin depth for graphite (whose measured isotropic DC resistivity was ~ 10 μΩm) is 1.8 cm. It is smaller than the collimator thickness of 2.5 cm. Hence one could think that the resistive thick-wall formula would be about right. In fact it is not. The resistive impedance is about two orders of magnitude lower at this frequency, which was a very good news for the LHC. A number of papers have been published on this subject in the last few years using the field matching technique starting from the Maxwell equations and assuming a circular geometry [18-22]. Recently, new results have been also obtained for flat chambers, extending the (constant) Yokoya factors to frequency and material dependent ones [23] (see later), as was already found with some simplified kicker impedance models [24,25]. Note that the material resistivity may vary with the magnetic field through the magneto-resistance and the surface impedance can also increase due to the anomalous skin effect [26 and references therein].

Considering the simplest case (the general case will be discussed in the next sections) of an infinitely long smooth cylindrical collimator (even if in the LHC the many collimators used are composed of two parallel plates of finite length) with one layer extending up to infinity, a simple approximate formula can be derived for the "wall impedance" (and not the "resistive-wall impedance") in the interesting frequency range which lies between few kHz and few GHz for any "relatively" good conductor with real permeability and the permittivity of vacuum. It can be written as (up to a certain frequency which depends on β), for instance in the horizontal plane, [27]

$$Z_x^{\text{Wall}}\left(f \right) = \frac{j \, L \, Z_0}{2 \pi \, b^2 \, \beta \, \gamma^2} + \beta \, \frac{j \, L \, Z_0}{\pi \, b^2} \times \frac{1}{1 - \dfrac{x_2}{\mu_r} \times \dfrac{K_1'\left(x_2 \right)}{K_1\left(x_2 \right)}}, \tag{12}$$

with

$$x_2 = \left(1 + j \right) \frac{b}{\delta}, \qquad \delta = \sqrt{\frac{2}{\mu_0 \, \mu_r \, \sigma \, \omega}} \, , \tag{13}$$

where Z_0 is the vacuum impedance, δ the skin depth, μ_0 the permeability of vacuum, μ_r the relative permeability, $\sigma = 1 / \rho$ the electric conductivity and K is the modified Bessel function. Equation (12) can be simplified even further in the two limiting cases using the following equations

$$\frac{K_1'\left(x_2 \right)}{K_1\left(x_2 \right)} = \left| \begin{array}{ll} -\dfrac{1}{x_2} & \text{if } \left| x_2 \right| << 1 \\ -1 & \text{if } \left| x_2 \right| >> 1 \end{array} \right. . \tag{14}$$

When | x_2 | >> 1, the "classical thick-wall formula" is recovered (up to a certain frequency which depends on β)

$$Z_x^{\mathrm{Wall}}(f) = \frac{j\,L\,Z_0}{2\pi\,b^2\,\beta\gamma^2} + (1+j)\,\beta\,\frac{L\,Z_0\,\mu_r\,\delta}{2\,\pi\,b^3}, \tag{15}$$

where the first term describes the coherent part of the space charge impedance (from electric and ac magnetic images) and the second term is the classical thick-wall formula for the resistive-wall impedance.

When | x_2 | << 1, i.e. at very low frequency, the transverse wall impedance approaches a constant inductive value given by (assuming here $\mu_r = 1$)

$$Z_x^{\mathrm{Wall}}(f \to 0) = j\,\frac{L\,Z_0}{2\pi\beta\,b^2}, \tag{16}$$

as only electric images contribute (there are no ac magnetic images when f approaches 0). Note that the (broad) maximum of the real part of the transverse impedance is reached when Re [x_2] ≈ 1, i.e. $\delta \approx b$, which means (see Fig. 1)

$$f_{\max,\mathrm{Re}} \approx \frac{\rho}{b^2} \times \frac{1}{\pi\,\mu_0}. \tag{17}$$

In summary, even if the skin depth, at a certain frequency, is smaller than the wall thickness, this does not mean that we are in the classical thick-wall regime. Indeed, another parameter needs to be taken into account, which is the beam pipe radius. The latter needs also to be much larger than the skin depth to be in the classical thick-wall regime. Equation (17) reveals simply why the low-frequency regime becomes important for the LHC collimators, as the beam pipe radius can be as small as ~ 1 mm (instead of few cm usually) and the resistivity of graphite is much higher than the resistivity of stainless steel or copper. Figure 1 shows the case with b = 2 mm, ρ = 10 μΩm, L = 1, μ_r = 1 and β = 1. It clearly reveals the two regimes discussed above. Furthermore, it shows that a coating (see also below) with a good conductor (usually copper), which helps in the classical thick-wall regime, does not help in the low-frequency regime as it forces the induced currents to remain close to the beam.

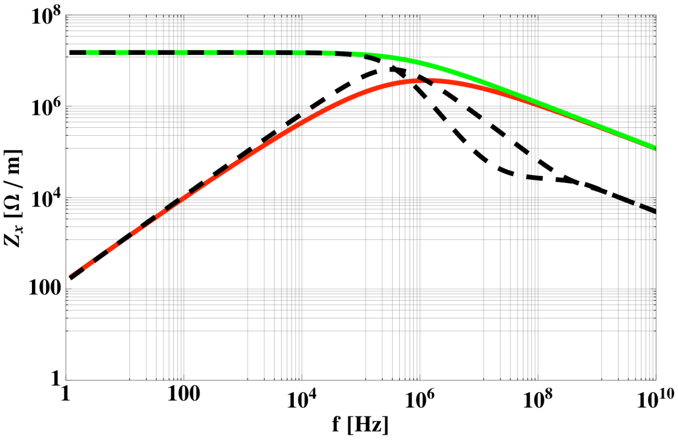

Fig. 1. Transverse (driving) impedance of a cylindrical LHC collimator (even if in reality the LHC collimators are composed of two parallel plates), with b = 2 mm, ρ = 10 μΩm, L = 1, μ_r = 1 and β = 1. The real part is in red while the imaginary part is in green (note that in the classical thick-wall regime, the real and imaginary parts are equal). The dashed curves correspond to the case with a copper coating of 5 μm.

B. Two-Dimensional Models For The Computation Of The Resistive-Wall Impedance

Two-dimensional analytical computations of beam coupling impedances have been developed for more than forty years, as discussed before and simple formulas exist and can be applied in many cases. However, some machine elements, e.g. the vacuum pipe, can typically exhibit a thin coating that cannot be assumed to be infinitely thick, in particular when considering very long-ranged wake fields that one needs to compute in order to perform beam dynamics simulations in the multi-bunch regime. To go beyond these limitations a general multi-layer theory is considered here. For an axisymmetric two dimensional geometry, analytical calculations have been existing since a long time: one can mention the general formalism of B. Zotter [18,28-31], the one of A. Burov and V. Lebedev [32] which is simpler but slightly less general, and more recently some matrix formalisms using potentials [33-36]. For other simple but non-axisymmetric two-dimensional geometries (elliptic, rectangular, or flat and infinitely large), the usual approach is to deduce the impedance from the axisymmetric case multiplied by some constant form factors [37] depending on the geometry, often called Yokoya [7] or Laslett [6] factors. However, recently it has been shown that this approach to compute the beam coupling impedances of a flat chamber fails in the case of non metallic materials such as ferrite [38]. Indeed, the hypotheses on which the form factors theories rely break down for general non conductive materials and/or over certain frequency range: in Ref. [6] one is concerned only about perfectly conductive materials in the static case, whereas in Refs. [7,37] one assumes that the beam is ultrarelativistic and that the chamber material is conductive with a skin depth much smaller than both the chamber thickness and its half gap. Since the skin depth is a monotonically decreasing function of frequency, the latter assumption implies a lower bound in frequency. Other more general approaches exist, in single-layer [39,42], two-layer [43] or even multi-layer [44] cases. In both the axisymmetric and flat cases, we will here go beyond the low frequency assumption made in Refs. [32,44], namely that in the frequency domain of interest the wave number is much smaller than the inverse of the minimum transverse dimension of the pipe or flat chamber surrounding the beam. A more general theory is typically needed in future linear colliders where one might well need to go beyond this low frequency approximation since the bunches will be very short [45,46], while the knowledge of the low frequency behaviour will also be needed, in particular if e.g. several bunches are circulating in a damping ring. We present here complete general multilayer formalisms in frequency domain, in longitudinal and transverse, in both the axisymmetric and flat two-dimensional infinitely long cases. Both theories presented are valid with any number of layers, any beam velocity and any frequency, and give all nonlinear terms in the resulting impedances. Each layer can be made of any resistive, dielectric or magnetic material, assuming only its linearity, isotropy, homogeneity and the validity of Ohm's law when it is conductive (thus neglecting the magnetoresistance and the anomalous skin effect). The formalism described here is largely based on B. Zotter's formalism and the complete description of the theory we outline here can be found in Ref. [47].

The main steps of the computation (using field matching) are the following: (i) we write the wave equations for the longitudinal components of the electromagnetic fields and solve them in each homogeneous layer (the solutions of the wave equations in each layer are linear combinations of modified Bessel functions); (ii) the transverse components are then found by application of Maxwell equations; (iii) expressing the boundary conditions, it can be shown that the integration constants of one layer are related to those from the adjacent layer through a simple matrix multiplication matrix (which is 4 × 4); (iv) the final solution of the problem is then found by computing the matrix relating the constants in the first layer to those in the last one, which is obtained from a multiplication of all the matrices found by matching the fields at each layer boundary. Expressing finally the boundary conditions for r and after a simple inversion of the 4 × 4 matrix one gets the complete set of integration constants and solves entirely the electromagnetic problem. The expressions found give the general nonlinear and multimode wall impedance, i.e. that includes all azimuthal modes m. We note here that, contrary to usual ultrarelativistic results (see e.g. Ref. [10]), we obtained non zero quadrupolar impedances even in the case of an axisymmetric chamber. This comes from the $m = 0$ mode, so from the fact that we considered together all azimuthal modes instead of treating separately the $m = 0$ and $m = 1$ modes and identifying the transverse impedances to those exclusively coming from the $m = 1$ mode, as is usually done.

In the case of a flat chamber, as it is typically the case for the LHC collimators, the approach is very similar to the one adopted for the cylindrical chamber. The solutions of the wave equations in each layer are found here as linear combinations of complex exponentials. Instead of summing all azimuthal modes as in the cylindrical case, we have here instead to integrate back over the wave number to get the final solution of the problem in frequency domain. The integrals cannot be performed analytically but can be rearranged such that we get a form similar to what we found in the axisymmetric case. Note that the horizontal impedance has no constant term due to the left-right symmetry but the vertical impedance has a non-zero constant term due to the absence of top-bottom symmetry. Concerning the dipolar and quadrupolar terms, we note that the horizontal quadrupolar impedance is equal to minus the horizontal dipolar impedance, which is a direct consequence of the continuous translation invariance along the horizontal axis. However, contrary to ultrarelativistic results, the horizontal quadrupolar impedance is not equal to minus the vertical quadrupolar impedance, due to the quadrupolar term already found for the impedance in an axisymmetric structure. Few examples of application are shown in Figs. 2-4. In Fig. 2 we show the dipolar wall impedance in the case of a graphite round collimator, with one layer or three layers. The difference between the two is mainly due to the copper coating in the three layers case, and this difference decreases at low frequencies because the fields penetrate deep inside the collimator wall. In Fig. 3 we have plotted the vertical dipolar impedance of a copper coated graphite flat collimator, comparing our results to Tsutsui's model [48] on a rectangular geometry, putting the plates perpendicular to the jaws 25 cm apart in order to get closer to the case of an infinitely large chamber. The agreement between the two approaches is very good. Finally, the form factors (i.e. the ratios between the linear terms in the flat chamber transverse impedance components and the dipolar impedance of an axisymmetric chamber with radius equal to the half gap of the flat chamber) are plotted in Fig. 4 for the case of the LHC injection protection collimator (TDI) made of titanium-coated hBN blocks. These form factors are a frequency and material dependent generalization of the constant Yokoya factors [7]. With respect to the Yokoya factors, some differences in the transverse form factors appear around MHz frequencies and for frequencies above ~ 1 GHz (in particular for the resonant peaks between ~ 1 GHz and ~ 100 GHz), while in longitudinal the form factor calculated from this theory is on most of the frequency range significantly different from the Yokoya factor. This can be explained by the fact that the hypotheses on which the Yokoya factors theory relies do not apply here, since one of the layers is highly resistive.

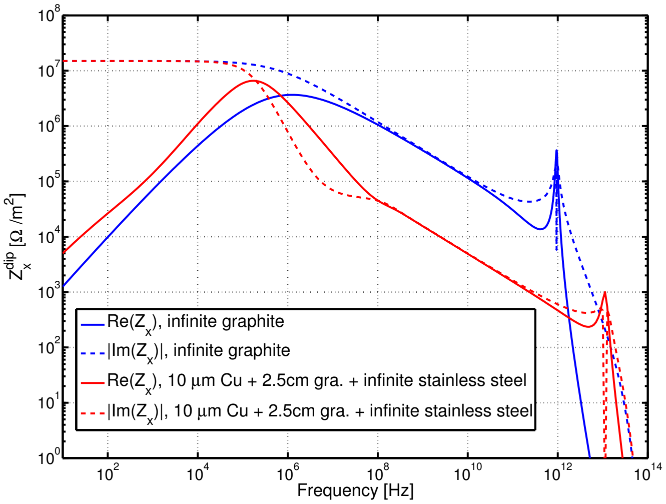

Fig. 2. Dipolar impedance (per unit length) of a round collimator: $b = 2$ mm, $\gamma = 479.6$, σ_{DC} (Cu) = 5.9 10^7 S/m, τ_{AC} (Cu) = 27 fs (relaxation time for the Drude model), σ_{DC} (graphite) = 10^5 S/m, τ_{AC} (graphite) = 0.8 ps, σ_{DC} (steel) = 10^6 S/m, τ_{AC} (steel) = 0.

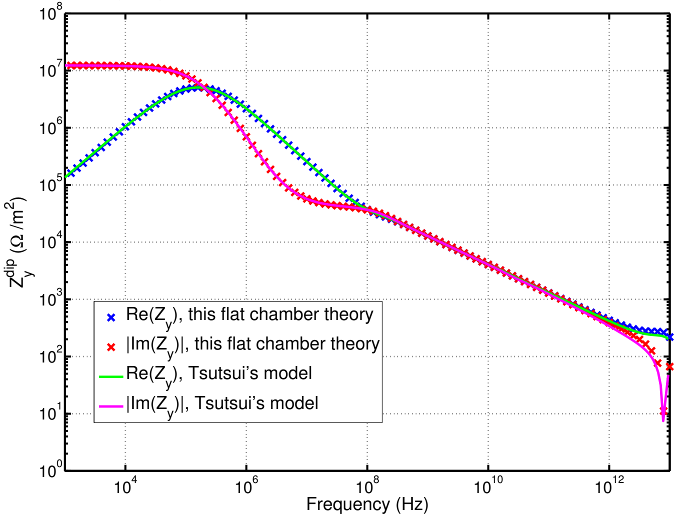

Fig. 3. Vertical dipolar impedance (per unit length) for a three-layer copper coated graphite flat collimator (parameters in Fig. 2). In Tsutsui's model, the third layer is replaced by a perfect conductor, and the plates perpendicular to the large flat jaws are 25 cm apart.

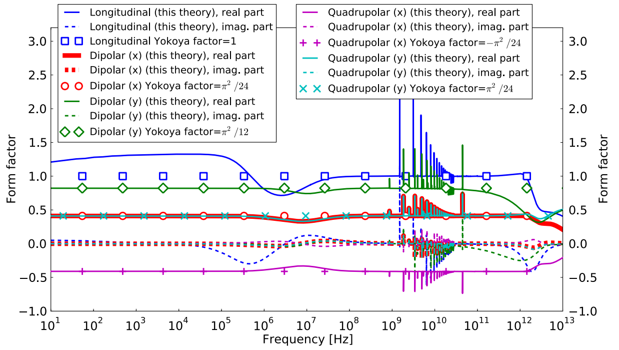

Fig. 4. Form factors between the flat and cylindrical geometries, for the impedances of the titanium-coated hBN block of the LHC injection protection collimator (TDI). Length of a hBN collimator of length: 2.8 m; $\gamma = 479.6$; half gap: 4 mm; each jaw is made of three layers: a 3 µm thick titanium coating (with resistivity 0.43 µΩm), a 54 mm thick hBN ceramic (dielectric constant 4, resistivity 4 10^{12} Ωm) and an infinitely thick stainless steel layer (resistivity 0.72 µΩm).

C. *Impedance Effect Due To The Finite Length*

For the LHC collimators, whose length (~ 1 m) is much longer than the half gap (few mm), the previous 2D computation was expected to be a good approximation (i.e. what is important is to compute the impedance per unit length and then we multiply by the length of the structure) but this had to be checked. Furthermore, there were some ideas to build shorter collimators and there are some equipment which are segmented such as kickers.

The problem of evaluating the impedance of finite length devices has been approached in the past mainly by means of the field matching technique making use of careful approximations where the cavity-like structure was approximated as a thin insert [49,53]. This technique is based on imposing the continuity of electric and magnetic fields at the boundaries between the finite length device and the access beam pipes. While the magnetic continuity can be easily imposed, this is not the case for the electric continuity. A different approach to the problem based on the mode matching technique is presented here. In order to take into account the finite length of the structure, we decompose the fields in the device into a set of orthonormal modes. We obtain a complete set of equations using the magnetic field matching and the nonuniform convergence of the electric field on the beam pipe access boundaries. As a case of study, we describe the method application to an azimuthally uniform structure of finite length: a cylindrical cavity loaded with a toroidal insert of lossy dielectric, connected to a cylindrical beam pipe. Then we present benchmarks done with the IW2D code [47], CST Particle Studio [12] and other existing analytical formulas and codes, pointing out the effect of finite length on the impedance of thin inserts, collimators and small beam pipe protrusions. Interesting observations concerning the impedance at frequencies close to the beam pipe cut-off frequency can also be explained.

Structures like the toroidal insert of lossy dielectric discussed above are common in particle accelerators. Opportunely varying the longitudinal and radial dimensions, or the insert material parameters, the structure could represent a beam pipe, a small discontinuity, a flange connecting two beam pipes, a loaded cavity, or even a collimator.

We introduce here the three relevant frequency parameters f_c, f_{co} and f_{skin}. The parameter f_c is the frequency limit at which a metal with a given conductivity σ can be treated as a good conductor, i.e when $\sigma > \omega\, \varepsilon_0$, and is defined as

$$f_c = \frac{\sigma}{2\,\pi\,\varepsilon_0}. \tag{18}$$

We define f_{co} as the beam pipe cut-off frequency (which depends on the impedance under study): for the longitudinal impedance, for example, only TM modes are excited and we define

$$f_{co}^{\mathrm{TM}} = \alpha_{0,1}\,\frac{c}{b}, \tag{19}$$

where $\alpha_{0,1} \approx 2.4048$ is the eigenvalue corresponding to the TM_{01} propagating mode. The parameter f_{skin} is the frequency at which the skin depth equals the insert thickness t. It is important to notice that we can define a f_{skin} only in the hypothesis of good conductor, i.e. $\sigma > \omega\,\varepsilon_0$ or $f < f_c$. Several cases have been benchmarked. Two cases are discussed below.

1) *Impedance Of A Thin Insert*

The beam pipe of accelerator machines is frequently interrupted and connected by means of thin inserts. Due to the large number of beam pipe transitions in circular accelerator machines, the contribution to the total machine impedance of these discontinuities can be important. The structure discussed before can model a thin insert when $L << t$. The mode matching model to the calculation of the longitudinal impedance of thin inserts as well as comparisons with the SCT theory [52] are shown in Fig. 5. In the SCT model the PEC boundary layer around the insert is not present and the field can propagate in free space. Moreover, following the approximation of short insert length in the SCT theory, the longitudinal field variation along z has been neglected (these approximations have been recently removed within an extension of the SCT model [53]). Therefore, the frequency regime in which the two models are expected to agree is above f_{skin} (which is the case as can be seen from Fig. 5). Below f_{skin}, the two models start to diverge: with mode matching the transverse field approaches the cavity's boundary and is reflected; in SCT it is radiated to the external vacuum region. From f_{skin}, the two models start to converge to the same impedance value. However, one may notice (looking at the difference between the two approaches) that the mode matching impedance slightly oscillates around the SCT's one before converging to the same curve. The discrepancy between the two models can be understood considering that around f_{skin} the skin depth is comparable with the insert thickness. This implies that the backward wave slightly interferes with the outgoing wave producing a modest standing wave pattern in the insert, therefore affecting the impedance. With increasing frequency, the backward wave amplitude becomes smaller and smaller and this pattern vanishes. The discrepancy at high frequency has to be compared with the impedance absolute value, which becomes larger and larger.

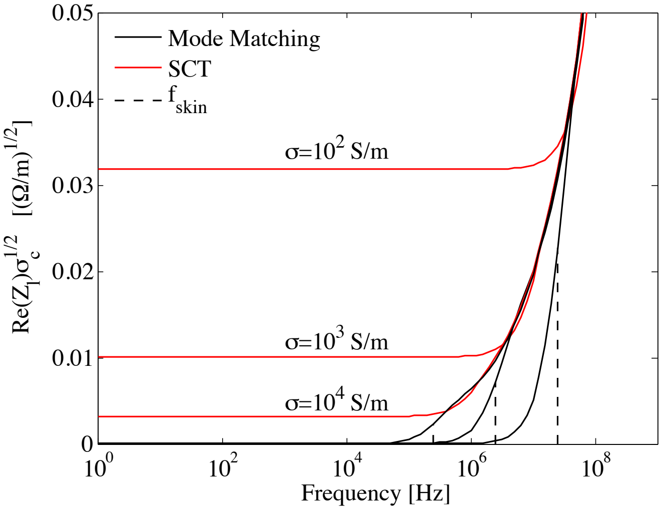

Fig. 5. Comparison between mode matching and SCT model for the longitudinal impedance of short inserts. Mode matching parameters: $b = 5$ cm, $t = 1$ cm, $L = 0.1$ cm and $\beta = 1$.

2) *Impedance Of A Collimator*

Figure 6 shows the ratio between the transverse dipolar impedance calculated with the mode matching and the IW2D code for varying length. When $L < b$, the transverse low frequency impedance in the finite length assumption becomes higher up to a factor 2 with respect to the infinite length one, as shown for the imaginary part. This effect, due to the contribution of the fields at the edge of the structure, can be considered not of particular concern being apparent only for short inserts at very low frequencies (10 - 100 Hz). No evidence of this effect has been instead observed in the longitudinal impedance, probably due to the small effect of the edges on the longitudinal electric field on axis. Within the hypothesis of our model we can therefore conclude that there is no significant impedance reduction by segmenting the LHC collimators.

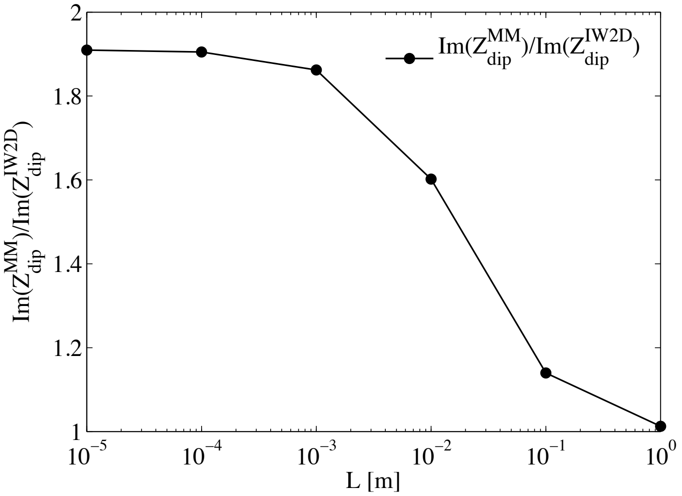

Fig. 6. Ratio between the finite length impedance (mode matching) and the infinite length one (IW2D). Mode matching parameters: $b = 5$ cm, $t = 25$ cm, $\sigma_c = 10^6$ S/m, $\beta = 1$.

D. *Impedance Simulations*

Analytical wake field computations are possible only for very simple geometries, thus in practice one has to rely on numerical techniques. Although the term beam coupling impedance was introduced first in the frequency domain by Vaccaro [54,8] in 1966, first numerical wake field computations were performed in the time domain by Balakin et al. [55] in 1978, and Weiland [56] in 1980. For highly relativistic bunches, due to causality, wake fields can catch up with trailing particles only after traveling a certain distance, the so-called catch-up distance [57]. This motivates computing wakes in linacs by using a mesh that moves together with the bunch. The moving mesh technique was introduced by Bane and Weiland in 1983 [58]. Nowadays many methods are available for beam coupling impedance computation: Time Domain (TD) method and Frequency Domain (FD) method, which splits in two main groups, the eigenmode methods and methods based on beam excitation in FD. The three methods are discussed below and an example of simulation with CST [12] is shown in Fig. 7.

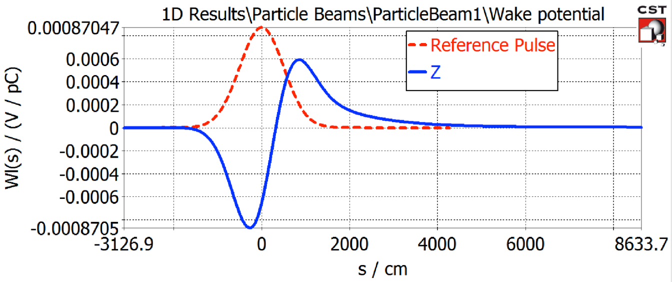

Fig. 7. Example wake function computed with CST Particle Studio® [12].

1) *Time Domain (TD)*

Most common TD methods are based on Finite Differences Time Domain (FDTD, Yee 1966 [59]) and Finite Integration Technique (FIT, Weiland 1977 [60]) where the leapfrog algorithm is applied for time stepping. More specialized techniques are the boundary element method (TD-BEM) [61-63], the finite volume method (FVTD) [64], Discontinuous Galerkin Finite Element (DG-FEM), and implicit methods. Due to the minimal duration-bandwidth-product, the excitation is usually done by a Gaussian bunch, which rigidly moves through the structure. The duration and bandwidth of the excitation are

$$T = \frac{\sigma_s}{\upsilon\sqrt{2}}, \qquad B = \frac{\upsilon}{\sigma_s\sqrt{2}}, \tag{20}$$

resulting in minimal $TB = ½$. The choice of the bunch length σ_s in a simulation does not necessarily depend on the real bunch length, but rather on the frequency of interest. The maximum frequency at which a reasonable excitation amplitude is present, is roughly 2 σ_f, i.e. the spectrum is mainly located at $\sigma_f = \upsilon / (2\,\pi\,\sigma_s)$, the so-called frequency associated with the bunch length. Shorter bunches increase the maximum frequency, but they decrease the frequency resolution, which is a particular problem at low frequency. The frequency resolution depends on the total number of points employed for the Discrete Fourier Transform (DFT),

$$\Delta f = \frac{1}{N_t\,\Delta t}. \tag{21}$$

The total integrated wake length is $L_{wake} = \upsilon\,N_t\,\Delta t$. Bunch length and wake length are the two important parameters for TD impedance computation. The choice of finite length puts a window-function on the real wake potential. If it is chosen too small, i.e. when the window closes before the wake has decayed, the impedance will show the Gibbs phenomenon. This can be smoothed by choosing other than rectangular window functions, but one should note that this does not improve the frequency resolution.

The semi-discrete Maxwell Grid Equations (MGE) can be written in FIT notation. Discretizing the time by central difference quotients on a staggered grid leads to the so-called leapfrog scheme. Applying this scheme to a plane wave in a single Cartesian (staircase) cell leads to the grid dispersion relation (see e.g. [65]) reproducing the continuous dispersion relation when all the space and time steps tend to zero. The criterion for the time step Δt is also referred to as the Courant-Friedrichs-Lewy (CFL) criterion [66].

Finite mesh size will always result in different propagation velocities dependent on the propagation direction, which can cause unphysical effects such as numerical Cherenkov radiation [67] and positive longitudinal wake functions at the head of a bunch. In order to reduce this dispersion several techniques are available (see [68]). There are techniques that have no dispersion in beam propagation direction at all, e.g. Gjonaj *et al.* implemented longitudinal-transverse splittings [69] and Zagorodnov implemented a TE-TM wave splitting scheme [67]. Furthermore, one should mention that conformal techniques have improved the modeling accuracy significantly and feature second order convergence, see e.g. [70]. Overviews of codes are available in [71] or [72].

The Panofsky-Wenzel theorem [73], as already discussed above, is fundamental in impedance and wake field computation. When boundary conditions are available, the longitudinal wake potential can be solved from the Laplace equation, and the transverse can be subsequently obtained from the longitudinal one [74]. For rotationally symmetric structures, it is sufficient to integrate the wake at an arbitrary radial coordinate, as the radial dependence is known a priori. This radial coordinate can be chosen right at the perfectly conducting beam pipe surface, reducing the integration to the cavity gap length [75]. In rotational symmetric structures it is also possible to choose a curved contour, the Napoly integral [76,77]. A combined contour-integration and Laplace-equation method is presented by Henke and Bruns [78]. An approach to avoid lengthy wake integration for evanescent waveguide modes in the beam pipe after a cavity is presented by Dong *et al.* [79]. Finally generalized methods for arbitrary structures are presented by Zagorodnov [80].

Space charge fields have to be taken into account for the calculation of wake fields and impedances in the non-ultrarelativistic case. This is particularly a challenge at the boundary where the beam enters and exits the computational domain. Pretending the beam enters and exits in an infinitely long, smooth, and perfectly conducting pipe, the space charge fields (source fields) in this pipe have to be calculated, and can subsequently be imprinted on the boundary. A consistent way to compute and imprint the source fields by means of numerical Lorentz-transformation is presented by Balk *et al.* [81,82].

2) *Eigenmode*

The longitudinal impedance of a resonant structure can be written in terms of eigenmodes (for the transverse impedance the same approach can be performed with dipole modes). The eigenmodes are solutions of MGE [83]. If the structure is lossless, the above matrix can be rewritten as symmetric and positive semi-definite, i.e. the eigenvalues are real and non-negative. In such systems only the eigenfrequency and the eigenmode can be determined, the R_{sh} and Q have to be determined from the wall losses by a perturbation approach. When strong losses are present, the eigenvalues become complex and R_{sh} and Q can be extracted from the imaginary part. However, the MGE become nonlinear as the conductivity enters the permittivity with a factor ω. eigenvalue computations are usually applied for beam coupling impedance computations only when Q is very high and high accuracy is required. Ackermann *et al.* [84] developed a solver for such structures, which is also capable of computing modes above the beam pipe cut-off, i.e. modes with energy leaking out of the cavity. Apart from high Q systems, recent developments also include eigenvalue computations for dispersively lossy tensorial materials utilized in tunable ferrite cavities [85].

3) *Frequency Domain (FD)*

At low frequencies, the CFL criterion already poses a strong requirement on the time step. Due to the uncertainty principle, lower frequencies require computing longer wakes. As the time step is fixed by structure properties via the CFL criterion, this leads to the necessity to compute very many time steps, i.e. massive oversampling. In order to circumvent this, FD-methods can be used to compute the beam coupling impedance directly via electromagnetic fields in FD, interpreting the longitudinal and transverse impedances as functionals of the electric field solution of Maxwell's equations in FD with the monopolar and dipolar excitation current densities given by a charged disc which is allowed to perform linearized dipole oscillations. Note that also the spectral density of the charge has to be taken into account, especially in the choice of appropriate beam entry and exit boundary conditions. Infinite beam pipe boundary conditions were implemented by van Rienen [86], Balk [81] and Doliwa [87], Floquet (quasi-periodic) boundary conditions by Niedermayer [88]. Approximations to neglect the charge completely result in quasi-stationary models and are discussed in [89,90]. Solutions can be obtained by the FIT, where Doliwa [87,91] implemented a special low frequency stabilization technique based on Neumann series expansion of the divergence corrected (Helmholtz decomposition) system matrix. The coefficients of this expansion are obtained by fix-point iteration through the four Maxwell equations, therefore the scheme has been named "Maxwell iteration". When the length of the computational domain with Floquet boundary conditions is reduced to zero (practically one cell), one obtains a 2D scheme. This system has been treated with FIT [88], with FEM [92], and also with the Boundary Element Method (BEM) [93]. The FEM approach [92] applies nodal elements on the longitudinal and edge elements on the transverse field components. Since the edge elements of lowest order are not suited to represent the divergence of a vector field, a Helmholtz decomposition needs to be performed and the static fields are obtained from the gradient of a potential subject to the complex Poisson equation. Such a FEM scheme is very flexible due to the unstructured mesh, i.e. it can model different dispersively lossy materials, surface impedance boundary conditions, and arbitrary beam shape and velocity, which is particularly useful for low energy, space charge dominated synchrotrons.

In summary, TD simulations using FIT or FDTD are suitable at medium and high frequency, and particularly in perfectly conducting structures. Explicit time stepping methods, such as leapfrog, are extremely efficient, as they require only a matrix-vector multiplication at each time step. Grid dispersion is a severe issue in those methods but has recently been improved by novel schemes. The infinite wake integration can be simplified by modifying the contour using the Panofsky-Wenzel theorem. TD methods are disadvantageous for low frequencies and low velocity of the beam. Also dispersively lossy material is difficult to treat in TD. In those rather exotic cases, FD methods prevail. When high quality factor structures are under investigation and high accuracy is required, eigenmode computations should be used.

E. *Building The Impedance Model Of A Real Machine*

Assessing the intensity limitations of a synchrotron is an essential step to predict its performance. While some impedance related limitations can be considered to be localized to a piece of hardware (e.g. equipment heating due to beam coupling impedance or electron cloud), the impedance contributions to beam instabilities cannot be considered individually and have to be aggregated for the whole machine. For this reason, impedance models have been built for many existing machines, upgrades and projects. Impedance models are usually started at the very early stage of machine design to assess if impedance related instabilities could be a limitation and should drive fundamental parameters of the accelerator. Therefore, impedance models in various forms and levels of complexity were developed over the years depending on the needs and knowledge at the time of implementation: for example for the CERN ISR [94], PS [95-97], PSB [98], SPS [99-102], LEP [103], LEP2 [104] LHC [104,105], RHIC [106] at Brookhaven National Lab, TeVatron [107] at Fermi National Lab, HERA [108] at DESY, KEKB [109], as well as many light sources: NSLS-II [110], PETRA [111] SOLEIL [112], ALBA [113], to name only a few.

In fact the complexity of an impedance model can range from a single number to an elaborated tool, which is able to recompute complex impedance contributions as a function of frequency and their related thresholds with slight changes of machine configuration (e.g. energy and gaps of moving devices). Ideally, one would aim for computing the longitudinal, as well as transverse driving and detuning contributions for obtaining all resistive wall, broadband and narrow band contributions over a frequency range that would span from the first potentially unstable frequency to the maximum frequency that can be excited by the various bunch modes. In practice, depending on the further use of the model – e.g. interpolation in frequency or time domain for theoretical formula or macroparticle simulations; single bunch or multi bunch studies – the frequency range and/or wake length can be drastically reduced.

1) Procedures To Build An Impedance Model

The procedure to build longitudinal and transverse impedance models are represented in Fig. 8.

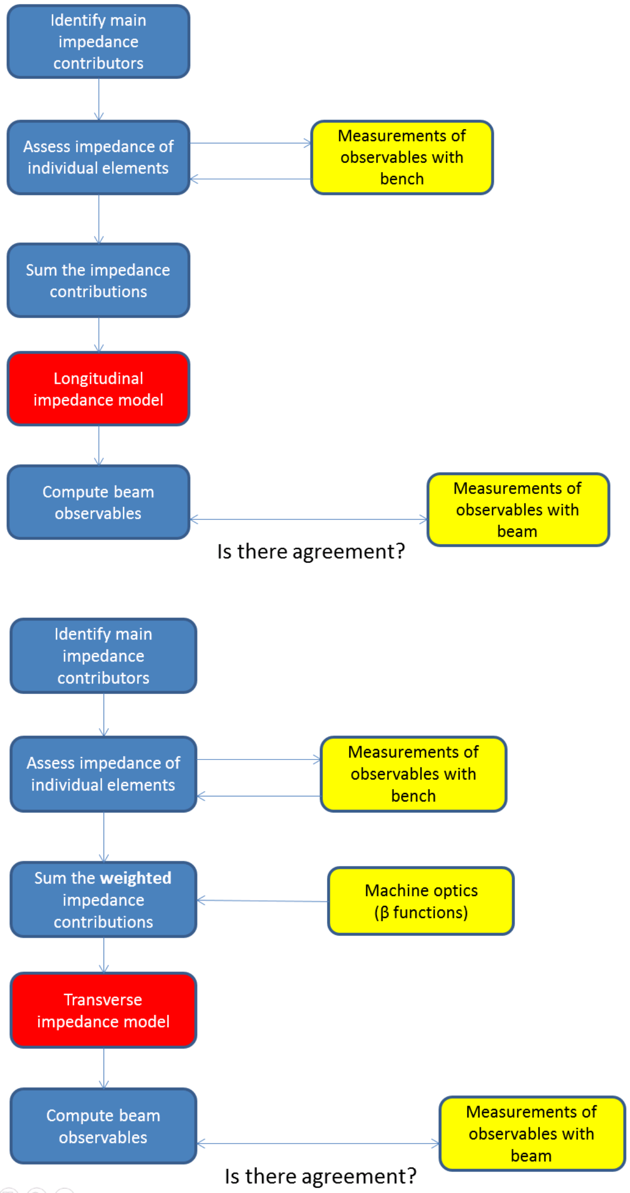

Fig. 8. A procedure to build a longitudinal (top) and transverse (bottom) impedance model.

The first step is to identify the main impedance contributors for the accelerator. These generally include the geometric and resistive contributions from the vacuum chambers, kickers, collimators, instrumentation, RF cavities, pumping ports and detectors. Once identified, these impedance contributions can be assessed using various tools. Analytical computations are the method of choice for simple geometries (see before). Geometric contributions of various basic accelerator geometries, bellows, tapers, step transitions can also be found [114], as well as for instance elliptical tapered transitions [115]. For more complicated geometries, the recent progress of simulation codes allows to compute the impedance of increasingly detailed geometries. The main electromagnetic codes currently used are ABCI [116], ACE3P [117], Ansys HFSS [14], CST Studio (MAFIA) [12], ECHO2D [118], GdfidL [119]. Bench measurements can also be performed on prototypes or final devices ready for installation using wires (1-wire and 2-wire-measurement techniques), probes and coils [120]. These measurements are efficient to benchmark the models used for computations, but cannot always be used directly for the impedance model due to the perturbation of the measuring device. The impedance contributions can then be summed to obtain a global impedance model for the whole machine. As seen in Fig. 8, it is important to note that the transverse impedance contributions have to be weighted by the ratio of the respective β-functions at the location of the element to the chosen reference for the β-function later used for beam dynamics computations when the impedance contributions are lumped at one single location. Typically the average β-function - either computed from the smooth approximation or from the actual average of the β-function around the ring - is chosen for this purpose. Beam observables may then be computed either by using analytical Vlasov solvers or macroparticle simulations (see later). These simulated observables should then be compared to beam observables measured in the machine (synchrotron and betatron tune shifts with intensity, longitudinal and transverse instability thresholds as a function of e.g. bunch length and longitudinal emittance for the longitudinal plane, chromaticity, amplitude detuning and damper gain for the transverse plane). This is clearly an iterative process where the impedance model should be refined to try and make the predicted observables agree with the measured observables. Unfortunately, this procedure is rendered difficult by several hurdles that come up at every level.

2) Sample Of Current Challenges To Build An Accurate Impedance Model

a) Is the model representative of reality?

One of the major difficulties encountered when building an impedance model is the lack of knowledge of what the machine is actually made of. When dealing with accelerators that were built decades ago, drawings may be hard to find and outdated. In addition, electromagnetic properties of some special materials are usually neither specified nor measured by the manufacturer and could be impossible to obtain if the manufacturer stopped its activity. It is also important to note that even if an up-to-date drawing of the geometry is available, non-conformities, damage and ageing may have altered the initial design and can represent a large source of errors. If some individual large contributors to the machine impedance can be quickly identified by their features (large resistivity, large magnetic losses, cavity-like structure, small aperture, steps), the integrated effect of many small contributions is more difficult to evaluate with accuracy: the error on the estimate is multiplied by the number of elements.

b) *Limitations of the simulation codes*

Limitations in the details that can be modelled often – if not always – require drastic simplifications for analytical estimates or 3D simulations, and the relevance of this cascade of simplifications cannot always be checked. This is in particular why a benchmark of computations with bench measurements is a crucial step for validating the assessment the impedance of an element. The limitation in the maximum number of mesh cells by the available memory and/or computing time also limits the maximum simulated frequency. This represents a severe limitation for 3D wakefield codes as the minimum exciting bunch length directly drives the needed smallest mesh cell size. Wake potentials with small exciting bunch lengths are needed for beam dynamics codes that slice the bunch into dozens of small slices. Ideally, a convergence should be found for the whole chain down to the beam dynamics, but it does not always work. However, a recipe was recently proposed to find the optimum bunch length for electromagnetic simulations [121]. It is also important to note the following major limitations of impedance codes:

- Many codes or features do not work efficiently when $\beta < 1$;
- Many analytical formulae are only valid in a limited range of frequencies and for simple geometries;
- The connection to complex external circuits with long cables is not easy to account for with 3D models;
- The difficulty to separate the dipolar and quadrupolar impedances with the eigenmode solver in non-symmetric structures;
- Despite recent significant effort in the treatment of dispersive materials in both wakefield and eigenmode solvers, modelling these materials is still suffering from large errors;
- Accounting for coatings and anisotropic materials in 3D simulation codes is not straightforward and leads to large errors;
- The current 3D simulation tools are not efficient for very short bunch length that excites frequencies well above the cut-off of the connecting pipes. This is due to the fact that the absorbing boundaries cannot be made perfectly absorbing. Besides, the commercial eigenmode solvers cannot work reliably with this type of boundaries and are therefore not recommended for use beyond the cut-off of the respective modes. Solutions are in development to cope with this problem [122].

c) *Challenges in aggregating the impedance contributions*

For a given machine, several contributions may come from various analytical or simulation codes (even for one single element which requires eigenmode simulations to obtain the resonant modes and wake field simulations to obtain the contribution over the full frequency range with a lower accuracy in the region of these modes). Results can therefore be in wake functions, wake potentials, impedances or eigenmode tables, which makes it difficult to get a global impedance for all purposes that would also be compact. The proposed strategy in this case is to keep the initial data for all contributions in a database, and to adapt their post-processing to the final goal:

- If the beam dynamics tool -, which will use the impedance - requires a single bunch wake as input, then a small bunch with a short wake length can be chosen (as in [101] for instance);
- If the beam dynamics tool requires a broadband impedance as input, then a long bunch with a long wake length can be used;
- If the beam dynamics tool requires both low and high frequency content, then a non-equidistant FFT to transform impedance into wake can help [105] to reduce the number of sampling points, and both short bunch and long wake length are needed, which may be beyond the limits of the simulation capabilities of the code.

Interpolation is required to sum contributions. If many resonances are present in the model, the number of points in the wake or in the impedance can be very large (of the order of 10^5 sampling frequencies for the LHC impedance model). Besides, impedance contributions have been added as broadband resonator contributions assuming that the global frequency would be the cut-off frequency of the main vacuum chamber (for instance in [123]). When this may be argued for the case of a machine with many sharp steps and bellows for which the single impedance contributions could amount to a broadband behaviour, it is more difficult to accept this simplification for machines which have been heavily optimised with respect to impedance, and therefore all contributions should be accounted for individually with their own cut-off. Finally the knowledge of the β-function at all devices is needed to obtain an accurate transverse impedance model. If the β-functions are well known for a running machine, the planned locations and/or beta functions of a device for a new project may not be clearly defined until a very late stage of design.

3) *Beam-Induced RF Heating*

Beam-induced RF heating has been observed in many places, as for instance recently in several CERN LHC components during the 2011 and 2012 runs when the bunch/beam intensity was increased and/or the bunch length reduced [124,125]. This caused beam dumps and delays for beam operation (and thus less integrated luminosity) as well as considerable damages for some equipment. This is why the rms bunch length was increased to ~ 9 cm in 2011 and ~ 10 cm in 2012, whereas the nominal value is 7.5 cm. The RF heating of some equipment is therefore worrisome for the future operation and it is closely followed up [126].

Therefore, in practice the elements of the vacuum chamber should be designed to minimise the self-generated (secondary) electromagnetic fields. For example, chambers with different cross-sections should be connected with tapered transitions; non necessary cavities should be avoided; bellows should preferably be separated from the beam by shielding; plates should be grounded or terminated to avoid reflections; poorly conductive materials should be coated with a thin layer of very good conductor (such as copper) when possible, etc. However, the issue with the diagnostics structures is that they are designed to couple to the beam. The beam-induced RF heating comes from the real part of the longitudinal impedance and the bunch length (and sometimes longitudinal profile) is the main parameter (once the bunch intensity and number of bunches have been fixed): usually, the longer the bunch, the better.

Consider the case of M equi-spaced equi-populated bunches, which should be a good approximation when the LHC machine is full. In this case, the general formula for the beam power loss (due to the interaction with the longitudinal impedance) can be written [125]

$$P_{loss} = M\, I_b^2\, Z_{loss}\,, \tag{22}$$

with

$$Z_{loss} = 2\,M \sum_{p=0}^{\infty} \mathrm{Re}\left[Z_l\left(p\, M\, \omega_0 \right) \right] \times \mathrm{PowerSpectrum}\left[p\, M\, \omega_0 \right], \tag{23}$$

where $I_b = N_b\, e\, f_0$ is the bunch current and PowerSpectrum stands for the beam power spectrum. Different longitudinal profiles are considered in Fig. 9 (top) and their corresponding beam spectra are shown in Fig. 9 (bottom). A comparison between the different longitudinal beam power spectra of several machines is shown in Fig. 10 (assuming a longitudinal profile with n = 3, see Fig. 9), revealing the frequency ranges of interest for the different machines. Whereas the LHC is interested in the frequency range of few GHz, the other machines discussed (synchrotron light sources) are interested in few tens of GHz.

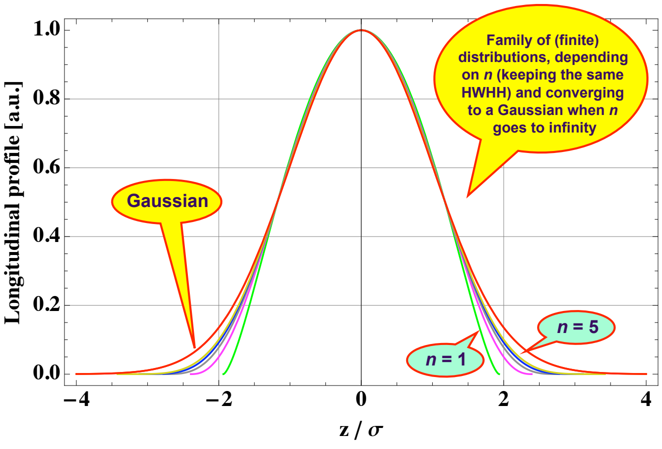

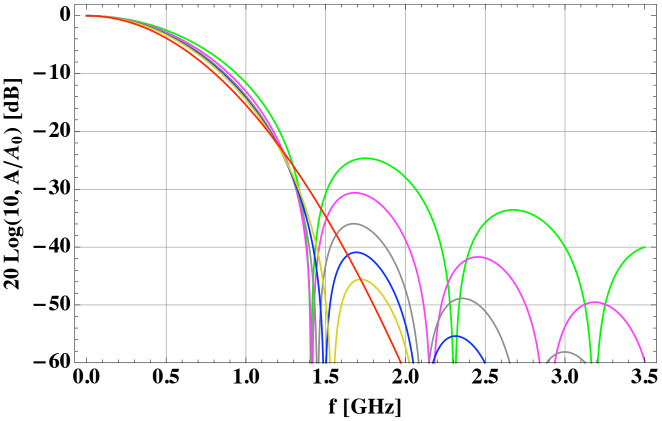

Fig. 9. (Top) Family of (finite) distributions, keeping the same half width at half height, depending on a parameter n, and converging to a Gaussian distribution when n goes to infinity. (Bottom) Corresponding beam power spectra.

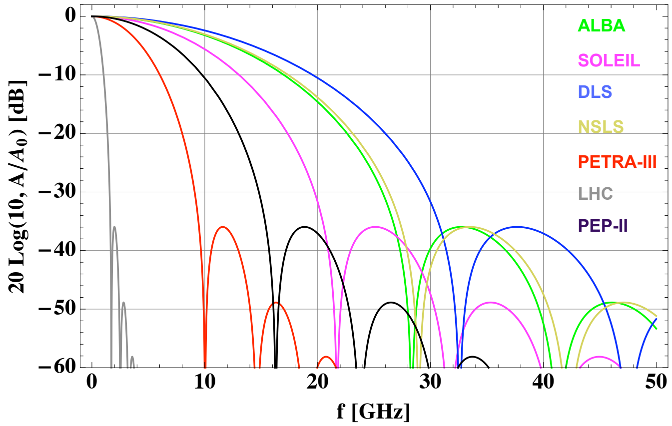

Fig. 10. Comparison between the different longitudinal beam power spectra of several machines, revealing the different frequency ranges of interest.

The power loss is always proportional to the square of the number of particles per bunch but depending on the shape of the impedance, it can be linear with the number of bunches (when the bunches are independent, i.e. for a sufficiently short-range wake field – or broad-band impedance – which does not couple the consecutive bunches) or proportional to the square of the number of bunches (when the bunches are not independent, i.e. for a sufficiently long-range wake field – or narrow-band impedance – which couples the consecutive bunches). These two extreme cases are discussed below.

In the case of a broad-band impedance, consider for instance the case of the resistive-wall impedance, and, as a numerical example, the particular case of the LHC beam screen (neglecting the holes, whose contribution has been estimated to be small in the past, and the longitudinal weld). Assuming a Gaussian longitudinal profile (other similar distributions would give more or less the same result in this case), the power loss (per unit of length) is given by

$$P_{loss/m}^{G,RW,1\text{layer}} = \frac{1}{C}\,\Gamma\left(\frac{3}{4}\right)\frac{M}{b}\left(\frac{N_b\, e}{2\,\pi}\right)^2 \sqrt{\frac{c\,\rho\, Z_0}{2}}\;\sigma_t^{-3/2} \tag{24}$$

where C = 26658.883 m is the average LHC radius, Γ the

Euler gamma function, b the beam screen half height (assumed to be 18.4 mm), ρ the resistivity (assumed to be 7.7 10^{-10} Ωm for copper at 20 K and 7 TeV) and σ_t the rms bunch length (expressed in unit of time). Assuming the nominal LHC beam parameters (M = 2808, N_b = 1.15 10^{11} p/b and σ_t = 0.25 ns), Eq. (24) yields ~ 100 mW/m.

Consider now the case of a narrow resonance, describing a trapped mode due to the geometry. It is described by 3 parameters: (i) the resonance frequency, assumed to be here f_r = 1 GHz; (ii) a shunt impedance, assumed to be here R_{sh} = 10 Ω; and (iii) a quality factor Q. In the case of a sharp resonance impedance (i.e. when $Q >> f_r \,/\, (\, 2 \, f_b \,)$ where f_b is the bunch frequency), the power loss is given by the simple formula (which is valid when $Q >> 1$ and $\Delta << 1$)

$$P_{loss} = R\, I^2 \times F \times G \tag{25}$$

with

$$F = 10^{\frac{P_{dB}(f_r)}{10}} \quad , \quad G = \frac{\Delta^2}{\Delta^2 + \sin^2\left(\frac{\pi f_r}{f_b}\right)} \quad , \quad \Delta = \frac{\pi f_r}{2\,Q\, f_b} , \tag{26}$$

where R = 2 R_{sh}, i.e. using the Linac convention (Linac Ohms), $I = M\, I_b$ is the total beam current and $P_{dB}\,(\,f_r\,)$ is the beam power spectrum in dB at the resonance frequency f_r read from a power spectrum (computed or measured). The factor F describes the frequency dependence of the power loss, which depends on (i) the longitudinal bunch length, (ii) the longitudinal profile and (iii) the resonance frequency. It converges to 1 at zero (low) frequency (where it is the worst case) and it is between 0 and 1 for any frequency. For a Gaussian bunch, the factor F is given by Exp[- (2 π f_r σ_t) ^{2}]. The factor G describes the off-resonance effect [127]: if the resonance falls exactly on an harmonic of the bunch frequency (i.e. on resonance), it is equal to 1, otherwise it is between 0 and 1. Assuming a total beam current of 1 A (the nominal LHC value is 0.58 A) and considering the theoretical longitudinal bunch spectrum of Fig. 11 (upper) for an rms bunch length of 9 cm (similar to the LHC case in 2011), a sharp resonance R_{sh} = 5 kΩ (usual typical values are between few hundreds and few tens of thousands Ohms) at 1.4 GHz (i.e. on resonance) would therefore generate a power loss of 1 W. However, this result is very sensitive to the bunch length. It can be seen for instance from Fig. 11 (lower), that dividing the bunch length by 2, i.e. going from 9 cm rms to 4.5 cm, would increase the power loss by a factor ~ 2000, i.e. going from 1 W to 2 kW! It is true that the power loss rapidly decreases with the frequency offset for high-Q resonances, as can be seen from Eq. (26), and therefore this could be a useful knob, but the problem is that in practice this offset is usually not known with sufficient precision and in the presence of many resonances this trick might not be possible.

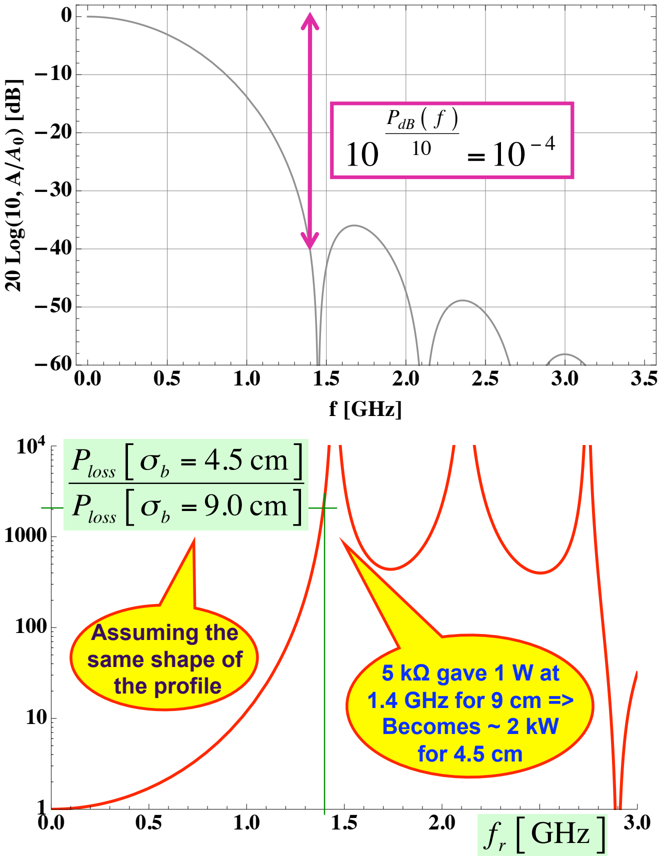

Fig. 11. Theoretical (see Fig. 9 with n = 3) longitudinal bunch spectrum (left) for the case of a LHC bunch in 2011 (9 cm rms bunch length) and power loss increase for the case of a bunch two times shorter (4.5 cm rms) assuming the same shape.

The usual solutions to avoid beam-induced RF heating are the following, depending on the situation:

- Increase the distance between the beam and the equipment.
- Coat with a good conductor if the heating is predominantly due to resistive losses and not geometric losses.
- Close large volumes (which could lead to resonances at low frequency) and add a smooth transition. This is why beam screens and RF fingers are installed.
- Put some ferrite with high Curie temperature and good vacuum properties (close to the maximum of the magnetic field of the mode and not seen directly by the beam) or other damping materials. Adding a material with losses (the type of ferrite should be optimized depending on the mode frequency), the width of the resonance will increase (the impedance will become broader) and the (maximum) impedance will decrease by the same amount. The power loss will therefore be (much) smaller. However, the ferrite will then have to absorb the remaining power. Even if much smaller, the heating of the ferrite can still be a problem if the temperature reached is above the Curie point, or is above the maximum temperature allowed by the device. To cool the ferrite one should try and improve the thermal conduction from the ferrite as

most of the time only radiation is used (given the general brittleness of the ferrite it is difficult to apply a big contact force).

- Improve the subsequent heat transfer:
    - Convection: there is none in vacuum.
    - Radiation: usually, the temperature is already quite high for the radiation to be efficient. One should therefore try and improve the emissivities of surrounding materials.
    - Conduction: good contacts and thermal conductivity are needed.
    - Active cooling: the LHC strategy (for instance) was to water cool all the near beam equipment.
- Try and design an All Modes Damper (AMD) if possible, to remove the heat as much as possible to an external load outside vacuum, where it can be more easily cooled away. This can also work together with a damping ferrite.
- Increase the bunch length. The longitudinal distribution can also play a very important role for some devices, and it should be kept under tight control.
- Install temperature monitoring on critical devices to avoid possible damages.

Following some issues with RF fingers on some LHC equipment in 2011 (as observed also before in other machines), a task force was set up during 2012 to review the design of all the components of the LHC equipped with RF fingers. The lessons learnt and the mitigation measures for the CERN LHC equipment with RF Fingers were reported in Ref. [128]. It is worth mentioning that for all the cases studied, no problem with impedance was revealed for conforming RF fingers. But the top priority for the future should be to try and reach robust mechanical designs to keep the contacts of all the RF fingers and to do a very careful installation (92 non-conformities were revealed in 2012 after an X-ray campaign).

Finally, in the presence of two counter-rotating beams as in the LHC collider, a general formula for the power loss at a location s around the accelerator has been recently computed. An integration over the beam screen length is needed to compute to total power loss in the beam screen (in W) and deduce an average power loss per unit length. This new formula involves the longitudinal impedances of both orders 0 and 1, the transverse offsets from the geometrical centre and the relative delay between the two beams. This new formula has been applied to the case of the current LHC and future HL-LHC triplets [129] and the resulting power was found to be very close to two times the power computed with one beam, i.e. there ws no significant interplay between the two beams.

4) Outlook

Many accelerators run now at the limit of stability and their impedance model need to be as precise as possible to be able to predict accurately their performance reach. For this reason, it is now fundamental to obtain all relevant wake or impedance contributions as a function of frequency and disentangle e.g. the driving, detuning and coupled terms contributions. In view of the many challenges that are experienced in all phases of building an impedance model, impedance related observables should be compared as much as possible with both bench measurements and beam-based measurements.

III. BEAM INSTABILITY THEORIES AND SIMULATIONS

A. Sacherer's and Laclare's approaches

Two approaches are usually used to deal with collective instabilities. One starts from the single-particle equation while the other solves the Vlasov equation, which is nothing else but an expression for the Liouville conservation of phase-space density seen by a stationary observer. In the second approach, the motion of the beam is described by a superposition of modes, rather than a collection of individual particles. The detailed methods of analysis in the two approaches are different, the particle representation is usually conveniently treated in the time domain, while in the mode representation the frequency domain is more convenient, but in principle they necessarily give the same final results. The advantage of the mode representation is that it offers a formalism that can be used systematically to treat the instability problem.

The first formalism was used by Courant and Sessler to describe the transverse coupled-bunch instabilities [130]. In most accelerators, the RF acceleration mechanism generates an azimuthal non-uniformity of the particle density and consequently the work of Laslett, Neil and Sessler for continuous beams [17] is not applicable in the case of bunched beams. Courant and Sessler studied the case of rigid (point-like) bunches, i.e. bunches oscillating as rigid units, and they showed that the transverse electromagnetic coupling of bunches of particles with each other can lead (due to the imperfectly conducting vacuum chamber walls) to a coherent instability. The physical basis of the instability is that in a resistive vacuum tank, fields due to a particle decay only very slowly in time after the particle has left (this leads to a long-range interaction). The decay can be so slow that when a bunch returns after one (or more) revolutions it is subject to its own residual wake field which, depending upon its phase relative to the wake field, can lead to damped or anti-damped transverse motion. For M equi-populated equi-spaced bunches, M coupled-bunch mode numbers exist ($n = 0,1,\ldots,M-1$), characterized by the integer number of waves of the coherent motion around the ring. Therefore the coupled-bunch mode number resembles the azimuthal mode number for coasting beams, except that for coasting beams there is an infinite number of modes. The bunch-to-bunch phase shift $\Delta\phi$ is related to the coupled-bunch mode number n by $\Delta\phi = 2\,\pi\, n\, /\, M$.

Pellegrini [131] and, independently, Sands [132,133] then showed that short-range wake fields (i.e. fields that provide an interaction between the particles of a bunch but have a negligible effect on subsequent passages of the bunch or of other bunches in the beam) together with the internal circulation of the particles in a bunch can cause internal coherent modes within the bunch to become unstable. The important point here is that the betatron phase advance per unit of time (or betatron frequency) of a particle depends on its instantaneous momentum deviation (from the ideal momentum) in first order through the chromaticity and the slip factor. Considering a non-zero chromaticity couples the betatron and synchrotron motions, since the betatron frequency varies around a synchrotron orbit. The betatron phase varies linearly along the bunch (from the head) and attains its maximum value at the tail. The total betatron phase shift between head and tail is the physical origin of the head tail instability. The head and the tail of the bunch oscillate therefore with a phase difference, which reduces to rigid-bunch oscillations only in the limit of zero chromaticity. A new (within-bunch) mode number $m = \ldots,-1,0,1,\ldots$ also called head-tail mode number, was introduced. This mode describes the number of betatron wavelengths (with sign) per synchrotron period.

The work of Courant and Sessler, or Pellegrini and Sands, was done for particular impedances and oscillation modes. Using the Vlasov formalism, Sacherer unified the two previous approaches, introducing a third mode number $q = \ldots,-1,0,1,\ldots$, called radial mode number, which comes from the distribution of synchrotron oscillation amplitudes [134,135]. The advantage of this formalism is that it is valid for generic impedances and any high order head-tail modes. This approach starts from a distribution of particles (split into two different parts, a stationary distribution and a perturbation), on which Liouville theorem is applied. After linearization of the Vlasov equation, one ends up with Sacherer's integral equation or Laclare's eigenvalue problem to be solved [135]. Because there are two degrees of freedom (phase and amplitude), the general solution is a twofold infinity of coherent modes of oscillation (m , $q = \ldots,-1,0,1,\ldots$). At sufficiently low intensity, only the most coherent mode (largest value for the coherent tune shift) is generally considered, leading to the classical Sacherer's formulae in both transverse and longitudinal planes. Note that contrary to the space charge case, these tune shifts are now complex, the imaginary part being linked to the instability growth rate. For protons a parabolic density distribution is generally assumed and the corresponding oscillation modes are sinusoidal. For electrons, the distribution is usually Gaussian, and the oscillation modes are described in this case by Hermite polynomials. In reality, the oscillation modes depend both on the distribution function and the impedance, and can only be found numerically by solving the (infinite) eigenvalue problem. However, the mode frequencies are usually not very sensitive to the accuracy of the eigenfunctions. Similar results are obtained for the longitudinal plane.

The most fundamental longitudinal instability encountered in circular accelerators is called the Robinson instability. The (Radio-Frequency) RF frequency accelerating cavities in a circular accelerator are tuned so that the resonant frequency of the fundamental mode is very close to an integral multiple of the revolution frequency of the beam. This necessarily means that the wake field excited by the beam in the cavities contains a major frequency component near a multiple of the revolution frequency. The exact value of the resonant frequency relative to the multiple of the revolution frequency is of critical importance for the stability of the beam. Above the transition energy, the beam will be unstable if the resonant frequency is slightly above it and stable if slightly below. This is the opposite below transition. This instability mechanism was first analyzed by Robinson [136]. Physically, the Robinson instability comes from the fact that the revolution frequency of an off-momentum beam is not given by the on-momentum revolution frequency, but by a quantity slightly different, depending on both the slip factor and the energy deviation. Let's assume in the following that the Robinson criterion is met. A bunch is longitudinally stable if the longitudinal profile observed at a wall-current monitor is constant turn after turn and it is unstable if the longitudinal profile is not constant turn after turn. In the case of instability, the way the longitudinal profile oscillates gives some information about the type of instabilities. This was studied in detail by Laclare [135], who explained theoretically such pictures of "longitudinal (single-bunch) instability" starting from the single-particle longitudinal signal at a pick-up electrode (assuming infinite bandwidth). Applying the Vlasov equation, linearizing it, and studying the effect of the impedance on the unperturbed distribution leads to the potential-well effect: a new fixed point is reached, with a new synchronous phase, a new effective voltage, a new synchrotron frequency, a new bunch length and a new momentum spread, which all depend on intensity. Studying a perturbation on top of the new stationary distribution, one ends up at low intensity, i.e. considering independently the modes m (which is valid up to a certain intensity), with an eigenvalue system to solve. The procedure to obtain first order exact solutions, with realistic modes and a general interaction, thus consists of finding the eigenvalues and eigenvectors of an infinite complex matrix. The result is an infinite number of modes of oscillation. To each mode, one can associate a coherent frequency shift (which is the qth eigenvalue), a coherent spectrum (which is the qth eigenvector) and a perturbation distribution. For numerical reasons, the matrix needs to be truncated, and thus only a finite frequency domain is explored. For the case of the parabolic amplitude distribution and a constant inductive impedance (which leads to real tune shifts only and therefore no instability), the signal at the pick-up electrode shown for several superimposed turns is depicted on Fig. 12. In the case of a complex impedance, the real part will lead in addition to a growing amplitude with an associated instability rise-time. It can be seen from Fig. 12 that there are q nodes on these "standing-wave" patterns.

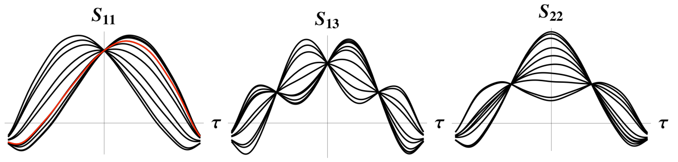

Fig. 12. Longitudinal signal S_{mq} at the pick-up electrode for three different modes shown for several superimposed turns (the red line corresponds to one particular turn), for the case of the parabolic amplitude distribution and a constant inductive impedance (exhibiting therefore no growing oscillations!).

Finding the eigenvalues and eigenvectors of a complex matrix by computer can be difficult in some cases, and a simple approximate formula for the eigenvalues is useful in practice to have a rough estimate. This is known as Sacherer's (longitudinal) formula [134]. Sacherer's formula is also valid for coupled-bunch instability with *M* equally-populated equally-spaced bunches, assuming multi-bunch modes with only one type of internal motion. In the case of gaps between bunch trains, a time-domain approach is usually better suited.

As the bunch intensity increases, the different longitudinal modes can no longer be treated separately and the situation is more involved. In the longitudinal plane, the microwave instability for coasting beams is well understood. It leads to a stability diagram, which is a graphical representation of the solution of the dispersion relation (taking into account the momentum spread) depicting curves of constant growth rates, and especially a threshold contour in the complex plane of the driving impedance [137]. When the real part of the driving impedance is much greater than the modulus of the imaginary part, a simple approximation, known as the Keil-Schnell (or circle) stability criterion, may be used to estimate the threshold curve [138]. For bunched beams, it has been proposed by Boussard to use the coasting-beam formalism with local values of bunch current and momentum spread [139]. A first approach to explain this instability, without coasting-beam approximations, has been suggested by Sacherer through Longitudinal Mode-Coupling (LMC) [140]. The equivalence between LMC and microwave instabilities has been pointed out by Sacherer and Laclare [135] in the case of broad-band driving resonator impedances, neglecting the potential-well distortion. Using the mode-coupling formalism for the case of a proton bunch interacting with a broad-band resonator impedance, and whose length is greater than the inverse of half the resonance frequency, new formulae have been derived taking into account the potential well-distortion due to both space charge and broad-band resonator impedances [141,142]. It is found in particular that due to the potential-well distortion, the beam is more stable below transition than above. Experimentally, the most evident signature of the LMC instability is the intensity-dependent longitudinal beam emittance blow-up to remain just below the threshold [143].

A similar analysis as the one done for the longitudinal plane can be done in the transverse plane [135]. Following the same procedure, the horizontal coherent oscillations (over several turns) of a "water-bag" bunch (i.e. with constant longitudinal amplitude density) interacting with constant inductive impedance are shown in Fig. 13 (here again the number of nodes correspond to the radial mode number *q*).

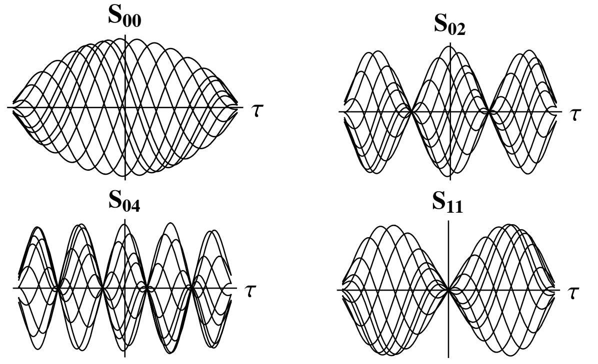

Fig. 13. Transverse signal S_{mq} at the pick-up electrode for four different modes shown for several superimposed turns, for the case of the "water-bag" bunch (i.e. with constant longitudinal amplitude density) and a constant inductive impedance. In the present example, the total phase shift between the head and the tail equal to 10.

The main difference with the longitudinal plane is that there is no effect of the stationary distribution and the bunch spectrum is now centred at the (transverse) chromatic frequency

$$f_{\xi_{x,y}} = Q_{x0,y0}\, f_0\, \xi_{x,y} \,/\, \eta \tag{27}$$

where $Q_{x0,y0}$ are horizontal and vertical low-intensity tunes and $\xi_{x,y}$ are the relative transverse chromaticities. The sign of the chromatic frequency is very important and to avoid the head-tail instability (of mode 0) it should be slightly positive, meaning that the chromaticity should be negative below transition and positive above. Sacherer's formula is also valid for coupled-bunch instability with *M* equally-populated equally-spaced bunches, assuming multi-bunch modes with only one type of internal motion (i.e. the same head-tail mode number). This analysis was extended in Ref. [144] to include also the coupling between the modes (and the possibility to have different head-tail modes in the different bunches). In the case of gaps between bunch trains, a time-domain approach is usually better suited.

As we saw before, at low intensity (i.e. below a certain intensity threshold), the standing-wave patterns (head-tail modes) can be treated independently. This leads to instabilities where the head and the tail of the bunch exchange their roles (due to synchrotron oscillation) several times during the rise-time of the instability. The (approximate) complex transverse coherent betatron frequency shift of bunched-beam modes is given by Sacherer's formula for round pipes [134]. For flat chambers, the effect of the quadrupolar impedance has to be added to obtain the real part of the coherent tune shift to be able to explain why the horizontal coherent tune shift is zero in horizontally flat chambers (of good conductors). As an example, a head-tail instability with 10 nodes is shown in Fig. 14 (upper). It is worth mentioning that there is also a head-tail instability in the longitudinal plane. The longitudinal head-tail instability, first suggested by Hereward [145] and possibly observed at the CERN SPS [146] results from the fact that the slip factor is not strictly a constant: it depends on the instantaneous energy error just as the betatron frequency does. The longitudinal beam distribution then acquires a head-tail phase, and instability may arise as a result.

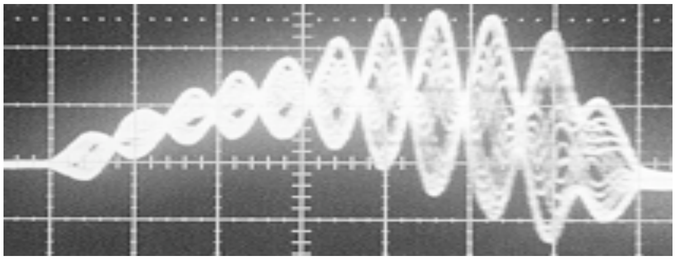

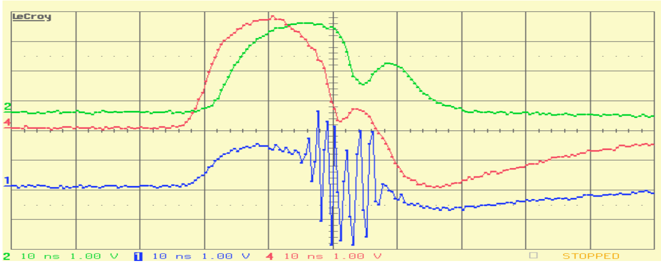

Fig. 14. (Upper) Signal from a radial beam position monitor during 20 consecutive turns observed in the CERN PS at 1.4 GeV kinetic energy in 1999. Time scale: 20 ns/div. (Lower) Fast instability observed in the CERN PS near transition (~6 GeV total energy) in 2000. Single-turn signals from a wide-band pick-up. From top to bottom: Σ, Δx, and Δy. Time scale: 10 ns/div. The head of the bunch is stable and only the tail is unstable in the vertical plane. The particles lost at the tail of the bunch can be seen from the hollow in the bunch profile.

As the bunch intensity increases, the different head-tail modes can no longer be treated separately. In this regime, the wake fields couple the modes together and a wave pattern travelling along the bunch is created (see e.g. Fig. 14 (lower)): this is the Transverse Mode Coupling Instability (TMCI). The TMCI for circular accelerators has been first described by Kohaupt [147] in terms of coupling of Sacherer's head-tail modes. This extended to the transverse motion, the theory proposed by Sacherer to explain the longitudinal microwave instability through coupling of the longitudinal coherent bunch modes. The TMCI is the manifestation in synchrotrons of the Beam Break-Up (BBU) mechanism observed in linacs. The only difference comes from the synchrotron oscillation, which stabilizes the beam in synchrotrons below a threshold intensity by swapping the head and the tail continuously. In fact, several analytical formalisms exist for fast (compared to the synchrotron period) instabilities, but the same formula is obtained (within a factor smaller than two) from five, seemingly diverse, formalisms in the case of a broad-band resonator impedance [148]: (i) Coasting-beam approach with peak values, (ii) Fast blow-up, (iii) BBU (for 0 chromaticity), (iv) Post head-tail, and (v) TMCI with 2 modes in the "long-bunch" regime (for 0 chromaticity). Two regimes are indeed possible for the TMCI according to whether the total bunch length is larger or smaller than the inverse of twice the resonance frequency of the impedance. The simple formula reveals the scaling with the different parameters, as, or a fixed impedance, the (e.g. vertical) intensity threshold is given by

$$N_{b,y}^{th} \propto \left| \eta \right| \varepsilon_l \, Q_{y0} \, . \qquad (28)$$

It can be seen in particular that the instability does not disappear at high energy but saturates like the slip factor (what is important is not the energy but the distance from the transition energy). This means that the TMCI intensity threshold can be raised by changing the transition energy, i.e. by modifying the optics. Furthermore, the intensity threshold increases linearly with the longitudinal emittance and the transverse tune. Note that the coherent synchrobetatron resonances, important in large machines, are not discussed here. This was checked with the MOSES code [149], which is a program computing the coherent bunched-beam mode. Below is a comparison between the MOSES code and the HEADTAIL code [150], which is a macroparticle tracking simulation code, in the case of a LHC-type single bunch at SPS injection [151]. As can be seen from Fig. 15, a very good agreement between the two was found. For a general impedance (i.e. not a resonator impedance) the situation is more involved and one should rely on HEADTAIL simulations. In the case of flat chambers, the intensity threshold is higher in one plane than in the other and linear coupling can be used to raise the TMCI intensity threshold [152]. Note finally that with many bunches the TMCI intensity threshold can be considerably reduced [144].

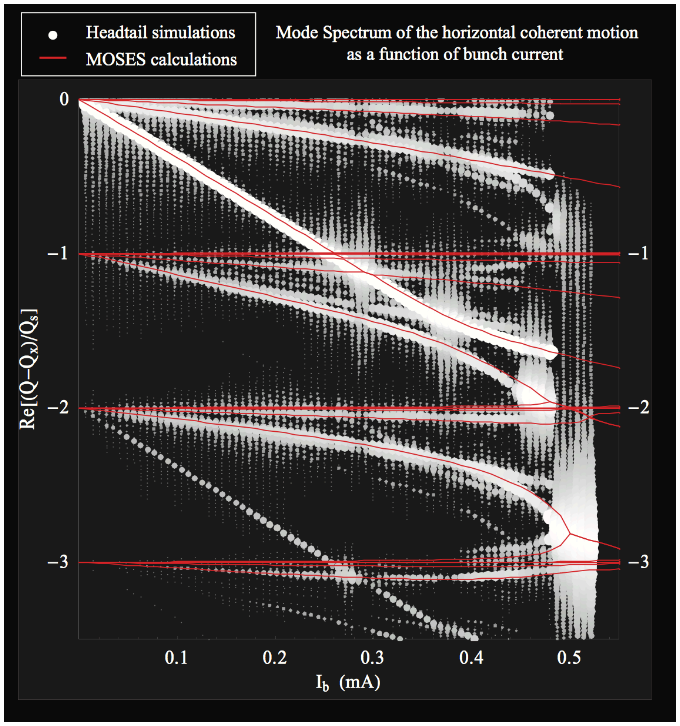

Fig. 15. Comparison between MOSES (in red) and HEADTAIL (in white) in the case of a broad-band resonator [151]. The evolution of the real parts of the shifts of the transverse modes (with respect to the unperturbed betatron tune and normalized by the synchrotron tune), is shown vs. bunch intensity.

It is worth mentioning also all the work done for the TMCI in LEP, as Chin's work (with MOSES) came later. It was proposed to cure the TMCI with a reactive feedback that would prevent the zero mode frequency from changing with increasing beam intensity [153]. In Refs. [154,155] a theory of reactive feedback has been developed in the two-particle approach and with the Vlasov equation. Theory has revealed that the reactive feedback can really appreciably increase the TMCI intensity threshold, which was confirmed by simulation [156,157]. On the contrary, the resistive feedback was found to be "completely" ineffective as a cure for the TMCI [155]. An action of a feedback on the TMCI intensity threshold was later examined experimentally at PEP [158]. It was confirmed that a reactive feedback is indeed capable to increase the TMCI intensity threshold. But it turned out unexpectedly that a resistive feedback can also increase the TMCI intensity threshold and even more effectively [158]. In Ref. [159], an attempt was made to develop an advanced transverse feedback theory capable to elucidate the conditions at which the resistive or reactive or some intermediate feedback can cure the TMCI. Positive chromaticity above transition helps, but depending on the coupling impedance, beam stability may require a large value of the chromaticity either unattainable or which reduces the beam lifetime. It was proposed to have a negative chromaticity (what is usually avoided), where the zero mode is unstable (by head-tail instability) and all the other modes are damped, and stabilise this mode by a resistive feedback, keeping the higher order modes stable.

Several stabilising mechanisms exist which can prevent the previous instabilities from developing. One of them is Landau damping, which is a general process that arises when one considers a whole collection of particles or other systems, which have a spectrum of resonant frequencies, and interact in some way. In accelerators we are usually concerned with an interaction of a kind that may make the beam unstable (wake fields), and we want to find out whether or not (and how) the spread of resonant frequencies will stabilise it. If the particles have a spread in their natural frequencies, the motion of the particles can lose its coherency. In fact, the origins of the frequency spread that leads to Landau damping need to be taken into account. The case where the frequency spread comes from the longitudinal momentum spread of the beam is straightforward (for a coasting beam), because the longitudinal momentum is a constant, which just affects the coefficients in the equations of motion of the transverse oscillations, and hence their frequencies: it is the distribution function which is important. The same result applies also if one considers a tune spread that is due to a non-linearity (e.g. from octupole lenses) in the other plane. However, this result is no longer valid if the non-linearity is in the plane of coherent motion. In this case, the steady-state is more involved because the coherent motion is then a small addition to the large incoherent amplitudes that make the frequency spread, and it is inconsistent to assume that it can be treated as a linear superposition [160]. One needs to consider "second order" non-linear terms and the final result is that in this case it is not the distribution function which matters but its derivative. Using the Vlasov formalism, this result is recovered more straightforwardly.

In the presence of tune spread (very often introduced by octupoles in the transverse plane, but other sources exist), the Landau damping mechanism of coherent instabilities is discussed through a dispersion relation. Without tune spread, the condition for the beam to be stable is simply that the imaginary part of the coherent tune shift is positive. In the presence of tune spread, a stability boundary diagram is defined, i.e. some beam stability can be reached even if the imaginary part of the coherent tune shift is negative: if the complex tune shift without tune spread is below the stability diagram, then the beam is stable. It is worth reminding that Landau damping of coherent instabilities and maximization of the dynamic aperture are partly conflicting requirements. On the one hand, a spread of the betatron frequencies is needed for the stability of the beam coherent motion, which requires nonlinearities to be effective at small amplitude. On the other hand, the nonlinearities of the lattice must be minimized at large amplitude to guarantee the stability of the single-particle motion. A trade-off between Landau damping and dynamic aperture is therefore usually necessary. Note that some work is being done to use the nonlinear optics as a path to high intensity, providing "infinite (transverse) Landau damping" [161]. The case of additional space charge nonlinearities is discussed later in this paper.

Note that linear coupling between the transverse planes can also influence the Landau damping mechanism [162], leading to a sharing of the Landau damping between the transverse planes, which can have a beneficial effect (i.e. stabilising the other plane) or a detrimental effect (i.e. destabilising one or two planes, as it was believed to be the case with the Batman instability of the HERA proton ring [163]). Furthermore, one has also to be careful with linear coupling as it modifies the transverse emittances [164,165].

Similarly, Landau damping is an important stabilizing mechanism in the longitudinal plane. When the bunch is very small inside the RF bucket, the motion of the particles is linear and all the particles have the same (unperturbed, maximum) synchrotron frequency. By increasing the bunch length the incoherent synchrotron frequency spread is increased (the maximum synchrotron frequency spread is obtained when the bunch length is equal to the RF bucket length as in this case the synchrotron frequency of the particles with the largest amplitude is equal to 0.

B. *Longitudinal Instabilities in the CERN SPS*

1) Microwave instability

There is a very wide range of phenomena in high-intensity circular accelerators that are called by the same name "microwave instability". Usually, but not always, an instability is called microwave if

$$f_r \, \tau >> 1, \tag{29}$$

where τ is the (full) bunch length and f_r is the resonant impedance frequency (or the central frequency where the instability develops). In proton accelerators the microwave instability is observed as a fast increase of the bunch length and thus of the longitudinal emittance ε_l. This bunch lengthening can be distinguished from the bunch lengthening due to potential well distortion by an increase in the slope of bunch length versus intensity. The break point where the slope changes is considered as the instability threshold.

The fast (with respect to the synchrotron period) microwave instability threshold can be estimated for a broad-band impedance using the Keil-Schnell-Boussard criterion. However, when applied to the SPS case in the past, a much lower threshold in intensity was obtained [166]. Indeed, the SPS impedance model is very far from the broad-band resonator (see later). Analytical solutions for the instability thresholds can be calculated for a fast instability growth for a bunch with Gaussian distribution in the limiting cases of a broad-band ($f_r \; \tau >> Q$) or narrow-band $f_r \; \tau << Q$) resonant impedance [166,167]. For the instability threshold of a single bunch in a single RF system defined by the interaction with a narrow-band resonator it is the value of $R_{\mathrm{sh}} \,/\, Q$ which is important. However, for a broad-band impedance $R_{\mathrm{sh}} \,/\, n_r$ is more relevant, where n_r is the harmonic number of the resonant impedance, $n_r = f_r \,/\, f_0$. Macroparticle simulations were carried out to verify this prediction, using the code

BLonD [168]. The simulation was set up to match the experimental conditions at SPS flat top. The initial matched distribution was created iteratively and the particles were then tracked for 1.15 s (around twice the time of the SPS flat top). The criterion used to estimate the threshold was based on the bunch length growth and on its oscillation amplitude at the end of the simulation. In particular, the bunch was considered unstable when the final bunch length is larger than 5% of the initial bunch length or the maximum bunch length oscillation amplitude is larger than 100 ps. Initially, the case with a single RF system was studied. In order to compare with the above-mentioned analytical predictions, a resonator with $f_r = 1.4$ GHz and the same $R_{sh} / Q = 10$ kΩ was used, while the value of Q (and R_{sh}) was scanned. The simulation results are summarized in Fig. 16, where the instability threshold as a function of bunch emittance is plotted.

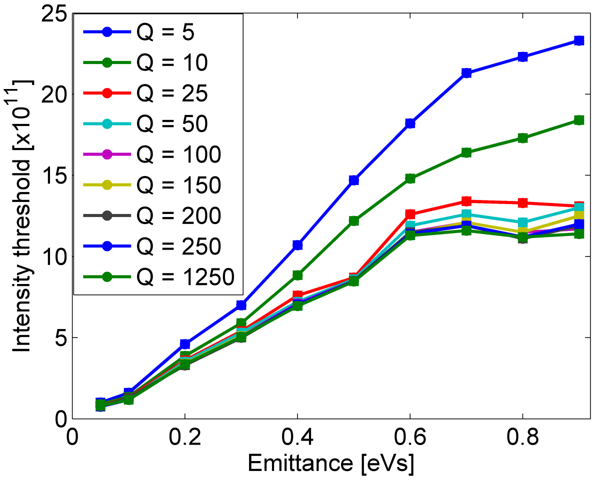

Fig. 16. Instability threshold as a function of intensity for different Q values, found in simulations for a single bunch at SPS flat top (450 GeV/c) in single RF and for a resonator with $f_r = 1.4$ GHz and $R_{sh} / Q = 10$ kΩ. The voltage $V_{200} = 2$ MV.

For $Q \geq 50$ the instability threshold is practically unchanged, confirming the fact that only R_{sh} / Q is important for the bunch stability when the resonator is in the narrow-band regime. Note that for all the simulated bunches $f_r \tau < 4 << 50$. Instead, when $Q < 50$, R_{sh} becomes important for stability since the resonator approaches the broad-band regime. As a consequence, for instability in narrow-band impedance regime, damping the resonator does not help much since R_{sh} / Q stays constant. In particular, a damping of more than a factor 50 should be achieved in order to increase the instability threshold. Similar dependence on R_{sh} / Q and Q was also found for a double RF system when the harmonic and the voltage ratios are $h_2 / h_1 = V_1 / V_2 = 2$. The two operating modes of the double RF system were studied, namely the bunch-shortening mode (BSM) and the bunch-lengthening mode (BLM) in which, above transition, the phase between the two RF systems is π and 0, respectively. The results for $Q = 250$ are presented in Fig. 17, together with the single RF case for comparison.

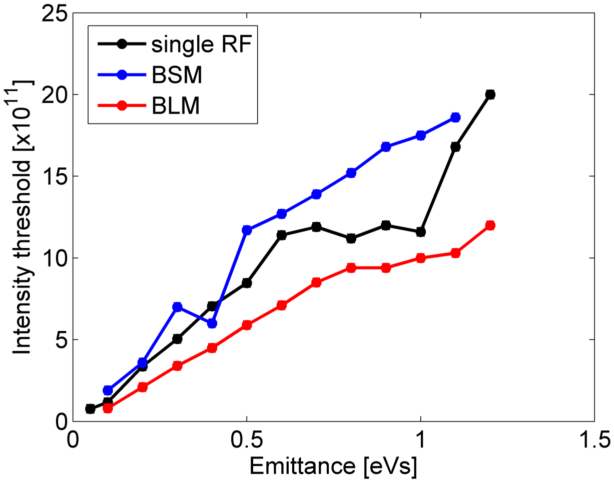

Fig. 17. Instability threshold as a function of intensity found in simulations for a single bunch at the SPS flat top (450 GeV/c) in single and double RF systems (BSM and BLM) with $h_2 / h_1 = V_1 / V_2 = 2$. A resonator with $Q = 250$ and $R_{sh} / Q = 10$ kΩ was used as an impedance source. The voltages $V_{200} = 2$ MV and $V_{800} = 1$ MV.

From microwave theory, it is expected that the instability threshold increases with relative momentum spread $\Delta p / p$ inside the bunch [138,148,166,167]. The fact that BSM, which has the maximum value of $\Delta p / p$, has the highest threshold is in line with this. Similarly, BLM has the lowest threshold amongst the three cases. However, the previous result is not valid anymore when the harmonic ratio between the two RF systems is $h_2 / h_1 = 4$, as presently in the SPS. Particle simulations performed for this harmonic ratio and for two different voltage ratios showed that above a certain emittance the instability threshold is higher in a single RF system (see Fig. 18).

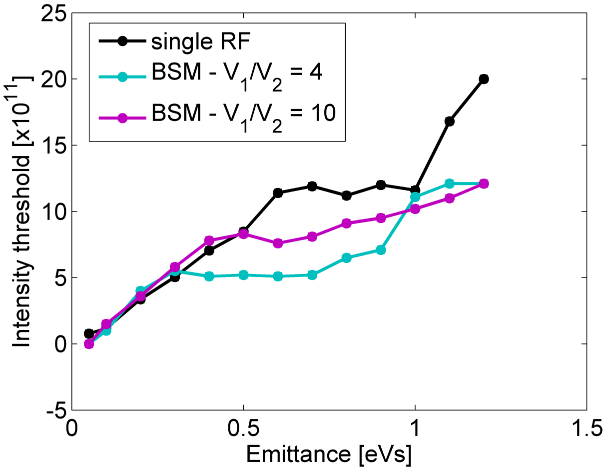

Fig. 18. Instability threshold as a function of intensity found in simulations for a single bunch at SPS flat top (450 GeV/c) in single and double RF systems (BSM) with $h_2 / h_1 = 4$. A resonator with $Q = 250$ and $R_{sh} / Q = 10$ kΩ was used. The voltage $V_{200} = 2$ MV.

A possible explanation of this fact can be obtained by inspecting the synchrotron frequency distribution inside the bunch f_s (J), where J is the action (similar to the longitudinal emittance ε_l). Examples of distributions calculated for a bunch of $\varepsilon_l = 0.6$ eVs are presented in Fig. 19. Note that $\varepsilon_l = 0.6$ eVs corresponds to the typical emittance of LHC-type proton beams at SPS flat top. As one can see, in BSM, there are regions with zero derivative in the tails of the bunch which can reduce significantly the loss of Landau damping threshold [169,170]. This is discussed in the next section.

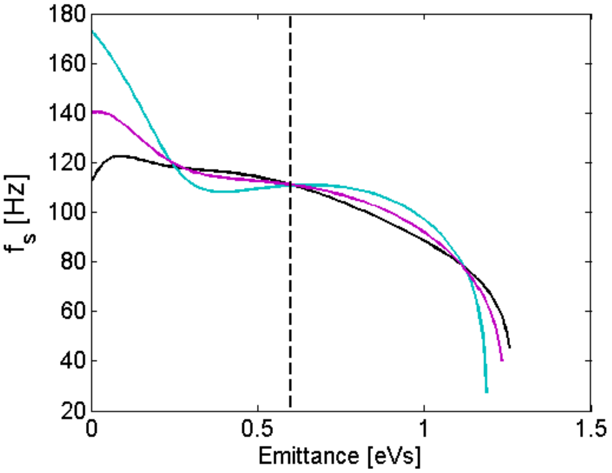

Fig. 19. Synchrotron frequency distribution inside the bunch, corresponding to the points with $\varepsilon_l = 0.6$ eVs in Fig. 18, with the same color convention.

2) Loss of Landau damping

Previous studies of beam stability in a double RF system already pointed out that in the BLM Landau damping can be lost for particles in the region where the synchrotron frequency distribution has its maximum outside the bunch center [171,172]. This region was also creating problems in the beam control of the CERN PS Booster due to the large coherent signal in a double harmonic RF system [173]. Indeed, large amplitude coherent response was measured in beam transfer function (BTF) in the BLM at frequencies corresponding to the maximum of the distribution [174]. Recently, an analytical approach made it possible to find this threshold through the onset of a discrete Van Kampen mode (coherent mode without Landau damping) by solving numerically the linearized Vlasov equation [169]. The latter method is used in [170], together with macroparticle simulations for inductive impedance, to explain the observations in the SPS during the ppbar operation. Only the dipole modes are addressed since they are expected to have the lowest threshold and no coupling between different azimuthal modes is considered. Two RF systems of 100 MHz and 200 MHz are used with voltage amplitudes $V_{100} = 0.6$ MV and $V_{200} = 0.3$ MV, while for the phase-space density a parabolic distribution was used, close to the one fitted to measurements. The intensity threshold of the loss of Landau damping N_{th}, for different longitudinal emittances in a double RF (BLM, BSM) and a single RF systems is shown in Fig. 20.

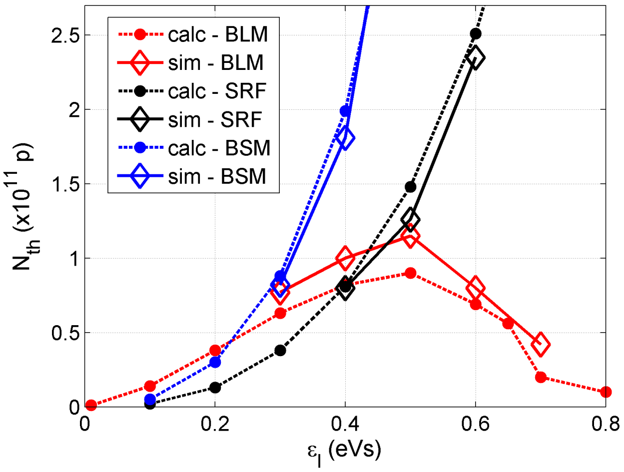

Fig. 20. Loss of Landau damping thresholds versus bunch emittance for a double RF (BLM - red, BSM - blue) and a single RF (black) systems found from calculations (dots) and simulations (diamonds). Application for the SPS during the ppbar operation at injection energy (26 GeV/c). Voltage ratio between the two RF systems at $V_1 / V_2 = 2$.

For the BLM, one can see that N_{th} increases with ε_l until some value of ~ 0.5 eVs. After this point further increase in ε_l leads to threshold reduction. In fact, an inspection of the incoherent synchrotron frequency distribution, see Fig. 21 (red curve), shows that the flat region where the derivative of the distribution is 0 (vertical line) corresponds to the critical emittance $\varepsilon_{cr} = 0.65$ eVs.

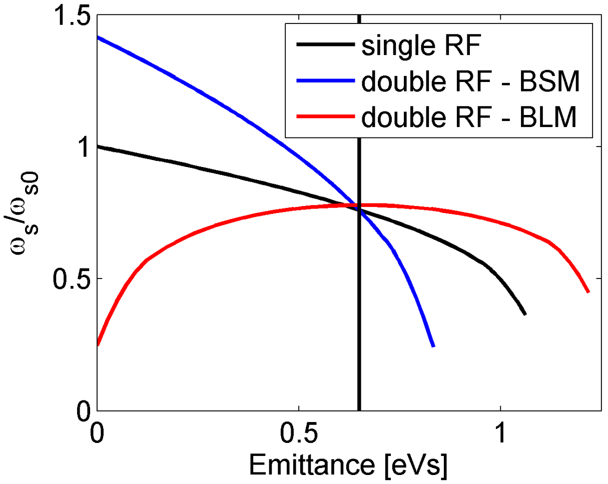

Fig. 21. Relative synchrotron frequency distribution for a double RF (BLM - red, BSM - blue) and a single RF (black) systems. No intensity effects are included. The vertical line at 0.65 eVs indicates the maximum of the BLM curve. Similar conditions as in Fig. 20.

This result can actually explain the un-damped oscillations at the injection plateau during the ppbar operation, since for the nominal (0.65 eVs) or larger emittances the threshold for the loss of Landau damping is very low [175]. Although the spread inside the bunch is still big, the lack of stability in this case is determined by the non-monotonic behavior of the distribution function in the tails of the bunch. On the other hand one can see that for a double RF in BSM and a single RF the intensity threshold keeps increasing with the emittance, as was expected from the monotonic behavior of their distribution functions shown in Fig. 21. For bunches with $\varepsilon_l < 0.2$ eVs, the BLM is the preferable mode at operation, while after this value the threshold of the BSM is rapidly increasing, making this mode a better choice for stability. However, it is clear from Fig. 22 that the BSM is unacceptable above 0.6 eVs due to lack of longitudinal acceptance, which would lead to significant particle losses. For $\varepsilon_l > 0.6$ eVs, a single RF seems to be the best option. Similar results were obtained in [169] for a resistive wake where again the threshold for loss of Landau damping in BLM is the highest for small emittances but for higher emittances drops first below the threshold in BSM and then below the single RF case.

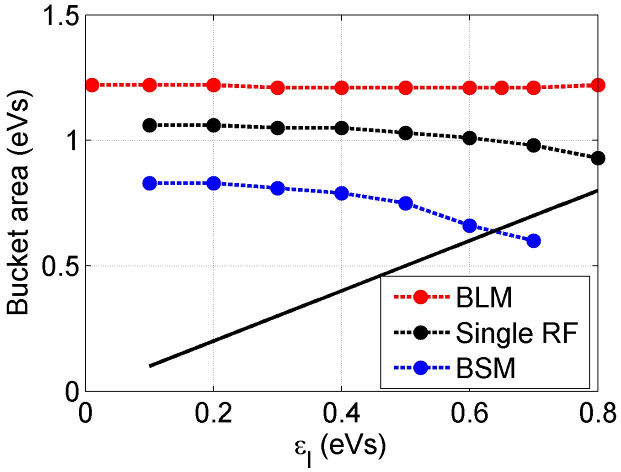

Fig. 22. Bucket area versus emittance for a double RF (BLM - red, BSM - blue) and a single RF (black) in the cases corresponding to the intensity threshold in Fig. 20. The black straight line is the limit where ε_l is equal to the bucket area.

C. *Beam Instability Macroparticle Simulations*

Numerical simulations have always been an important tool to understand the physics of collective effects in particle accelerators leading to beam instabilities and thus brightness limitations. Moreover, they are a valuable means to evaluate and propose mitigation techniques to improve these limitations. In the past, simulation tools were often geared to modelling certain types of collective effects. There were for example specialized codes to study the effect of beam-beam interactions, other codes were more focused on the interaction of a beam with impedances and yet others were used to investigate electron cloud effects. The understanding of the individual effects has improved by a large amount such that the combination of the different effects is becoming increasingly important. To systematically study these combined effects on the beam stability, it is mandatory to bring together all the specific features of collective effects simulation codes.

1) *pyHEADTAIL*

PyHEADTAIL is a recently developed simulation code that is based on the HEADTAIL code [150] written in 2000 and originally designed to study electron cloud instabilities in circular accelerators. At a later stage, the HEADTAIL code was branched into a separate version intended to study the effect of impedances on beam dynamics in greater depth. The two versions of the code coexisted and were used to study the different types of instabilities separately. New effects and features were continuously added to enhance the beam dynamics model of either one of the versions. Concerning the code addressing the study of impedance effects, the newly added features covered e.g. the influence of multi-turn wake fields as well as the multi-bunch treatment. For the electron cloud version on the other hand, the modeling of wideband feedback systems was a major enhancement of the code. At a certain point during this evolution, the idea emerged to separate the different portions of the code into independent modules, each representing a separate physical phenomenon. This would drastically ease the maintenance of the code, allow to separately develop individual modules and, moreover, would greatly improve the extensibility, i.e. the possibility to easily add new modules to treat new physical phenomena without having to thoroughly engage into the rest of the code. In addition, the idea was to make the simulations scriptable. A simulation would no longer be statically controlled via an input file. Instead, different modules of the code are combined in a custom tailored script with all the necessary control flow tools provided. One therefore designs specific simulations that can be managed dynamically at run time. This led to the creation of PyHEADTAIL.

The physical drift/kick model of PyHEADTAIL was largely adopted from HEADTAIL. The model treats the accelerator ring as a collection of interaction points distributed along its circumference. The interaction points are connected by ring segments. Hence, the ring is naturally split into a set of segments with an interaction point at the end of each segment where one or more collective effects take place as outlined in Fig. 23.

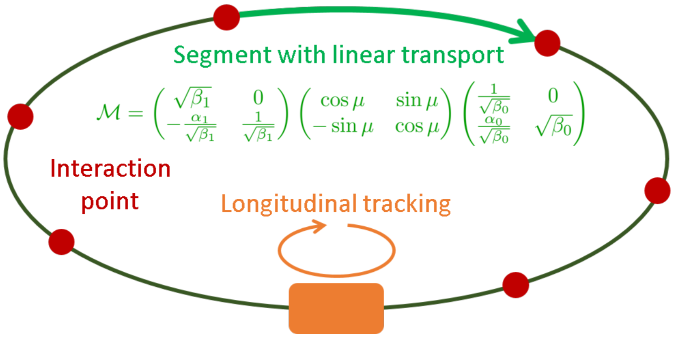

Fig. 23. Scheme of the drift/kick model adopted for PyHEADTAIL.

A beam is modeled as a set of macroparticles, each represented by a charge, a mass and the generalized coordinates and corresponding canonically conjugate momenta. It is transported along one segment from one interaction point to the next via the linear transport map, which takes into account the local Twiss parameters and the dispersion at each interaction point. Non-linear tracking features are not directly included in the form of non-linear kicks. Instead, the effects of any non-linearities on the incoherent detuning are wrapped into global machine parameters such as chromaticity or anharmonicities, for example. Each segment then provides an additional detuning to each individual macroparticle in accordance with the specified chromaticities or anharmonicities, etc. This treatment is crucial for collective effects to correctly model head-tail instabilities or Landau damping. The longitudinal coordinates and momenta are updated via the symplectic Verlet integration scheme consisting of a half drift, a kick and again a half drift. PyHEADTAIL features acceleration as well as multi-harmonic RF systems. Collective effects are applied at the end of each segment. Typically, these effects are correlated with the longitudinal position of particles within the beam. To make the computations numerically efficient, a beam is longitudinally binned into a set of slices via a 1D particle-in-cell (PIC) algorithm. A single slice is then thought to be representative for all the macroparticles contained within. Collective effects are correspondingly applied to the macroparticles on a slice-by-slice basis. To date, the implemented types of collective effects cover (multi-turn) wake fields, a transverse damper, wideband feedback systems, space charge and electron cloud. The algorithms that are implemented to treat the individual collective effects range from simple convolutions, used e.g. to determine the action of wake fields, to 2D Poisson solvers needed to compute the electron cloud interaction. The latter are also able to account for complicated geometrical boundaries using the Shortley-Weller finite difference (FD) scheme [176].

The programming language of choice to write PyHEADTAIL was Python. Python is a modern, general-purpose, high-level programming language that supports multiple programming paradigms. It is widely spread and supported and contains a large set of third party libraries specialized for scientific computing, most importantly to be mentioned here, the NumPy and SciPy packages. Moreover, it can be interfaced with Fortran or C routines via F2PY or Cython to speed up computationally demanding parts of the code and thus to overcome performance bottlenecks. Python has a clear and simple syntax and is said to considerably reduce the lines of code when compared with classical lower level languages such as C/C++. For these reasons, code readability and understanding is drastically improved, which reduces the chance of implementing bugs and significantly enhances both maintainability and extensibility of the code. For the general architecture of PyHEADTAIL it was thus decided to have the code layout and structure managed in Python and to provide crucial inner-loop functions in Fortran or C where computational speed-up is needed. Currently, efforts are on-going to offer optional parallelization of PyHEADTAIL via OPEN-MP (for multi-CPU-core usage) as well as CUDA (to benefit from GPU hardware acceleration). The PyHEADTAIL design opts to be a direct mapping of the underlying physical model. An object-oriented approach was chosen to ease the internal organization of the code and help in providing the desired modularity. The idea is that each physical entity or phenomenon should be represented by a class, each containing its specific attributes and methods to handle any processes specific to this object. Roughly, the classes available in PyHEADTAIL can be categorized into beam objects and machine objects. A beam object represents the physical beam as a set of macroparticles. The basic attributes of this set of macroparticles are the number of macroparticles together with the number of physical particles to be represented. Furthermore, there are the particle charge and mass and, finally, a set of generalized coordinates and the corresponding canonically conjugate momenta of all the macroparticles. The available beam methods include functions to evaluate beam properties such as the beam energy or the emittance. A machine object on the other hand knows how to handle a beam by modifying any of the beam attributes accordingly. This could for instance be the reduction of the number of macroparticles and physical particles of a beam by an aperture element or the update of the phase space coordinates of the beam particles by a tracking element. The general philosophy is that any machine object should have a "*track*" method that accepts a beam object as the only argument. The internal tracking routine would then depend on the individual machine object but the interface for tracking a beam is common to all machine classes. To assure this interface, any new machine-type class is derived from an abstract base class, which requires a *track* method with the given interface. That way, any new feature representing a physical phenomenon acting on the beam can easily be added as a machine-type class. Machine objects perform a variety of operations on the beam. Some examples are:

- Transverse tracker: transports a beam along a ring segment by updating its transverse coordinates and momenta using a linear transport map according to the local Twiss parameters of the machine;
- Longitudinal tracker: transports a beam once around the full ring by updating the longitudinal coordinates via a Verlet integration scheme;
- Wake field: applies wake field interaction with a beam by updating the beam momenta after the convolution with a given wake field;
- Aperture: removes particles from the beam according to the provided aperture restrictions.

Apart from the beam and machine classes, there are Slicer objects that perform the longitudinal binning of the beam. They do not need to be explicitly called by the user, but are used internally by some of the machine-type classes in PyHEADTAIL. Furthermore, there are various monitor classes that allow the user to save the evolution of the beam state during the simulation in the HDF5 file format. The chosen design not only eases maintenance and extendibility of the code, but also allows for a flexible workflow for simulations. When setting up a simulation, which fully takes place in a Python scripting environment, all the PyHEADTAIL modules required for the simulation are imported first. The objects needed for the simulation are then instantiated with their specific interfaces ensuring that all the necessary parameters are provided. The design is set up such that all the machine object instances can simply be linked together to a list of accelerator element maps. That way, any combination of machine elements can be easily built allowing to study a wide variety of different configurations. The simulations are individually adaptable and the study of the combination of different collective effects becomes trivial at least in terms of setting up and performing the simulation. The code snippet responsible for the actual tracking consists of only three lines as depicted in Fig. 24.

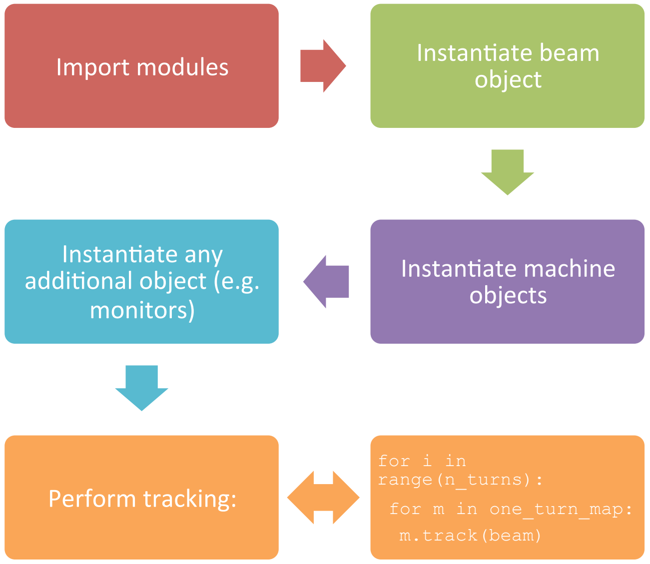

```
for i in
range(n_turns):
 for m in one_turn_map:
  m.track(beam)
```

Fig. 24. Typical workflow when setting up a PyHEADTAIL simulation.

Some of the applications are described below. One of the big advantages that come with running simulations in a scripting language is the dynamic control over the simulation process. For example, it is possible to access instance variables representing simulation parameters and to modify them at run time. This allows to seamlessly implement trim functions into the simulation. In principle, real machine cycles can thus be realistically simulated. One example where dynamically changing parameters have been employed is the creation of longitudinally hollow bunches in the CERN PSB. Here, a double harmonic RF system is used to shape the beam to a hollow ring in the longitudinal phase space. Correspondingly, this distribution features a flattened line charge density, which effectively mitigates transverse space charge, an important player at the low beam energies of the PSB or the PS at CERN. To achieve the flat bunch profile, the RF parameters need to be dynamically adjusted in the machine. The trim functions are shown in Fig. 25 and have been adopted in the simulations. It was shown that with these trim functions the hollow bunches could be reproduced in simulations. In a second step, the effect of longitudinal space charge was added and its impact on the formation of hollow bunches could be studied in detail. An example result obtained from such a simulation is shown in Fig. 26.

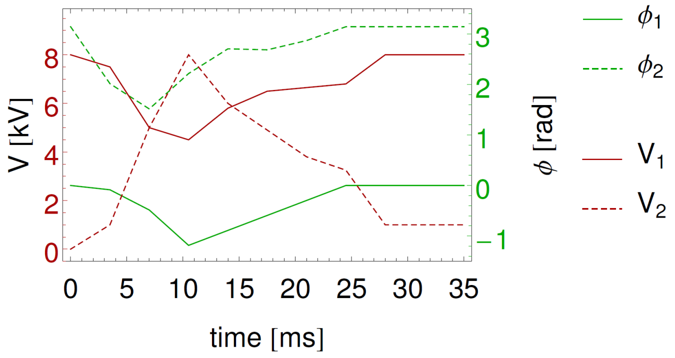

Fig. 25. Trim functions for the double harmonic RF systems. The plot shows the time evolution of the voltage (red) and phase (green) of the first (solid) and the second (dashed) harmonic RF systems.

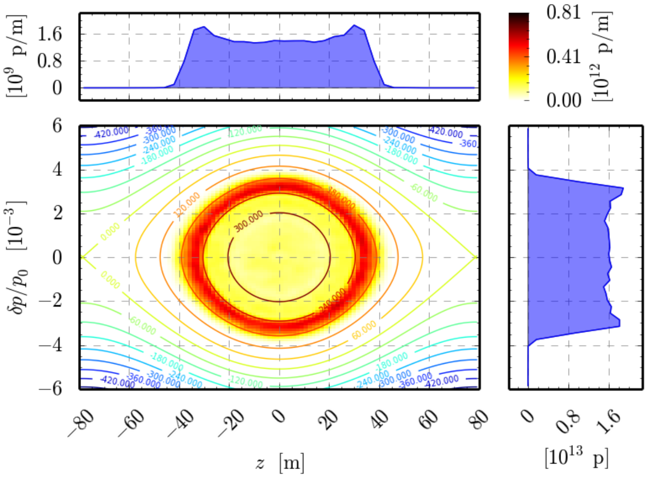

Fig. 26. Hollow bunch shape in longitudinal phase space after having applied the trim functions shown in the figure above. The line density profile becomes flat.

An example of the benefits coming with the modular design of the code is the creation of an interface to PyECLOUD [177], which is a macroparticle simulation code (see also later) to model the build-up of electron clouds in circular accelerators due to multipacting (the exponential growth of the number of electrons from amplification due to secondary emission from the inner surface of vacuum chambers). It has been widely used in the past to study the formation of electron clouds in different machines with their specific beams and has also been benchmarked against experiments. It features a sophisticated multipacting model and FD PIC solvers to model the collective interaction of electrons among each other and with the passing beam. Both the multipacting algorithm as well as the PIC solvers account for non-trivial boundary geometries. PyECLOUD includes a Boris tracker (global bound on energy error, though not symplectic) in order to correctly handle and resolve the electron dynamics in arbitrary magnetic fields. This allows studying the electron cloud build-up in the vacuum chambers of dipole or quadrupole magnets, for example (see Fig. 27). For the study of electron cloud induced instabilities it is therefore natural to reuse all the existing features of PyECLOUD. For this, all that needed to be done was to provide PyECLOUD with a beam tracking algorithm together with an interface to PyHEADTAIL. Due to the orthogonal design of the PyHEADTAIL modules, no additional knowledge of any of the other modules was necessary for the successful integration of PyECLOUD. This made the inclusion of an entire separate code seamless and drastically reduced the probability of introducing any bugs in any of the working routines. Equipped with this additional feature, PyHEADTAIL was used to study electron cloud instabilities in different vacuum chambers with different magnetic field configurations for the SPS at CERN. It is also being used to study the beam stability in presence of electron clouds in the quadrupoles of the LHC and the HL-LHC, where the high beam energies generate very fast cyclotron motion of the electrons which makes the correct modeling of the electron motion numerically very challenging.

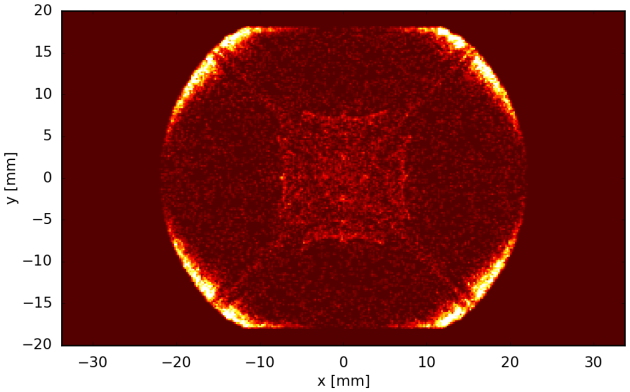

Fig. 27. Electron cloud pinch in a vacuum chamber within a quadrupolar magnetic field. Bright spots indicate regions with high electron cloud densities.

In summary, to satisfy the needs of future studies of collective beam instabilities, which are increasingly focused towards investigating the combination of different collective effects, modern numerical simulation tools should provide simple and flexible ways to set up and perform studies of a variety of scenarios. With contemporary availability of computational power and modern scripting languages such as Python, PyHEADTAIL has been developed as a recent advancement of the original HEADTAIL code. It has been extended by additional features such as an improved, detailed treatment of electron cloud effects and has been applied to simulated scenarios, which would have been extremely hard to realize within the classical framework of HEADTAIL. The approach taken in the design of PyHEADTAIL is representative for modern numerical simulation tools for the study of collective beam instabilities. These tools are geared towards ease of maintenance and extendibility and provide the necessary flexibility to simply design customized simulations for the study of increasingly complex scenarios and the interplay of a variety of collective effects.

2) *pyECLOUD*

Secondary electron emission in resonance with an alternating electric field can lead to avalanche electron multiplication. The underlying mechanism is called multipactor effect. Although desirable for some applications [178], it is usually associated with deleterious effects, such as voltage breakdown in radio frequency (RF) devices, outgassing, surface heating [179-181]. In the case of a particle accelerator operated with closely spaced bunches multipactor effects can occur in the beam chambers leading to the formation of so called Electron Clouds (EC) with several negative effects on the machine performances [182-186]. EC effects have been observed in several accelerators all over the world, much more commonly in those operated with positively charged particles (e.g. positrons, protons, heavy ions), and are presently among the major performance limitations for high energy colliders, like the Relativistic Heavy Ion Collider (RHIC) in the USA [187], the KEKB electron positron collider in Japan [188], the DAΦNE electron positron collider in Italy [189] and, more recently, the CERN LHC [190]. A qualitative picture of the EC buildup at a section of an accelerator operated with bunches of positively charged particles is sketched in Fig. 28 (see also [191]).

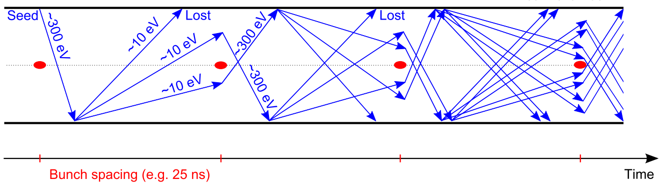

Fig. 28. Schematic of the formation of an electron cloud in a particle accelerator (a similar sketch can be found in [191]).

The circulating beam particles can produce electrons due to different mechanisms, e.g. ionization of the residual gas in the beam chamber or photoemission from the chamber's wall due to the synchrotron radiation emitted by the beam. These are called “primary or seed electrons”. Seeds are attracted by the passing particle bunch and can be accelerated to energies up to several hundreds of eV. When an electron with this energy impacts the wall, “secondary electrons” are likely to be emitted. The secondaries have energies up to few tens of eV and, if they impact the wall with these energies, they are either absorbed or elastically reflected but cannot produce any secondary. On the other hand, if they survive until the passage of the following bunch they can in turn be accelerated, projected onto the wall and produce secondaries. This can trigger an avalanche multiplication effect which builds up the EC during the passage of an entire bunch train. The presence of EC in the beam chamber can limit the achievable performance of a particle accelerator through different effects, which will be briefly reviewed in the following (all these effects have been observed at the LHC and in its injector chain, as described in detail in [190]):

- Transverse beam instabilities: the forces exerted by the EC on the particle beam can drive transverse instabilities (e.g. exponentially growing oscillation of the particle around the nominal trajectory). Both “coupled bunch'” instabilities and intra-bunch motion [192] can be observed leading to fast transverse emittance blowup and particle losses, which in many cases can prevent a safe operation of the accelerator. Due to the important high frequency content, the conventional transverse feedback systems are usually ineffective in controlling EC induced instabilities. Better results can be obtained introducing Landau damping [192] through high chromaticity settings or using octupole magnets, typically at expense of transverse emittance preservation and beam lifetime [193,194].
- Incoherent beam effects: even when transverse instabilities can be avoided (either because the EC density is low enough, or thanks to Landau damping) the interaction of the beam with the EC can drive incoherent effects e.g. slow emittance blow up, particle losses, transverse tune spread, which are particularly worrying in storage rings and particle colliders where the aim is to store the beam in the ring for a very long time (several hours) while preserving the beam quality.
- Vacuum degradation: the electron flux on the chamber's wall stimulates the desorption of gas molecules from the

surface which results in an increased residual gas density in the beam chamber, and therefore in a pressure increase. This has several deleterious effects like larger equipment irradiation, worse background in the experimental areas, increased probability of breakdown in high voltage devices like kickers or electrostatic septa, and impact on the beam lifetime [195].

- Heat load: the electrons also deposit energy on the chamber's wall. While this effect is typically negligible in room temperature accelerator components, it can become a serious issue in devices operating at cryogenic temperature like the superconducting magnets of the LHC, where the EC induced heat load can reach the cooling capacity limit of the cryogenic system [196].
- Impact on beam diagnostics: the presence of an unforeseen electron flux can induce malfunctions on beam diagnostics devices like pickups and Beam Position Monitors [197].

The analysis of EC observations in the LHC and its injectors has raised new challenges for the EC build-up simulations. For a correct understanding of machine observations it is often necessary to deal with beams with thousands of bunches and with non idealities like non uniform bunch populations and bunch lengths along the beam. Beside the usual simulation scenarios of field free regions and dipole magnets, also more complex situations needed to be addressed, like the EC buildup in quadrupoles or combined function magnets and with two counter-rotating beams in the same chamber. Moreover, the demand for extensive parameter scans gave quite stringent requirements in terms of speed and reliability. CERN has a long experience in the EC build-up simulation, mostly carried out with the ECLOUD code, developed and maintained at CERN since 1997 [191,198,199,150] and, more recently, a fully reorganized simulation code has been developed in order to better fulfill the aforementioned requirements. The new code has been called PyECLOUD, since it is almost entirely written in Python and inherits the physical models of the ECLOUD code.

PyECLOUD is a 2D code that simulates the EC buildup in a thin slice around a certain section of a particle accelerator. Electrons are grouped in MacroParticles (MP) in order to achieve a reasonable computational burden and the dynamics of the MP system is simulated following the flow diagram sketched in Fig. 29.

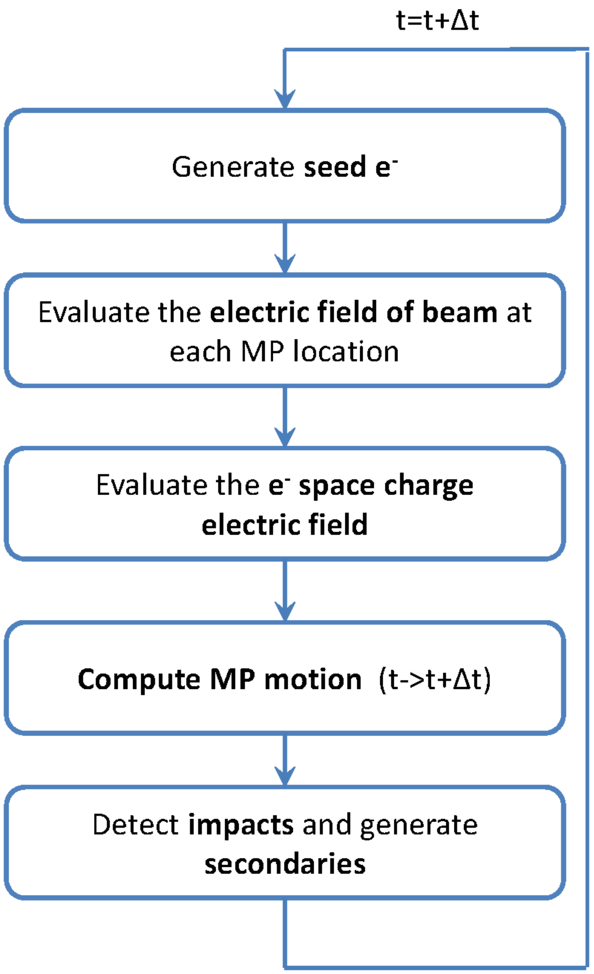

Fig. 29. Flowchart representing PyECLOUD main loop.

At each time step, seed electrons due to residual gas ionization and/or to photoemission, are generated with a number consistent with the passing beam slice. Then the electric field acting on each MP is evaluated: the field of the beam is precomputed on a suitable rectangular grid (using analytic expressions for special chamber and beam shapes or an Finite Difference Poisson solver for more general cases) and obtained at each MP location by a linear interpolation. The electron space charge contribution is calculated using a Particle In Cell (PIC) algorithm based on a Finite Difference solution of the Poisson equation. Curved chamber boundaries can be accurately simulated since the Shortley-Weller method is implemented in the code [200] and a significant speed-up is obtained by pre-computing the LU factorization of the inherent matrix and reusing it at the different time steps. Once the total electric field at each MP location is known, MP positions and momenta are updated by integrating the equation of motion. At this stage the presence of an externally applied magnetic field can also be taken into account. To obtain sufficient accuracy also for long-lived electrons, e.g. those trapped in the quadrupole fields [201], the Boris tracking algorithm is used [202]. At each time step, a certain number of MPs can hit the wall. In these cases a proper model of the secondary emission process is applied to generate charge, energy and angle of the emitted electrons. One of the peculiarities of the EC buildup process is the fact that, due to the exponential rise driven by multipacting, the number of electrons can spread several orders of magnitude along the passage of the bunch train (see Fig. 30 (top)).

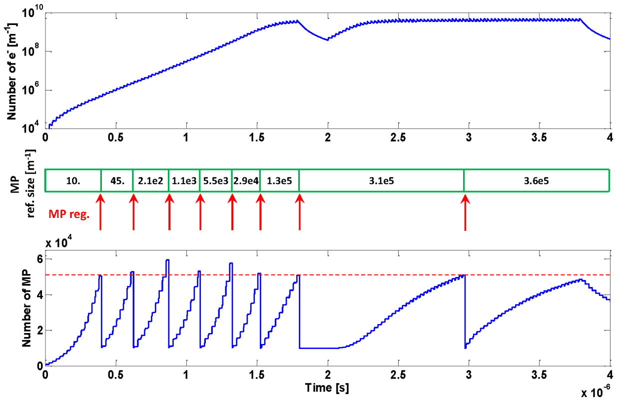

Fig. 30. Top: evolution of the number of electrons in the beam pipe for an LHC type beam with 25 ns bunch spacing in the SPS (2 trains of 72 bunches. MBB type magnet); middle: evolution of the reference MP size; bottom: evolution of the number of MPs, the regeneration threshold is highlighted in red.

As a consequence, it is impossible to choose a MP size, which is suitable for the entire simulation, allowing both a satisfactory description of the phenomena and a computationally affordable number of MPs at every stage of the simulation. The MP size management in PyECLOUD has been modified from the ECLOUD concept and will be briefly described in the following. MP sizes are not enforced throughout the simulation process but are determined step by step by "decisions" taken during the execution. For this purpose a target MP size n_{ref}, dynamically adapted during the simulation, is employed to control the number of electrons per MP. In particular:

- The size of MPs generated by seed mechanisms is exactly n_{ref};
- When a MP hits the wall, it is simply rescaled according to the Secondary Electron Yield (SEY) if the emitted charge is below 1.5 n_{ref}, otherwise "true" secondary MPs are generated so that the resulting MP size is as close as possible to n_{ref};
- Once per bunch passage, a cleaning procedure is performed, which deletes the MPs with charge lower than 10^{-4} n_{ref}.

The target MP size n_{ref} is changed whenever the total number of MPs becomes larger than a certain threshold defined by the user (typical value ~ 10^5), which means that the computational burden has become too high. When this happens, a regeneration of the set of MPs is applied, by performing the following procedure (see Fig. 30):

- Each MP is assigned to a cell of a uniform grid in the 5-D phase space $(x,y,\upsilon_x,\upsilon_y,\upsilon_z)$ obtaining an approximation of the phase space distribution of the electron gas;
- The new n_{ref} is chosen in order to get a target number of MPs (typically 5-10 times smaller than the regeneration threshold), which still allows for an accurate simulation but with a more reasonable computational effort;
- A new set of MPs, having the new reference size, is generated according to the computed distribution.

The preservation of the entire phase space is very important in EC build-up simulation since the dynamics imparted by passing bunches generates very distinctive velocity distributions at the different time steps and the conservation of few specific lower order moments (e.g. total charge, total energy) might not guarantee a sufficient accuracy.

Several numerical tests have shown that the errors on the total charge and the total energy which are introduced by this procedure, are about 1 % at the first time step after the regeneration and they become even smaller after the first bunch passage following the regeneration.

The passage from ECLOUD to PyECLOUD had a significant impact on the performances both in terms of accuracy and of computational efficiency. Furthermore, the new code has been designed in order to offer an increased usage flexibility, allowing to deal with irregular beam structures e.g. non uniform bunch intensity and/or bunch length along the bunch train, irregular bunch spacings and bunch profiles. Thanks to these new features, PyECLOUD has been already largely applied at CERN for several EC simulation studies for the LHC and its injector chain [203-206]. In particular PyECLOUD simulations have been used to reconstruct the evolution of the SEY of the chambers in the LHC arcs, from the measurement of the heat load deposited on the beam screen of the cryogenic magnets. Simulation studies have also addressed the EC formation in the common vacuum chambers of the LHC. Examples of this kind of application are described in [190], showing the capability of PyECLOUD to deal with beams made of thousands of bunches with irregular spacings. The new code also allows us to estimate the bunch by bunch energy loss due to the interaction of the beam with the EC and to export the electron distribution seen by each bunch. The first feature allowed us to benchmark the results against bunch by bunch stable phase measurements, as shown in Fig. 31, while the second was used, together with HEADTAIL simulations, to analyze the instabilities observed in the LHC with 25 ns bunch spacing [207].

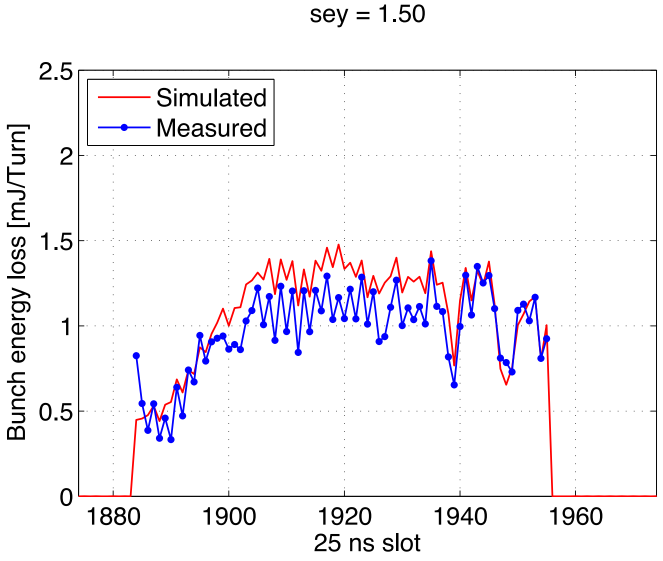

Fig. 31. Simulated and measured energy loss for a train of 72 bunches with 25 ns spacing circulating in the LHC.

D. Effect of Transition Energy on the Transverse Mode-Coupling and Electron Cloud Instabilities: Example of the CERN SPS

The transition energy of a circular accelerator can have a strong impact on the intensity thresholds for coherent beam instabilities, as seen before. The same threshold scaling applies to the single bunch instability driven by e-cloud, in case the wake field generated by the electrons can be approximated by a broad-band resonator. In case a machine is operated not too far from transition, a relatively small change of γ_{tr} can result in a significant increase of the absolute value of the slippage factor and thus to significantly higher thresholds for these instabilities in case the RF voltage is adjusted such that the bucket area and thus the bunch length remain constant. This can be understood intuitively, since the larger absolute value of the slippage factor results in faster synchrotron motion and this is the basic stabilization mechanism for instabilities of the strong head-tail type. The effect of the transition energy on these types of instabilities is illustrated by the example of the CERN SPS in the following. The SPS machine optics used for LHC type beams until 2012 has a gamma at transition of $\gamma_{tr} = 22.8$ and is called Q26 according to the integer part of the betatron tunes $\left(Q_x, Q_y = 26.13, 26.18\right)$. Since the LHC proton beams are injected at 26 GeV/c and thus above transition, reducing the transition energy of the lattice results in a higher slippage factor throughout the acceleration cycle. This is illustrated in Fig. 32, which shows η normalized to the value in the nominal SPS optics as function of γ_{tr} for the case of injection (26 GeV/c) and extraction (450 GeV/c). Note that the largest relative gain can be achieved at injection, which is the most critical part of the cycle with respect to the TMCI in the SPS.

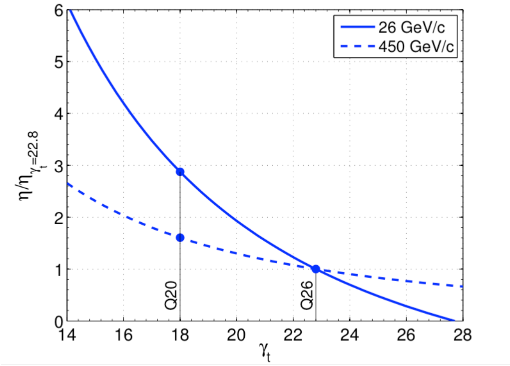

Fig. 32. Slippage factor η relative to the slippage factor of the nominal optics ($\gamma_{tr} = 22.8$) plotted as a function of γ_{tr}. The two curves show the case of injection and extraction momentum.

A new optics configuration with lower transition energy has therefore been developed [208] to overcome the TMCI at SPS injection for reaching the future beam intensity requirements of the LHC. Compared to the Q26 optics, the working point in this so-called Q20 optics is lowered by six integer units $\left(Q_x, Q_y = 20.13, 20.18\right)$ in both planes such that the transition energy is reduced to $\gamma_{tr} = 18$ and at injection energy a 2.85 times larger slippage factor is achieved.

Experimental and simulation studies have been performed in order to compare the intensity threshold for the TMCI in the vertical plane at SPS injection in these two optics configurations in the same experimental conditions. In Q26, the RF voltage of the main 200 MHz RF system was set to 1.4 MV. In order to achieve the same bucket area in the two optics, the voltage was increased to 4.0 MV in Q20. The 800 MHz cavity was operated in bunch shortening mode at 10% the voltage of the main RF system. The vertical single bunch TMCI at injection is one of the main intensity limitations for LHC beams in the Q26 optics. For bunches injected with the nominal longitudinal emittance $\varepsilon_l = 0.35$ eVs, the corresponding instability threshold is around 1.6×10^{11} p/b (with vertical chromaticity adjusted close to zero) [209]. The instability results in emittance blow-up and fast losses as shown in Fig. 32 (top). A significant increase of the ratio of the slippage factor and the vertical beta function at important impedance sources $|\eta|/\beta_y$ is about 2.5 times higher compared to the Q26 optics (the beta functions are slightly higher in Q20). This has been verified in measurements with high intensity single bunch beams as shown in Fig. 32 (bottom), where the instability threshold in the Q20 optics for chromaticity close to zero and the nominal longitudinal emittance of $\varepsilon_l = 0.35$ eVs at injection was found at around 4.5×10^{11} p/b, in good agreement with the analytical estimation (see Eq. (28)).

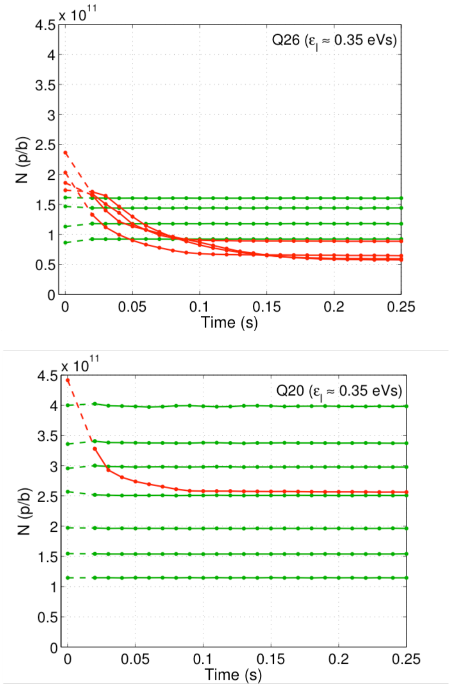

Fig. 32. Intensity as function of time after injection in the Q26 optics (top) and in the Q20 optics (bottom). Red traces indicated unstable beam conditions and green traces correspond to stable conditions.

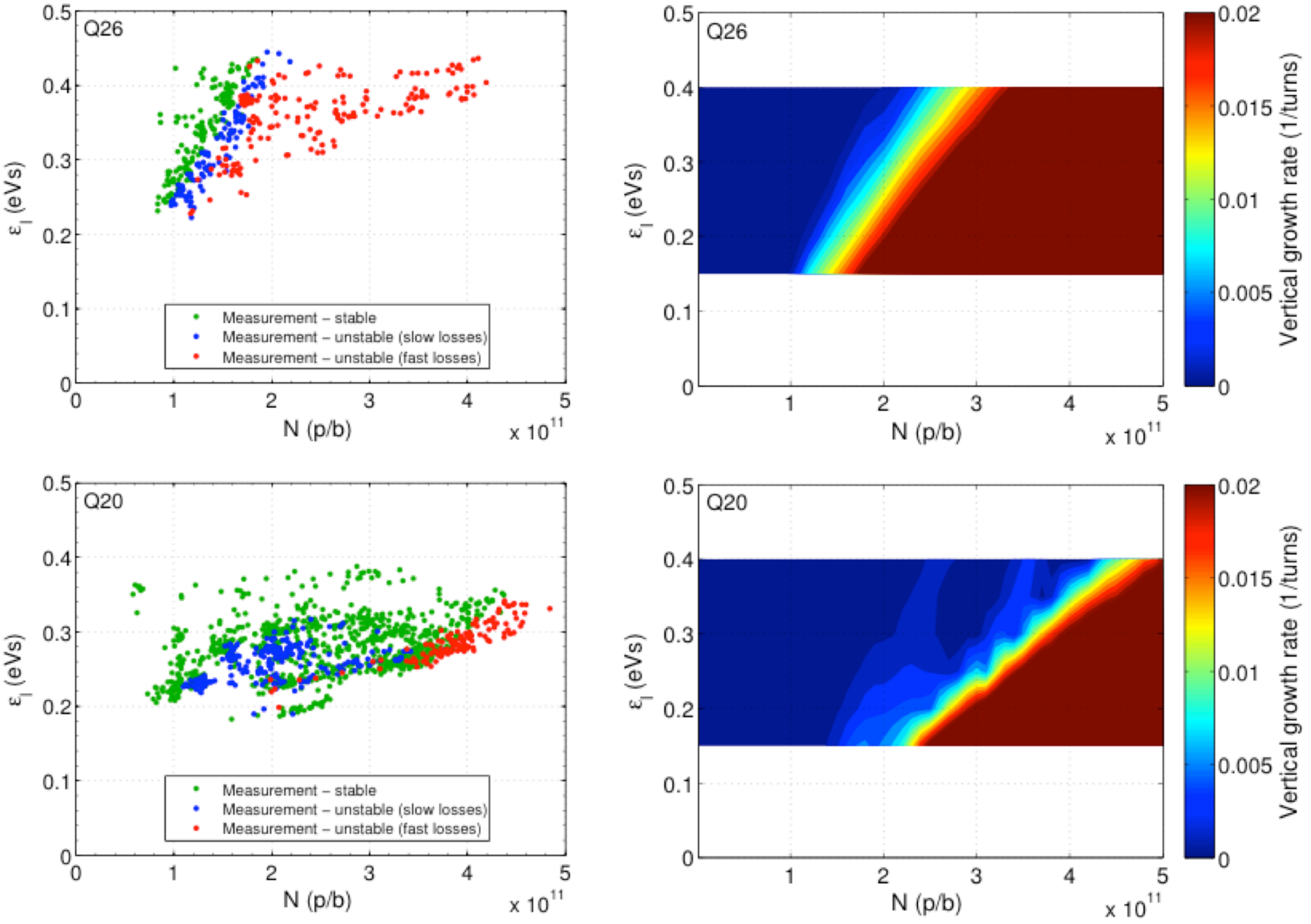

Fig. 33. Measurements of the beam stability at injection with low vertical chromaticity (left) and comparison with the growth rate as predicted by HEADTAIL simulations (right) for the Q26 optics (top) and Q20 optics (bottom).

The TMCI intensity threshold in the Q20 and the Q26 optics was also characterized as a function of the longitudinal emittance and the bunch intensity [208] as shown in Fig. 33 (left). Each measurement point corresponds to the injection of a single bunch into the SPS. Cases in which the beam was stable are indicated by green dots. Injections where the beam was unstable are marked by red dots if losses occurred within the first 1000 turns (“fast losses”) and blue dots if losses occurred later in the cycle (“slow losses”). In the case of the Q26 optics, a linear dependence of the intensity threshold as a function of the longitudinal emittance is observed, as expected from the analytical models. In addition to the strong TMCI at high intensity, an area of “weak instability” is observed in the Q20 optics for longitudinal emittances below $\varepsilon_l \approx 0.32$ eVs and intensities between 1.1×10^{11} p/b and 2.3×10^{11} p/b.

The experimental observations in the two SPS optics are compared with numerical simulations using the wake functions obtained from the SPS impedance model [210], which reproduces almost completely the measured vertical coherent tune shift with intensity. Note that in the beam stability simulations presented here the impedance of the SPS transition pieces between the different types of vacuum chamber geometries is not yet included. However, simulation results indicate that they play a minor role for the TMCI instability thresholds. Figure 33 (right) shows the vertical growth rate as a function of longitudinal emittance and intensity for the two SPS optics as obtained with the macroparticle code HEADTAIL. Both the 200 and the 800 MHz RF systems and the non-linear chromaticity up to third order measured in a separate experiment [208] are taken into account. The threshold intensities are very similar to those observed in the measurements. Furthermore, the area of slow instability experimentally found in the Q20 optics is reproduced in the simulations. Figure 54 shows the measured intra bunch motion for a few example cases in comparison with the results of the HEADTAIL simulations. A clear traveling wave pattern without nodes is observed in the measurement for high intensity in the Q26 optics, which is a typical signature of a TMCI. A very similar intra bunch motion is also observed in the simulation for comparable beam parameters (see Fig. 34). Two cases are shown for the Q20 optics: for high beam intensity, where the strong instability appears, a traveling wave pattern is observed. For an intermediate intensity at which the weak instability occurs, the intra bunch motion has one node in the center of the bunch.

The TMCI observations in the two SPS optics for different ranges of intensities and longitudinal emittances can be reproduced in excellent agreement by numerical simulations when using the detailed SPS impedance model. The scaling of the intensity threshold for the fast TMCI at injection between the Q26 and the low gamma transition Q20 optics is similar to analytical models based on a broadband resonator impedance. With the Q20 optics the TMCI is not of concern for the beam parameters envisaged for the upgrades.

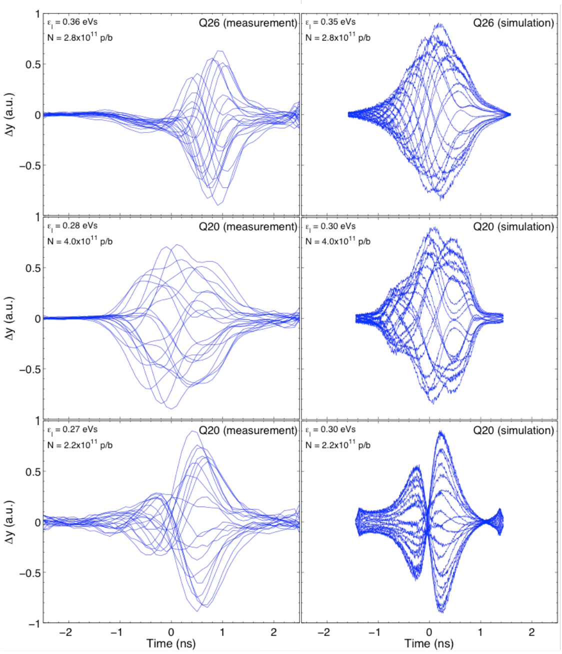

Fig. 34. Vertical intra bunch motion in the SPS Head-Tail monitor measurement (left) in comparison with the corresponding HEADTAIL simulations (right) for one case of the Q26 and two cases of the Q20 optics.

In addition to the TMCI at injection, the electron cloud effect can be a serious performance limitation for the 25 ns LHC proton beams in the SPS, as discussed above. The threshold of the single bunch electron cloud driven instability (ECI) in the SPS has been studied in numerical simulations using HEADTAIL.

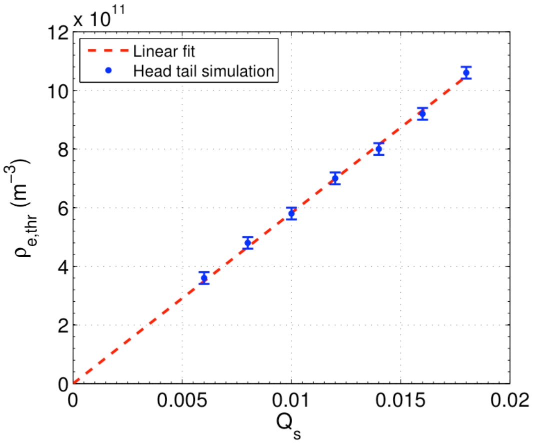

Fig. 35. HEADTAIL simulations yielding the instability threshold density as function of the synchrotron tune for constant bunch parameters. Simulated points are compared with the predicted linear dependence.

It is not attempted to provide an exact prediction for the ECI thresholds in the two optics, in particular since the studies presented here are based on simplified assumptions, such as for example a uniform initial electron distribution. It is rather intended to obtain a relative scaling of the ECI threshold between the Q26 and the Q20 optics in particular at injection energy, at which electron cloud effects in the SPS are usually most critical. First the effect of the transition energy on the instability threshold is studied. Some existing models for the electron cloud single bunch instability predict that the threshold electron density for the ECI onset scales linearly with the synchrotron tune Q_s under the assumption that the bunch length is a given parameter and the RF bucket area is kept constant. Note that in this case the change of the synchrotron tune is proportional to the change of the slippage factor. Figure 35 shows the threshold electron density as function of the synchrotron tune as obtained in HEADTAIL simulations assuming the presence of a dipole magnetic field for beam and machine parameters at SPS injection [208] and zero chromaticity. The expected linear scaling is found. The dependence of the threshold electron cloud density on the optics functions is more complicated compared to the TMCI caused by an impedance source. In particular the electron oscillation frequency around the bunch center due to the attractive electric field generated by the protons is a function of the beam size and thus the wake field generated by the electron cloud depends on the optics functions. Therefore the corresponding average beta functions in the long straight sections and in the bending magnets of the SPS are used for comparing the instability thresholds between the two SPS optics configurations in dipoles and in field free regions, respectively. The resulting threshold electron densities are shown in Fig. 36 for the intensity range of interest for the future upgrades. In both field free regions and dipole regions the electron density threshold in the low gamma transition Q20 optics is about two times higher compared to the Q26 optics. The difference between the two optics seems to be more significant at lower bunch intensities. In field free regions, the electrons can move freely in both transverse directions and thus the proton bunch can become unstable in both planes. However, the beam stability is observed to be more critical in the vertical plane.

In summary, a clear effect of the transition energy on beam stability was demonstrated (as predicted) on the example of the CERN SPS for the TMCI and the ECI. Due to the fact that LHC beams are always injected above transition in the SPS, the slippage factor and thus the instability thresholds are raised throughout the acceleration cycle by lowering the transition energy. In particular, the thresholds for the TMCI and the ECI are about 2.5 and 2 times higher compared to the normal SPS optics used in the past. Since the change of the SPS optics did not require any hardware modification, a very cost effective solution to overcome important performance limitations for LHC beams in the SPS has been found. The example of the SPS demonstrates the importance of the interplay between the machine optics and collective effects and the potential for performance optimization by optics manipulations.

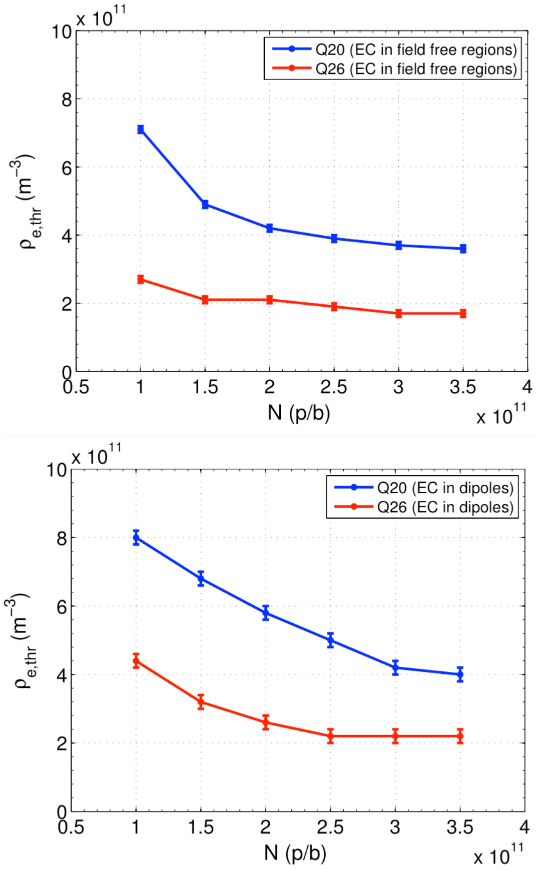

Fig. 36. : HEADTAIL simulations yielding the instability threshold density as a function of intensity per bunch comparing the Q26 with the Q20 optics for field free regions (top) and for the electron cloud located in dipole magnets (bottom), assuming the corresponding average beta functions in the respective locations.

IV. The Example Of The CERN Impedance Models: Comparison Between Theory, Simulations And Beam-Based Measurements

Impedance models have been developed in the past for most of the accelerators in the world, with more or less efforts and with more or less success. Some observables from beam-based measurements often revealed a factor 2 in the best cases, which was most of the time sufficient. For a decade a lot of efforts have been devoted at CERN (in the framework of upgrade projects) to develop more precise impedance models for the different machines such as the PSB, PS, SPS and LHC. The example of the SPS (longitudinal and transverse) and LHC (longitudinal) impedance models are discussed below.

A. CERN SPS Transverse Impedance

The latest SPS transverse impedance model includes kicker magnets, wall impedance, transition pieces (e.g. flanges and vacuum chamber discontinuities), beam position monitors and RF cavities. Analytical models, 3D simulations and bench measurements are used to estimate these contributions. The SPS impedance model is dynamical because it needs to be updated to include newly identified impedance sources as well as modifications of installed elements or new elements. The model has been successfully benchmarked against experimental observations (coherent tune shift, transverse mode coupling and headtail instability measurements). The present version of the SPS transverse impedance model, which we present here, includes the following contributions:

- Kicker magnets. They are likely to be the most important impedance source in the SPS. In a very simple approximation a SPS ferrite loaded kicker can be modelled as two parallel plates of ferrite. For this simple geometrical model all the impedance terms (longitudinal, driving and detuning horizontal and vertical impedances) have been calculated analytically. CST 3D simulations were found to be in very good agreement with the analytical results. The excellent agreement between analytical model and numerical simulations can be read as an important benchmark for the simulation code in the correct solution of electromagnetic problems involving dispersive materials such a ferrite. In the framework of an improvement of the kicker impedance model we performed a step by step simulation study starting from the simplest model and introducing one by one the new features that make the model gradually closer to reality. This approach allows for a good understanding of the different contributions brought to the kicker impedance by the different aspects. First, the ferrite is assumed to be C-shaped and the whole finite length device is inserted in the vacuum tank and equipped with an inner conductor [211]. In order to further approach a more realistic model other aspects have to be included: the cell longitudinal structure, also called segmentation, which determines a significant increase of the beam coupling impedance for the SPS injection kickers (due to the short cell length) and the serigraphy for the SPS extraction kickers. All the details about the SPS kicker impedance model can be found in [210].
- Wall (resistive wall and indirect space charge), based on analytical calculation taking into account the different SPS vacuum chambers [210];
- Beam position monitors, based on CST 3D simulations [100];
- RF cavities, based on CST 3D simulations [212];

- Broadband impedance from step transitions, based on the information for the SPS flanges collected during the task force for the identification of the longitudinal impedance source responsible of the impedance peak at 1.4 GHz observed during beam measurements [102]. The broadband impedance contribution of each type of transition has been obtained by means of CST 3D simulations.

Figure 37 shows the full SPS impedance model including all the impedance sources analyzed weighted by the respective length and beta functions for the horizontal and vertical driving and detuning impedances [210].

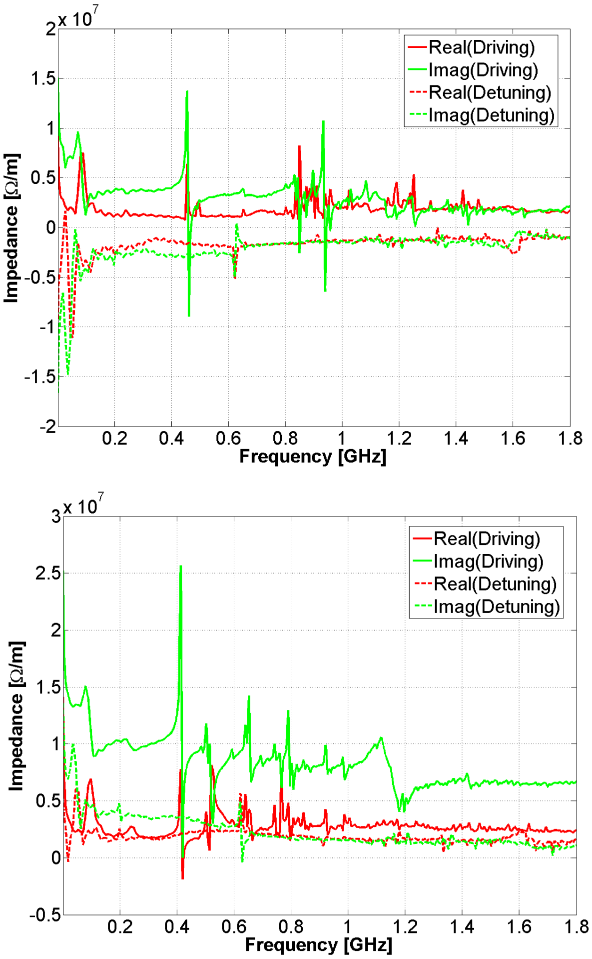

Fig. 37. Horizontal (top) and vertical (bottom) SPS impedance model.

The model has been found to reproduce with very good accuracy coherent tune shift measurements (which give an integrated information about the effective impedance of a machine, which depends on both its full impedance and the length/shape of the bunch used for the measurements, see later) in both transverse planes [213] (see Fig. 38). Moreover, macroparticle HEADTAIL simulations have been found in very good agreement with TMCI and headtail instability measurements [213,214]. We present here (see Fig. 39) the benchmark with the headtail instability measurements (the benchmark with TMCI measurements was discussed before).

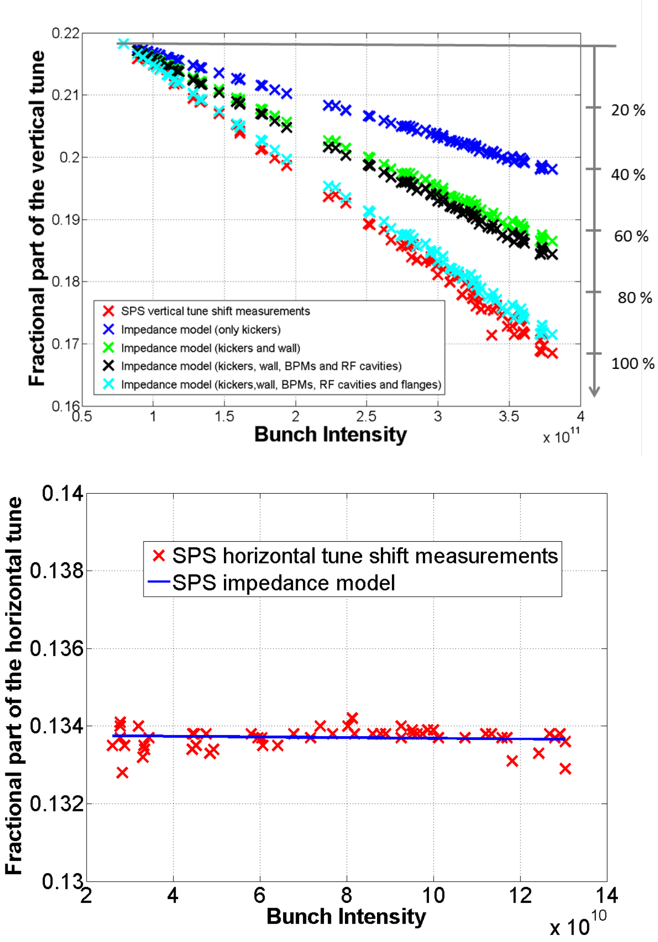

Fig. 38. (Top) vertical tune versus bunch intensity. Measurements performed in September 2012. (Bottom) horizontal tune versus bunch intensity. Measurements performed in March 2013.

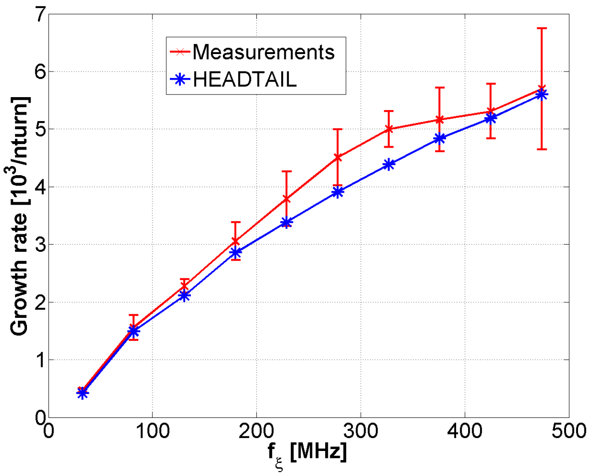

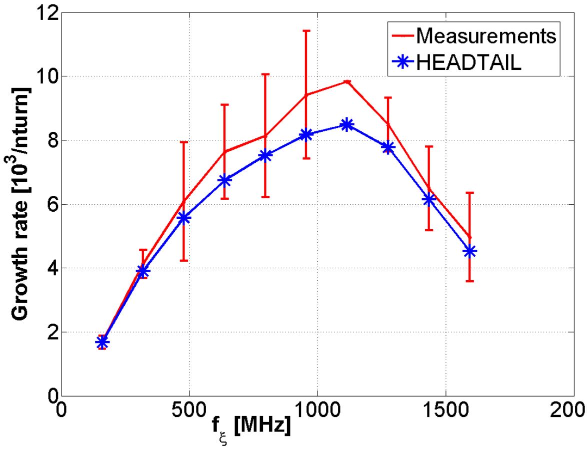

Fig. 39. Comparison between measurements and simulations of the headtail vertical growth rates vs. the chromatic frequency, for both Q20 (top) and Q26 (bottom) optics.

In conclusion, the HEADTAIL simulations using the present version of the CERN-SPS transverse impedance model have been found to reproduce the headtail vertical instability measurements (growth rates and intra-bunch motion). This result, together with the successful benchmark for the coherent tune shift and for the TMCI instability behavior make the SPS a fine example of a machine, whose impedance model can reproduce experimental results with an unprecedented degree of accuracy for particle accelerators. Such an accurate impedance model can be used to drive machine impedance optimization and to estimate the impact on the beam stability of accelerator elements before installation in the machine. The models must be kept up to date according to modifications. Measurements of the tune shifts versus chromaticity are foreseen to further benchmark the impedance model.

B. CERN SPS Longitudinal Impedance

The present longitudinal impedance model of the SPS is a result of intensive impedance calculations and measurements, often driven by beam studies. Indeed, even after the successful impedance reduction in 2000, which eliminated the microwave instability caused by ~ 800 inter-magnet pumping ports, longitudinal instability in the SPS is still one of the main intensity limitations for future high intensity beams [215]. It is observed during acceleration for both single- and multi-bunch beams at intensities well below the nominal LHC intensity. The production of the higher intensity beams required by the HL-LHC project cannot be guaranteed without eliminating the source of this instability [216]. Possible sources are the fundamental and high order modes of the main (200~MHz) and high harmonic (800~MHz) RF systems as well as the impedance of the vacuum flanges. The latter contribution, discovered only recently, consists of many high frequency resonances in the range (1.2-2.5) GHz [217] with the highest peak at 1.4 GHz, seen first in the measurements with long bunches and RF off [218]. The example of the unstable bunch spectra obtained from measurements and simulations using the present SPS impedance model is shown in Fig. 40. The growth rate of the instability at frequency close to the resonant frequency depends on R_{sh}/Q of the impedance and peak positions in the spectrum give valuable information about important sources of the impedance in the ring.

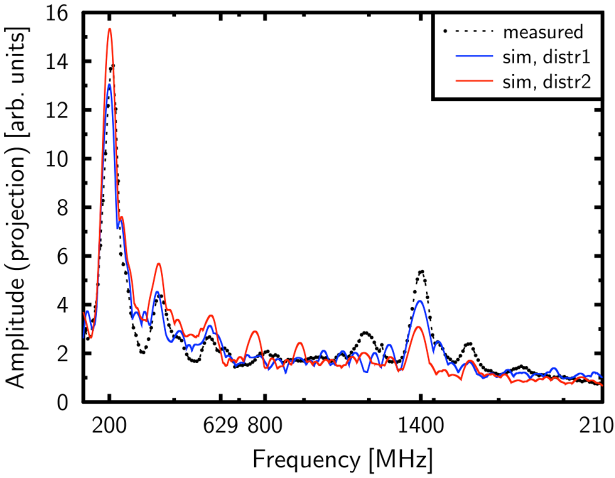

Fig. 40. Projection of spectrum evolution of unstable long bunches on the SPS flat bottom with RF off in measurements (black dashed line) and simulations with two different particle distributions using the present SPS impedance model. Bunches had an average length of 25 ns and an intensity of 1.0 10^{11} p/b.

The measured and simulated single bunch instability thresholds are visible from bunch length measurements on the SPS flat top presented in Fig. 41. One can see that the simulations [219] performed using the present SPS impedance model are in good agreement with two sets of measurements done in 2012 and 2014. An inverted dependence of instability threshold on bunch emittance for these particular beam parameters is due to effect of the potential well distortion in a double RF system (200 MHz and 800 MHz).

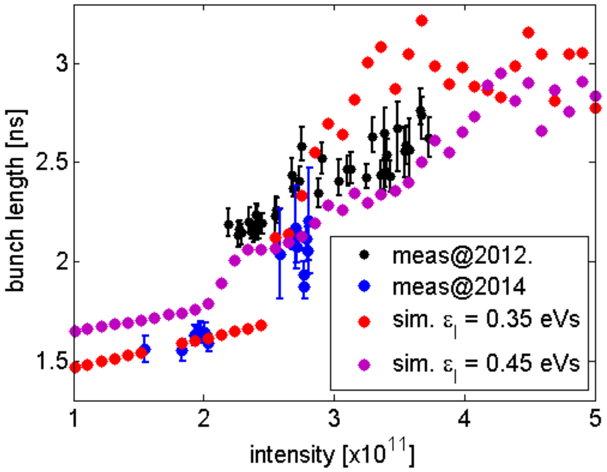

Fig. 42. Measured and simulated bunch length as a function of intensity on the SPS flat top (450 GeV/c) for two values of the longitudinal emittance. At 450 GeV/c the RF voltage at 200 MHz was 2 MV and 0.2 MV at 800 MHz.

The measured multi-bunch instability threshold is different for 25 ns and 50 ns spaced bunches but it doesn't depend on the number of batches in the ring (with 225 ns batch gaps). This points out to the short-range wake which is compatible with the main impedances of the 200 MHz and 800 MHz RF systems which have, correspondingly, quality factor Q of 150 and 300, as well as with vacuum flange impedance at 1.4 GHz with $Q \sim 200$. As expected from scaling of coupled-bunch instability threshold [220], it clearly depends on energy and longitudinal emittance: more dense bunches become unstable earlier in the cycle. In present operation the LHC beams are stabilized by increased synchrotron frequency spread (Landau damping) using the fourth harmonic RF system in bunch-shortening mode and controlled longitudinal emittance blow-up performed by band-limited noise. The emittance blow-up in a double RF system has its own limitations due to modification of the synchrotron frequency distribution by presence of beam loading [221]. The thresholds were also increased in the new SPS optics (Q20) with lower transition energy (γ_t = 18 instead of the previous γ_t = 22.8 with the Q26 optics) [208]. For a low transition energy the expected increase in longitudinal instability threshold is proportional to the slip factor [222]. However for the same longitudinal parameters the required voltage also scales as the absolute value of the slip factor. Already the maximum 200 MHz voltage is used for beam transfer to LHC, but the controlled emittance blow-up could also be reduced for the same intensity. This scaling was tested by measurements performed in different beam studies [208]. Significant improvement in beam stability (around factor 3) was obtained on the flat bottom. However on the flat top the high harmonic RF system is still insufficient for stability of high intensity beams and one needs in addition the controlled emittance blow-up.

Single short bunches injected into mismatched RF voltage continue to oscillate on the SPS flat bottom for many seconds. The reactive impedance, responsible for this loss of Landau damping, was probed at the 26 GeV/c flat bottom by measuring the synchrotron frequency shift as a function of intensity for different bunch lengths. The comparison of measured and simulated synchrotron frequency slopes are shown in Fig. 43. At this beam energy the space charge contribution should also be included into the SPS impedance model used in simulations. The calculations done for realistic transverse emittances taking into account bunch and vacuum chamber size variation over the ring give 1.1 Ω for the Q20 optics (1.2 Ω for the previous, Q26 optics). One can see that for certain bunch lengths the shifts are close to zero. This is a result of a complicated dependence of the SPS reactive impedance on frequency and in particular of the presence of the high frequency impedance from vacuum flanges. The new SPS impedance reduction programme, which will include shielding or redesign of the vacuum flanges in under discussion in the frame of the CERN LIU project [215].

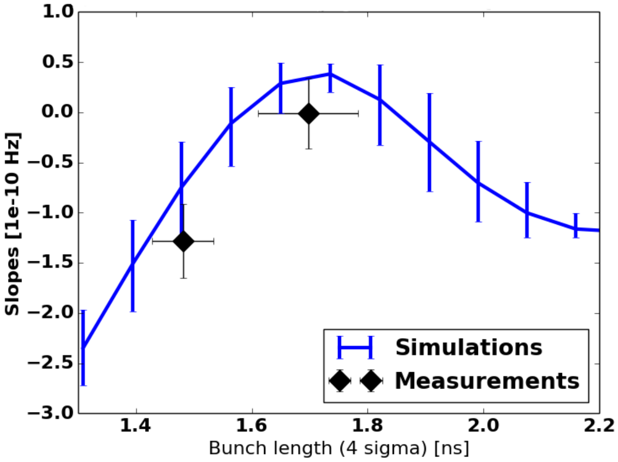

Fig. 43. Slope b of quadrupole synchrotron frequency shift with intensity $f_2 = a + b\,N$ found from measurements and simulations for different bunch lengths in the Q20 optics at 26 GeV/c.

C. *CERN LHC Longitudinal Impedance*

During the design phase of the LHC, significant efforts were made to reduce its impedance in order to minimize the impact of collective effects on the accelerator performance. According to the LHC Design Report [223] and the current LHC impedance model [105], the reactive part of the LHC effective longitudinal impedance ImZ / n is 0.08 Ω. This value is very small compared to other CERN proton accelerators, e.g. 4 Ω in the SPS and 20 Ω in the PS. Therefore, beam measurements of the LHC impedance with usual methods are very challenging. This impedance is however sufficient to cause loss of Landau damping during acceleration leading to single-bunch instability in the LHC [224]. Therefore, controlled longitudinal emittance blow-up is required in operation. So far, observation of loss of Landau damping was found to be the most sensitive method for validation of the LHC impedance model. During one measurement session in 2012, 4 bunches of similar intensity (~ 2.4 10^{11} p/b) and different longitudinal emittances were accelerated to 4 TeV with phase loop off. The energy E_{th} at which bunches became unstable is shown in Fig. 44, and the dependence on the longitudinal emittance is in accordance with the expected scaling $E_{th} \propto \varepsilon_l^2$ [225-227]. These measurements show that the nature of the instability observed is compatible with loss of Landau damping. From measurements made during another session in 2012 at 4 TeV and with an RF voltage of 12 MV, the threshold of loss of Landau damping was found to be around 1 eVs for a bunch intensity of 1.0 10^{11} p/b [228]. With the aim of reproducing the measurements at 4 TeV, simulations using the LHC impedance model were performed with the code BLonD [168]. The generated particle distribution was similar to the measured one and matched with intensity effects. Then a phase kick of 1° was applied to the bunch and the bunch phase oscillations were observed. Figure 45 shows the intensity threshold for different longitudinal emittances found in simulations and in measurements. Unfortunately only one point is available from measurements up to now, for which the agreement is very good. The dependence of the threshold on the longitudinal emittance is in accordance with the expected scaling $N_{th} \propto \varepsilon_l^{5/2}$ [225-227].

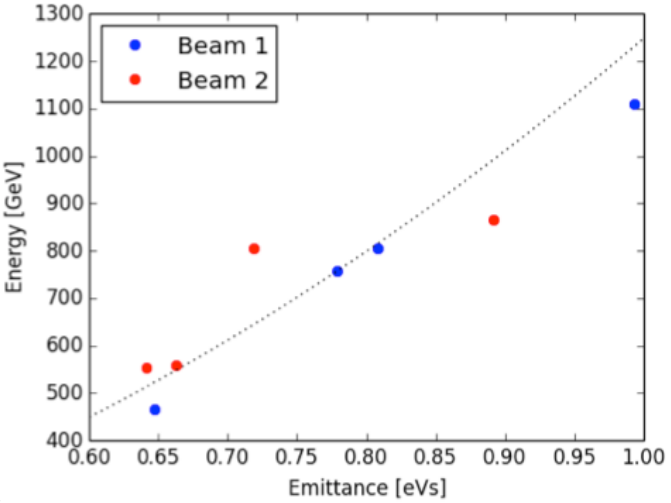

Fig. 44. Measured energy threshold E_{th} of loss of Landau damping as a function of longitudinal emittance ε_l with phase loop off. The dashed line is the fit of the measurements according to $E_{th} \propto \varepsilon_l$.

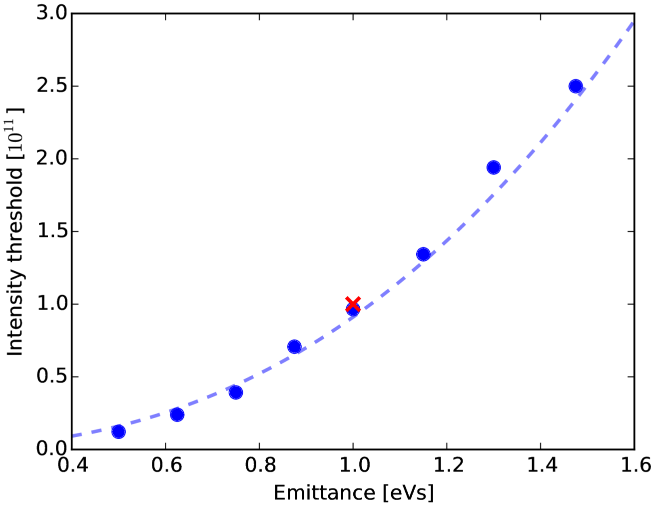

Fig. 15. Intensity threshold of loss of Landau damping from simulations (blue circles) together with the expected scaling $N_{th} \propto \varepsilon^{5/2}$ (dashed line) and the measured threshold (red cross).

The reactive impedance ImZ / n can also be estimated from the measured incoherent synchrotron frequency shift Δf_s with intensity. The expected frequency shift can be calculated for a Gaussian bunch with intensity N and 4σ length τ using the following expression (e.g. [135])

$$\Delta f_s = -f_s \left(\frac{2}{\pi}\right)^{\frac{1}{2}} \frac{16\, N\, e\, \omega_0\, h^2}{V\, (2\, \pi\, h\, f_0\, \tau)^3} \frac{ImZ}{n}, \tag{30}$$

where h is the harmonic number and V is the RF voltage. Two different methods were used to measure Δf_s. In the first one, the synchrotron frequency was obtained from the quadrupole line of the peak-detected Schottky spectrum [229]. Measurements done with bunches of the same length (1.4 ns) and a difference in intensity of 1.0×10^{11} show that the frequency shift is smaller than 0.5 Hz. Although this result is at the limit of the measurement accuracy, it is in agreement with the expected frequency shift found from (1), $|\Delta f_s| = 0.38$ Hz. The incoherent synchrotron frequency shift was also estimated from measurements using an RF phase modulation at 450 GeV [230]. A sine-wave modulation was applied to 8 bunches, which had close longitudinal emittance and different intensities. The modulation frequency was reduced in steps of 0.1 Hz starting from 55.3 Hz, above the linear synchrotron frequency $f_{s0} = 55.09$ Hz for an RF voltage $V = 6$ MV. A bunch with $N = 0.8\times10^{11}$ and $\tau = 1.2$ ns was excited with a frequency 0.1 Hz higher than one with $N = 1.4\times10^{11}$ and $\tau = 1.35$ ns. This measurement is in good agreement with the expected 0.11 Hz shift calculated from Eq. (30).

A first attempt to measure the resistive part of the longitudinal impedance was done using synchronous phase measurements. This method was successfully used to measure the energy loss due to electron-cloud [231], which produces a synchronous phase shift in the order of 1° with 25 ns spaced bunches. The expected phase shift due to the resistive impedance is smaller, in the order of 0.1° for 1 ns long bunches with a difference in bunch intensity of 1.0×10^{11}, which is approximately in the same order as the systematic errors in the measurements. The accuracy of the method is therefore not enough to measure the absolute value of the resistive impedance, but it can be used for relative measurements. For example, it was used to measure the resistive impedance of the LHC beam injection beam stopper (TDI) [232] and results are in agreement with electromagnetic simulations. Some improvements were done during the LHC Long Shutdown 1 (2013-2015) to the synchronous phase measurement system in order to reduce the systematic errors and new attempts to measure the resistive impedance will be done during the LHC Run 2 in 2015.

V. EFFECTS OF OTHER MECHANISMS ON THE IMPEDANCE-INDUCED BEAM INSTABILITIES

A. *Transverse Damper*

1) *NHT Vlasov solver*

So far, solutions of the Vlasov equation were limited by rather simple cases (see e. g. Ref [1]), insufficient to tell about complicated reality of multi-bunch beams with feedbacks and octupoles, and also beam-beam effects in colliders. That is why a second approach to beam stability problems, macroparticle simulations, attracted more and more attention, driven by continuing burst of computational powers. For colliders, such codes as HEADTAIL [150] and BeamBeam3D [233] are known and used for more than ten years. Attractiveness of the macroparticle tracking programs is related to their similarity to real beams; they appear to be as close to reality as possible, allowing rather straightforward introduction of all the factors influencing beam stability. However, an attempt of these direct simulations of reality has its drawback: convergence typically requires a big number of macroparticles per bunch, at the order ~10^6 or so. For thousands bunches per beam in the collider, it makes a required study of multi-dimensional space of parameters so far impossible by means of the macroparticle tracking – even with the help of parallel computations by powerful supercomputers.

This limitation of the tracking methods brings us back to the Vlasov equation with a motivation to develop more sophisticated methods of its solution, where all important factors of reality would be properly taken into account. The Nested Head-Tail (NHT) Vlasov solver suggests an attempt in this direction [234]. Its name points to its primary idea: solutions of the Vlasov equation are sought as expansions over conventional head-tail functions, defined at a set of nested rings in the longitudinal phase space. Since the impedance, feedback, and coherent beam-beam are described by linear response functions, their analysis is reduced to a standard eigensystem problem that is solved instantaneously, as soon as the related matrices are defined. After this is done, growth rates and tune shifts of all potentially dangerous modes are known. However, with any feedback, that pure linear system is still unstable: its stabilization requires some Landau damping, an intrinsic self-stabilization mechanism caused by nonlinearity of single-particle motion. In general, these anharmonicities lead to very complicated equations (see e.g. Eq.(6.179) in Ref. [1]). However, for many practical cases, the anharmonicities may be treated as perturbations of the linear system. When Landau damping moves the coherent tune shifts not by much, it can be found as a perturbation. That is how Landau damping is treated by the NHT, allowing finding thresholds of the instabilities, with both octupoles and beam-beam nonlinearities taken into account. Fortunately, for many practical cases this perturbative approach to Landau damping is justified. For pure transverse nonlinearities it leads to well-known dispersion relations (see Ref. [235] and references therein). Otherwise, more general form of the dispersion relation has to be applied, see a section "Landau Damping" in Ref. [234].

In Ref. [236], the instability growth rate computed from the BeamBeam3D [233] tracking simulations for LHC parameters is presented as a function of the chromaticity and damper gain (the gain here is in unit of synchrotron tune and 1.4 corresponds to a damping time of 50 turns). For those simulations, a single 3D-Gaussian bunch per beam and single IP were assumed. The intensity and collision parameters were taken close to the end of the beta-squeeze case. Namely, 10 rms beam radius of the beam-beam separation was assumed, and the computed beam-beam long-range kick was additionally enhanced by a factor of 10, thus simulating 10 identical long-range collisions instead of one. The IP optics was taken as perfectly round, all the octupoles were zeroed, the potential well was supposed to be ideally parabolic, and the doubled nominal impedance of the LHC [47] was implemented. To make a comparison, NHT computations were fulfilled for the same conditions.

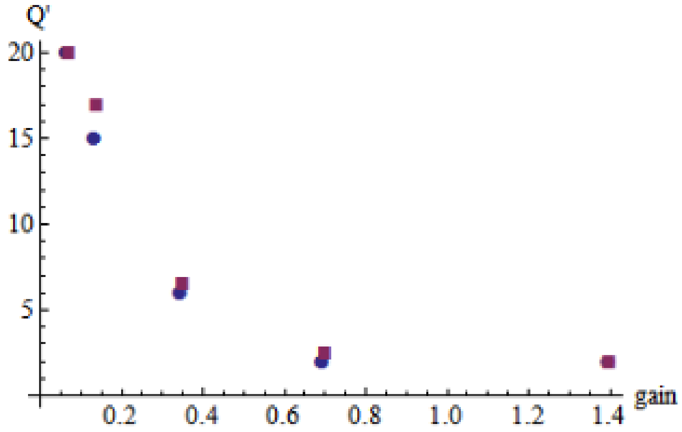

Fig. 46. Threshold chromaticity versus the damper gain for BeamBeam3D tracking (circles) [233] and NHT solutions (squares).

In Fig. 46, these results of BeamBeam3D are presented together with corresponding NHT ones. The NHT results reflect eigenvalue computation with both coherent and incoherent beam-beam on, followed by analysis of the stability diagram. Since implementation of the incoherent beam-beam effects is formally identical to the octupoles, the good agreement between the two principally different codes shows correctness of their linear and octupolar parts.

Figures 47 and 48 show NHT results for the effective octupole current stabilizing one or two LHC beams seeing each other at the end of the betatron squeeze. The effective octupole current is the sum of the Landau octupole current and a contribution of the beam-beam nonlinearity expressed in terms of the equivalent octupole current. According to Ref. [237], the oncoming beam contributes 100 A to the effective octupole current for the pacman bunches and twice more for the central ones at the end of the squeeze. It follows then, that about 100A of the Landau octupoles should be sufficient for the stabilization, assuming the machine is operated at the high gain and high chromaticity plateau of Fig. 48, as it was in the second part of 2012. Contrary to this conclusion, at the end of the squeeze a transverse instability was permanently observed, notwithstanding the octupole current was kept at its maximum of ~ 550A [238].

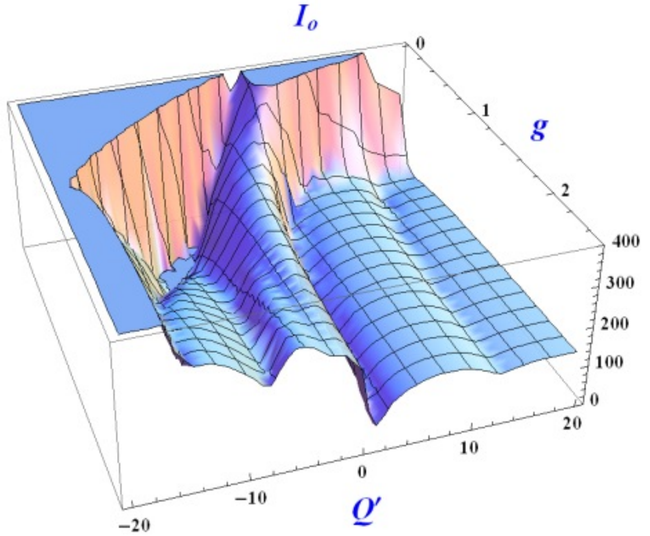

Fig. 47. Threshold octupole current [A] at positive polarity, for a full 50 ns single beam in the LHC and doubled nominal impedance.

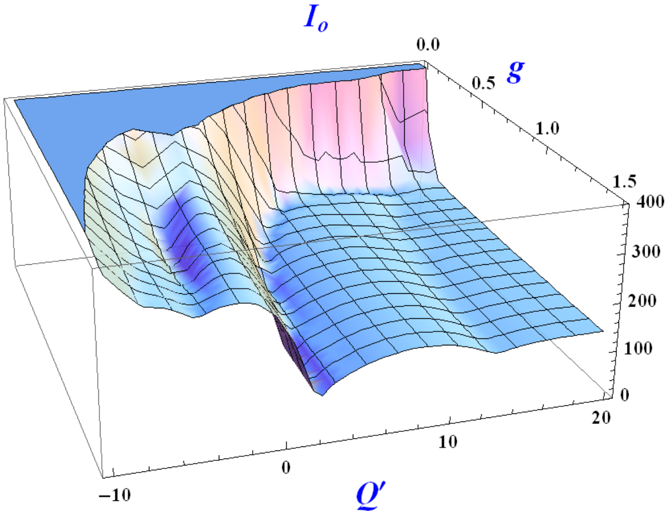

Fig. 48. Same as above, but for two 50 ns single beams at the end of the betatron squeeze.

An initial idea that this instability is driven by the coherent (strong-strong) beam-beam effect or some hidden two-beam impedance was refuted by the NHT computations [239], confirmed later by a dedicated LHC beam experiment [240]. To explain this instability, a hypothesis of three-beam instability, or beam-beam-beam effect was suggested, where the third beam is an electron cloud accumulated in a high-beta area of the main interaction regions [241, see later].

The NHT Vlasov solver has been effectively used as a computation tool for transverse collective oscillations of high-energy beams in the LHC, with their radial modes, couple-bunch modes, feedbacks, beam-beam effects and octupole-related Landau damping accurately handled. The main advantage of that solver against macroparticle tracking codes is many orders of magnitude shorter CPU time, which allows a fast and efficient analysis of that complicated system in a multidimensional space of parameters. In many cases the measurements of beam stability were within a factor ~ 2. The effect of chromaticity and damper gain will be studied in more detail during the LHC Run II (2015-2018).

2) DELPHI

DELPHI (for Discrete Expansion over Laguerre Polynomials and Headtail modes to compute Instabilities), is an analytical code to compute transverse instability modes from beam-coupling impedance and transverse feedback. Its find the eigenmodes of Vlasov equation for a distribution of particles circulating in a synchrotron under the combined action of beam-coupling impedance and a feedback damper, based on an extension of Sacherer integral equation solved on a basis of Laguerre polynomials combined with standard azimuthal headtail modes, and it is systematically checking for convergence vs. the number of modes [242]. Instabilities can be predicted for any machine, with any initial longitudinal distribution, any kind of transverse dipolar impedance and for any reactive or resistive bunch-by-bunch damper. Chromaticity is included in the model, as well as multi-bunch effects. We apply the present theory to several synchrotrons such as VEPP and LEP, and benchmark our code with other approaches, including other instability theories and particle tracking simulations. In particular, a new light is shed on the relative lack of success in trying to stabilize the transverse mode coupling instability using a reactive or resistive transverse feedback in the LEP.

This approach is very similar to the one adopted in the MOSES [149] code, as well as in the model by Karliner and Popov [159]. The main additions here are 1/ the extension to the multibunch case, 2/ the possibility to consider any longitudinal distribution, and 3/ the automatic checking of the convergence vs. matrix size.

As a first example, we show in Figs. 49 and 50 a comparison between the codes MOSES and DELPHI for the case of the old CERN LEP collider (whose tunnel is currently being used for the LHC), without transverse damper. Note that the LEP impedance model is reduced to a single broadband resonator, corresponding to the RF cavities [243,244], as the code MOSES cannot perform calculations on impedance models more elaborated than a single resonator. In Fig. 49 the real part of all the modes are compared at zero chromaticity, while in Fig. 50 the imaginary part of the modes at the chromaticity Q' = 22 are benchmarked. In both cases, the agreement between the two codes is excellent, which is expected since they are based on the same formalism. Note that the number of modes have been fixed in our approach, i.e. the algorithm to check convergence in DELPHI is deactivated, in order to be able to compare with MOSES in which the number of modes has to fixed in input. We benchmarked also DELPHI with some of the results from Karliner and Popov [159], in the case of the VEPP-4 machine (BINP, Novosibirsk). For a non-zero feedback gain and zero chromaticity an excellent agreement was found also in this case. Again, the number of modes included in the computation has been fixed to allow the comparison.

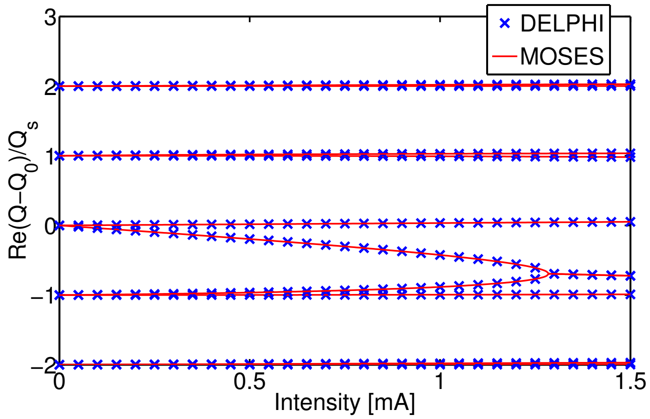

Fig. 49. Comparison between DELPHI and MOSES for LEP in single-bunch at zero chromaticity, for the real part of the tuneshifts of all modes. LEP parameters are: energy 22 GeV, RMS bunch length 1.834 cm, circumference 26.659 km, Q_x = 76.194, Q_s = 0.108, α_p = 1.855 · 10^{-4}, broad- band shunt impedance R = 1.51 MΩ/m with Q = 1 and cut-off frequency 1.4 GHz. 5 azimuthal modes and 2 radial modes were included in the computations.

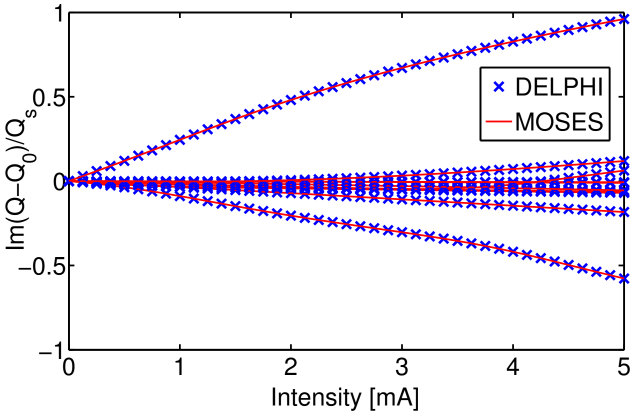

Fig. 50. Comparison between DELPHI and MOSES for LEP in single-bunch at $Q' = 22$, for the imaginary part of the tuneshifts of all modes. LEP parameters are the same as in Fig. 49. Note that instabilities correspond to negative tune shift in our convention.

However, in the case when both chromaticity and damper gain are non-zero, a significant discrepancy was found between the two approaches. Note that in this case, the fully converged result is used in DELPHI, but a similar discrepancy (although somewhat different) would be still visible when the number of modes are set exactly the same as in Karliner and Popov's paper. Note still that the damper model used here is simpler than the sophisticated damper these authors use, which we cannot model here since its parameters are not all provided in Ref. [159]. Nevertheless, in the same plot (see Fig. 51) we also show the results of HEADTAIL macroparticles simulations, which turn out to give a curve very similar to the one obtained from DELPHI for the most unstable mode.

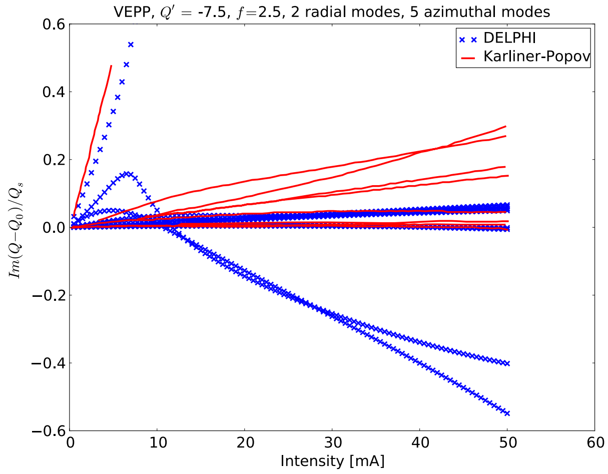

Fig. 51. Comparison between DELPHI and Karliner-Popov results for the imaginary part of the tune shifts of all modes in VEPP-4 in single-bunch at $Q' = -7.5$, with a resistive feedback gain corresponding to f = 2.5 (see details in Ref. [159] – the corresponding damping gain $1 / n_d$ in our theory depends on the intensity and is related to f by $1 / n_d = I f 2\pi Q_s / I_b$ with I the intensity in A and $I_b = 0.0199$ A). VEPP-4 parameters are: energy 1.8 GeV, RMS bunch length 7.5 cm, circumference 357.9 m, $Q_x = 7.62$, $Q_s = 0.025$, $\alpha_p = 0.01645$, broad-band shunt impedance $R = 5.02$ MΩ/m with $Q = 1$ and cutoff frequency 0.506 GHz. 5 azimuthal modes and 2 radial modes were included in the computations. We also show the imaginary tune shift of the most unstable mode from HEADTAIL macroparticles simulations.

Having benchmarked our code in various situations, we now try to use DELPHI to shed a new light on LEP TMCI and the relative lack of success in the various attempts to stabilize it with a transverse bunch-by-bunch feedback [245]. Over the years of operation of LEP, at least two kinds of damper were tested: 1/ a reactive feedback, to prevent the azimuthal mode 0 to shift down and couple with the azimuthal mode – 1, or 2/ a resistive feedback, which was tried at LEP but never used in operation, and recently thought to be a good option by Karliner-Popov [159] with a possible increase of the TMCI threshold by a factor ~ 5 . It is also worth mentioning that there was in general a good agreement between measurements of the TMCI threshold (just below 1 mA) and the LEP impedance model [245]. To try to explain these observations, we show in Figs. 52 and 53 two-dimensional plots where the color represents the TMCI threshold as a function of the chromaticity and feedback gain, for respectively a resistive and a reactive feedback, using the DELPHI code (fully converged). It appears clearly that the resistive feedback does not improve the TMCI threshold, and the reactive one can improve it only marginally (at high feedback gain). This is in qualitative agreement with the observations in LEP.

The code is available as part of a broader software suite that can be used to compute impedances and instabilities in particle accelerators and synchrotrons, called IRIS (for Impedance, Resistive-Wall and Instability codes and Scripts) [246]. In the future, all kinds of longitudinal non-linearities could be included, but with probably some difficulties: (i) non-linear bucket, (ii) quadrupolar wakes and (iii) second order chromaticity.

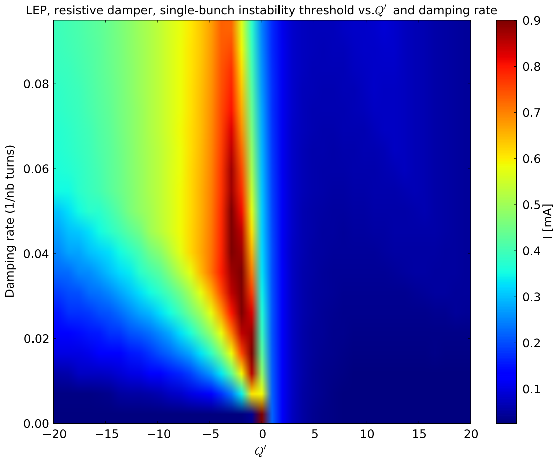

Fig. 52. TMCI threshold (color) vs. chromaticity and damper gain of a transverse resistive feedback. Parameters are the same as in Fig. 49 except for the RMS bunch length (1.3 cm) and the impedance model that is more complete here (two broad-band resonators for the RF cavities and the bellows, of shunt impedances respectively 1.1 and 0.23 MΩ/m, cut-off frequencies 2 and 12 GHz, and of quality factor $Q = 1$).

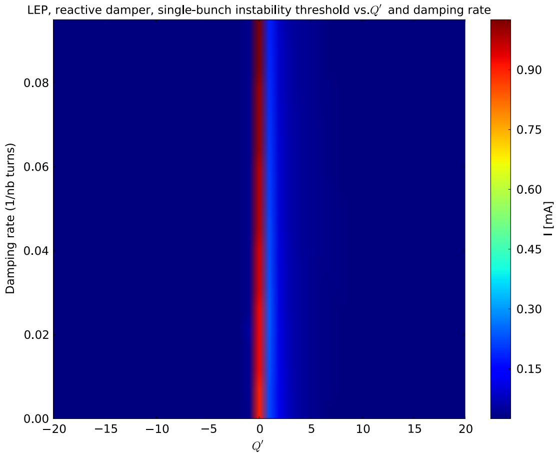

Fig. 53. TMCI threshold (color) vs. chromaticity and damper gain of a transverse reactive feedback. Parameters are the same as in Fig. 52.

B. Space Charge

1) Theory

The head-tail instability of bunched beams was observed and theoretically described many years ago, as discussed before. Since then, this explanation has been accepted and included in textbooks, but still there is an important gap in the theory of head-tail interaction. This relates to the influence of space charge on the coherent modes: their shapes, growth rates, and Landau damping. Two theoretical articles of M. Blaskiewicz [247,248] shed certain light on this issue. In particular, a compact analytical description of the coherent modes was found there for a square well model with a short-range wake function, without any assumption for the relative values of the space charge tune shift, the synchrotron tune, and the coherent tune shift.

Compared to these papers, an attempt of Ref. [249] is both broader and narrower. It is broader since there are no assumptions about the shape of the potential well, the bunch distribution function, single- and coupled-bunch dipole and quadrupole wake functions and feedbacks. The solution for a parabolic potential well and 3D Gaussian bunch had been given there in detail, but the method is universal. It was shown that contrary to the coasting beams, there is the *intrinsic Landau damping*, i.e. Landau damping driven by the space charge itself. Both intrinsic and octupole-related damping rates were estimated up to a numerical factor ~1.

From another aspect, the approach of Ref. [249] is narrower than that of Ref. [247, 248], since in the former the *strong space charge approximation* was applied, i.e. the space charge tune shift was assumed to be large compared to the synchrotron tune and the wake-driven coherent tune shifts.

The reason why this case allows to be effectively treated is that all the particles at the given longitudinal position respond almost identically to the collective field when the space charge is strong, since spread of the incoherent frequencies is much smaller than the separation between the coherent and incoherent peaks. Thus, as soon as the space charge is strong, the bunch slices oscillate as rigid discs; the strong space charge approximation can be called the *rigid slice approximation* as well. This fact entails the fact that the bunch eigenfunctions to depend on a single longitudinal phase space argument, namely, the position along the bunch, contrary to the no space charge case, when the eigenfunctions depend on two arguments, the synchrotron action and phase. Thus, rather unexpectedly, space charge leads to the significant simplification, when it is strong.

Using the rigid slice approximation, the problem for the coherent modes in the presence of strong space charge and arbitrary wakes has been reduced in Ref. [249] to a single-dimension second-order linear integro-differential equation with zero boundary conditions for the eigenfunction derivative; this has been done for arbitrary beam distribution functions and potential well. The detailed formulas can be found in Ref. [249] or, with more details, in [250].

It has been also shown how this problem is effectively solved in two-step approach. At the first step, no-wakes problem (zero right-hand side of the Burov equation) has to be treated. This is a standard Sturm-Liouville problem which solution is given by a one-dimensional array of orthogonal eigen-functions. For the Gaussian distribution, the spectrum of this equation has been described in Refs. [249-251]; similarly, it can be found for any potential well and distribution function. After the no–wake problem is solved, its eigenfunctions can be used as an ortho-normalized basis for the Burov equation with given wakes and dampers. Expansion of the eigenfunction over the no-wake set the amplitudes to be found, leads to the algebraic problem for the eigenvector of the amplitudes. This equation allows computing the instability growth rates for fairly general situations when the Landau damping can be neglected. However, without Landau damping nothing can be said about the instability threshold, so the theory would be incomplete. For the strong space charge, Landau damping rates were roughly estimated in Ref. [249]. Numerical simulations give a possibility for more accurate knowledge of the damping rates, with the numerical factors to be found with a good precision. This work was started by V. Kornilov and O. Boine-Frankenheim several years ago with their PATRIC code [252,253], and has been joined recently by A. Macridin et al. with the Synergia program [254, 255]. When the collective tune shifts imposed by the wakes are small compared to the synchrotron tune, their influence on the Landau damping can be neglected. Potential importance of the image charges and currents for Landau damping was shown in Ref. [252, 253]. A preliminary version of the Vlasov solver built in these principles was presented in Refs. [256,257]. Hopefully, this work will be generally completed in a reasonable future. However, outside the strong space charge approximation, the problem of the transverse collective motion of the bunched beams with space charge does not have any other solution except the macro-particle tracking so far.

2) Simulations

The eigenspectrum of transverse head-tail oscillations for a bunch in an rf bucket with the synchrotron tune Q_s is given by $Q_k = k\ Q_s$ ($k \in Z$). These can be observed in the Schottky noise as equidistant satellites at each betatron side band, $f = f_0\,(1 \pm Q^f)$ where Q^f is the fractional part of the bare betatron tune. The composition of the betatron side band with different amplitudes provides the power frequency spectrum for a given head-tail mode and depends on the bunch distribution.

In order to characterize the space charge force in a bunch, we use the space charge parameter

$$q = \frac{\Delta Q_{SC}^{KV}}{Q_s}, \tag{30}$$

which is the direct space charge tune shift for the rms-equivalent K-V beam (the geometric factor, which depends on the transverse distribution, is 2 for the Gaussian profile and 1 for a K-V beam) in the peak of the line density normalised by the synchrotron tune.

A very useful model for the head-tail instability with arbitrary space charge has been suggested in [247], as discussed before. This "airbag" model assumes two opposing flows of particles in the longitudinal plane, and a square-well potential and thus a constant line density. Rigid flows are considered, i.e. only dipole oscillations without variation in the transverse distribution of the flows are included. The resulting tune shift due to space charge is given by

$$\frac{\Delta Q}{Q_s} = -\frac{q}{2} \pm \sqrt{\frac{q^2}{4} + k^2}\ , \tag{31}$$

where "+" is for modes $k > 0$. These space charge tune shifts are illustrated in Fig. 54.

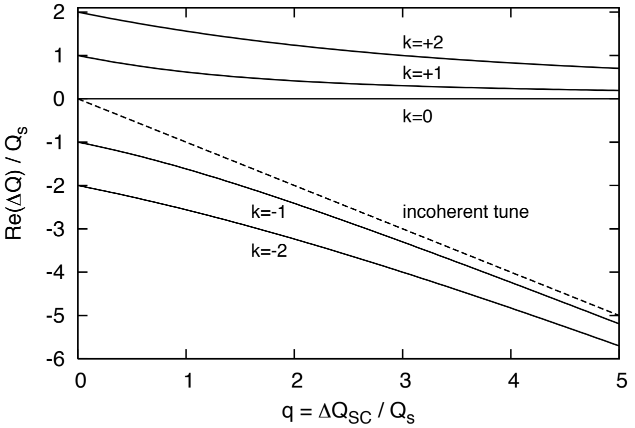

Fig. 54. Tune shifts of five head-tail modes versus space charge parameter q as given by the airbag theory (see Eq. (30)), the dashed line is the incoherent betatron tune (Q_0 - ΔQ_{sc}).

The validity of this model has been perfectly confirmed by particle tracking simulations [258], which suggests to use the model also for accurate numerical code validation. In the recent works discussed before [249-251] analytical treatments of head-tail modes with space charge for realistic bunch distributions (e.g. Gaussian) have been proposed. It appeared that the airbag model is still surprisingly good for predicting the bunch eigenfrequencies, especially for strong space charge. Figure 55 shows the coherent oscillation spectra for a bunch with q = 20 from particle tracking simulations [252,259], in a comparison with the airbag theory. Note that without space charge the modes are located at $k\ Q_s$, so the prediction error is below ~ 5 %.

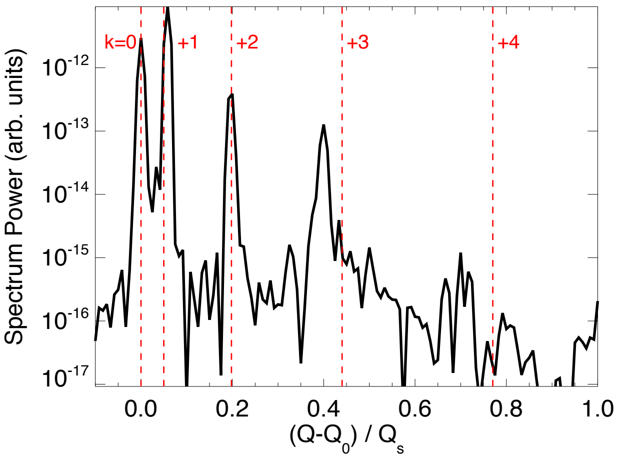

Fig. 55. Transverse bunch spectrum from simulations [252] for a Gaussian bunch with space charge. Red dashed lines are given by Eq. (31).

The effect of space charge on head-tail modes has also been observed in experiments [260] in the heavy-ion synchrotron SIS18, GSI Darmstadt. Figure 56 shows an example of the bunch spectrum for q ≈ 4.5, where the mode k = 1 dominates. Interestingly, the mode k = - 1 is also clearly seen, which is strongly shifted downwards and is usually damped in agreement with the theory.

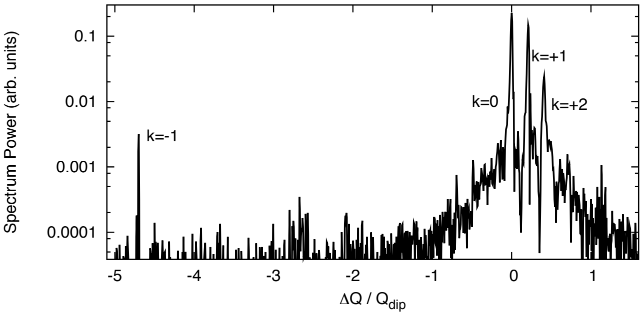

Fig. 56. Transverse coherent spectrum for a bunch with space charge in SIS18, GSI Darmstadt [260], the mode eigenfrequency shifts correspond the effect of space charge according to a modified [260] airbag model [247].

The head-tail eigenmodes in bunches with strong space charge for realistic distributions can be calculated numerically using the theories [249-251]. Figure 57 demonstrates that even for bunches with space charge q = 6 the airbag predictions are very close to the complete theory results. Also experimental observations [260] of the bunches with space charge confirmed this.

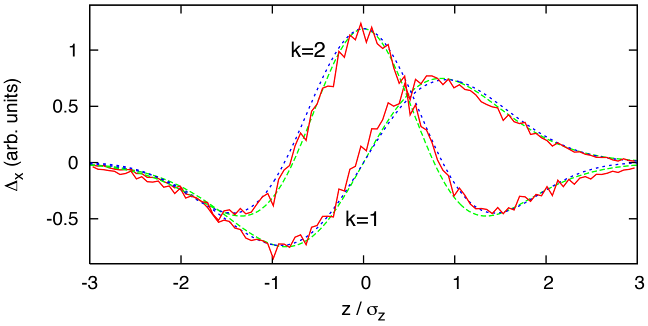

Fig. 57. Dipole moments from simulations [252] for a Gaussian bunch (red lines), theory eigenfunctions for a Gaussian bunch from [249,250] (green lines) and for the airbag bunch (blue lines).

The effect of space charge on the eigenmodes saturates for strong space charge, thus the instability growth rates saturate for strong space charge as well [247-250,252]. Since the frequency shifts within the sidebands are relatively small, and the eigenmode modifications due to space charge are relactively weak, the effect on the instability increments is not strong. The important effect of space charge on head-tail instability is the Landau damping induced by the space charge tune spread. It was predicted theoretically in [249-251] and observed and quantified numerically in [252]. This damping is due to interaction of the coherent mode with the incoherent particle spectrum. In opposite to the coasting beam [261], the tune spread due to space charge provides damping for the bunch eigenmodes. The bunch transverse and longitudinal distribution define the space charge tune spread and thus determine the damping. This is illustrated in Fig. 58, where the transverse K-V distribution is compared with the 3D-Gaussian bunch.

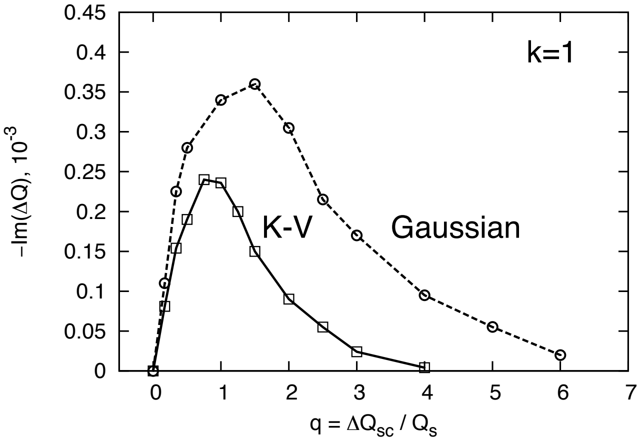

Fig. 58. Decrement of the space charge damping from particle tracking simulations for $k = 1$ head-tail mode. Solid lines correspond to the longitudinal Gaussian and transversal K-V bunches from [252]. Dashed lines are for the Gaussian (longitudinal and transversal) bunches [262,263].

The decrement of the space charge induced damping has been analytically estimated [249], for strong space charge $q >> 2k$,

$$\mathrm{Im}\left(\Delta Q\right) \sim -\frac{k^4 Q_s}{q^3}. \tag{32}$$

The simulation results [252] confirmed the scaling of the damping rate with the mode number and with q. The absolute values of the damping decrement depend on the given bunch distribution because it defines the number of resonant particles which interact with the coherent wave. The damping of bunch eigenmodes can be enhanced by larger incoherent tune spread [262], for example due to octupoles [264,265], RF nonlinearities, or detuning wakes [10]. Also coherent tune shifts which push the eigenmodes closer to the incoherent spectrum can significantly enhance the space charge damping and change the stability thresholds. For example, image charges in the vacuum pipes can provide an enhancing effect on damping [262,263]. Another important effect of space charge on collective instabilities is the suppression of the transverse mode coupling instability [2,247,249]. This instability appears because the coherent tune shifts due to impedances/wakes are different for different bunch eigenmodes, and the crossing the modes frequencies trigger fast high-frequency instabilities. If the eigenmode tune shifts are dominated by space charge, it can prevent the coupling due to the impedances.

C. Beam-Beam

1) Weak-Strong: Landau damping of head-tail modes due to incoherent beam-beam effects

Most hadron synchrotrons rely on lattice nonlinearities for Landau damping of impedance driven coherent modes of oscillation. However, in a collider, the presence of beam-beam interactions strongly modifies the transverse amplitude detuning and therefore the resulting stability diagram. Numerical investigations of this effect are discussed, supported by observations at the LHC.

In circular hadron colliders, the amplitude detuning due to beam-beam interactions largely exceeds the one caused by lattice non-linearities, having a significant impact on the Landau damping effect on coherent modes oscillations driven by the beam coupling impedance. Furthermore, the type and strength of the beam-beam interactions vary strongly during the operational cycle, it is therefore crucial to be able to quantify the Landau damping including the effect of beam-beam interactions during all phases of the operational cycle of the collider. While the effect of lattice non-linearities can be addressed analytically, the complex configuration of beam-beam interactions leads to amplitude detuning with difficult analytical expressions [266,267], which render the solution of the dispersion relation difficult. This problem is easier addressed numerically, using single particle tracking to evaluate the amplitude detuning and numerical integration of the dispersion integral [268,269]. The non-linearities of beam-beam interactions not only modify the amplitude detuning but can also significantly distort the particles distribution in the beam, affecting the strength of the Landau damping. Both these incoherent effects of beam-beam interactions are discussed in this paper.

a) Long-Range interactions

To first order the amplitude detuning from the lattice can be written:

$$\begin{cases} \Delta Q_x = a_x J_x + a_{xy} J_y \\ \Delta Q_y = a_{yx} J_x + a_y J_y \end{cases}. \tag{33}$$

In the LHC, the main component of the lattice detuning is controlled via a dedicated set of octupole magnets, arranged such that $a_x \approx a_y$ and $a_{xy} \approx a_{yx}$ in order to ensure equivalent Landau damping in both transverse plans [270]. Furthermore, the amplitude detuning arising from a set of long-range interactions around two Interaction Points (IPs) located at opposite azimuth in the ring, with crossing angles in alternating planes can be written with the same form, with [266]

$$\begin{cases} a_x = a_y = \dfrac{3\,N_{LR}\,\xi}{2\,d^4} \\ a_{xy} = a_{yx} = -\dfrac{3\,N_{LR}\,\xi}{d^4} \end{cases}, \tag{34}$$

with N_{LR} the number of long-range interactions around each IP, d the separation between the beams at the location of the interactions normalised to the beam size, and where the beam-beam parameter is defined as

$$\xi = \frac{N_b\,r_p}{4\,\pi\,\varepsilon_{tn}}. \tag{35}$$

The combined effect of the lattice octupoles and of long-range interactions is therefore constructive if the octupoles are set such that the direct detuning coefficients are positive and the cross terms negative and destructive otherwise (see also [271,272). Higher order components of the amplitude detuning induced by long-range interactions needs to be included in order to obtain a quantitative estimation of their effect on the Landau damping, however the first order usually dominates, therefore the statement on the sign of the coefficients holds for all configurations where the two effects have similar strength. Nevertheless, in the LHC their relative strength varies significantly during the operational cycle. The strength of the octupoles is dominant in the first part of the cycle, when the separation between the beams at the location of the beam-beam interaction is large. The reduction of the β-function at the IP, during the so-called betatron squeeze, reduces the normalised separation between the beams at the location of long-range interaction increasing their strength to a level comparable to the one of the octupoles. During this operation, the detuning is either increased or reduced depending on the sign of the detuning coefficients, as illustrated in Fig. 59. While the so-called positive polarity of the octupoles seems at first sight preferable, the actual preference is more subtle. Indeed, depending on the real part of the imaginary tune shifts expected, one of the polarity might be preferred when the beams are well separated. Indeed, before the betatron squeeze, one observes that the stability diagram arising from the negative polarity is slightly shifted in the negative imaginary parts with respect to the positive polarity, which makes it a favourable solution in case the expected imaginary tune shifts are negative, as in the LHC [47]. Therefore, the best choice of polarity results from a careful optimisation of the beam stability with weak and strong long-range interactions, i.e. before and after the betatron squeeze.

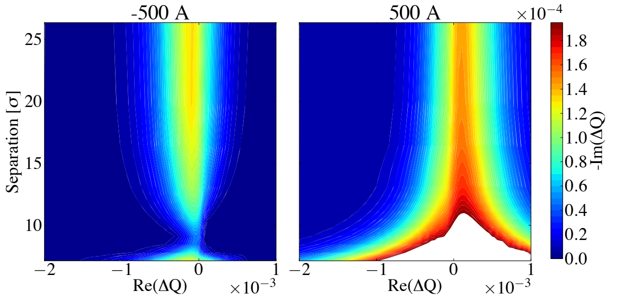

Fig. 59. Evolution of the stability diagram as the normalized separation between the beams is reduced during the betatron squeeze for the nominal LHC optics and beam parameters [269]. At the end of this operation, nominal LHC beams have a normalized separation of 10 σ.

During the 2012 run of the LHC, instabilities were observed at the end of the squeeze with both polarities of the octupole [269], excluding this mechanism as a sole explanation for the instabilities observed, in particular when the contribution of long-range beam-beam interaction and the octupole contibute constructively to the stability diagram. Nevertheless, the size of the amplitude detuning is not the only consideration to take into account, as the dynamics of single particles is highly affected by both the long-range interactions and the lattice non-linearities. This matter is discussed later.

b) Head-On interactions

The main component of the amplitude detuning due to head-on interactions is not linear with the transverse actions and therefore has a very different impact on the stability diagram with respect to the lattice non-linearities and long-range interactions. This feature is clearly visible in the tune footprint in Fig. 60.

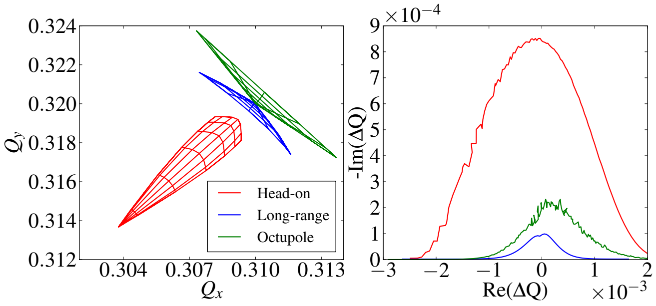

Fig. 60. Comparison of the amplitude detuning represented by the transverse tunes Q_x and Q_y for particles oscillating at different amplitudes in a so-called tune footprint (left) and the corresponding stability diagrams (right) generated by octupole magnets, long-range beam-beam interactions in IP1 and 5 or head-on beam-beam interactions in IP1 and 5. The machine and beam parameters are those of the nominal LHC.

The corresponding stability diagrams obtained numerically shows the different contributions. In particular, one observes that head-on interactions provides a larger stability diagram for a similar amplitude detuning, due to the strong amplitude detuning for the most populated part of the distribution, i.e. for the particles oscillating with small amplitudes. Due to this difference, the lattice detuning as well as the effect of long-range interactions have a negligible impact on the stability diagram when the beams are colliding head-on. This interesting feature of head-on interactions is considered as a potential solution to increase the beam stability earlier in the cycle, e.g. by bringing the beams into collision before the betatron squeeze, thus avoiding the difficulties linked to the interplay of long-range interactions and the lattice non-linearities discussed before, provided that all bunches in the machine experience a head-on collision [271]. Similarly, an electron lens providing an amplitude detuning similar to the one of head-on beam-beam interactions [272] could be envisaged to efficiently provide a large stability diagram before head-on collisions are established, instead of the relying on lattice non-linearities or octupole magnets which might have detrimental effects on the single particle dynamics.

The beams in hadron colliders collide with small transverse offset, i.e. in the order of the beam size at the interaction point, in a transient phase aiming at bringing the beams into collision or when an orbit bump is introduced statically in order to artificially reduce the luminosity for different experimental purposes. During such phases, the amplitude detuning varies from a configuration dominated by the lattice non-linearities and long-range interactions to a configuration dominated by head-on interactions, as illustrated by the tune footprints in Fig. 61. The corresponding evolution of the stability diagram in the horizontal plane is shown in Fig. 62. In particular, one observes that the change of sign of the tune shift and amplitude detuning leads to a systematic cancellation of the imaginary part in the dispersion integral, leading to a minimum of Landau damping with beams separated by around 1.5 σ [269].

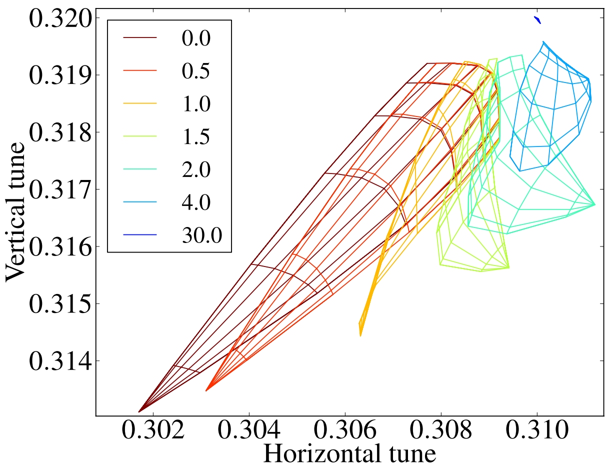

Fig. 61. Example of tune footprint of a bunch colliding in IP1 with different separations in the horizontal plane.

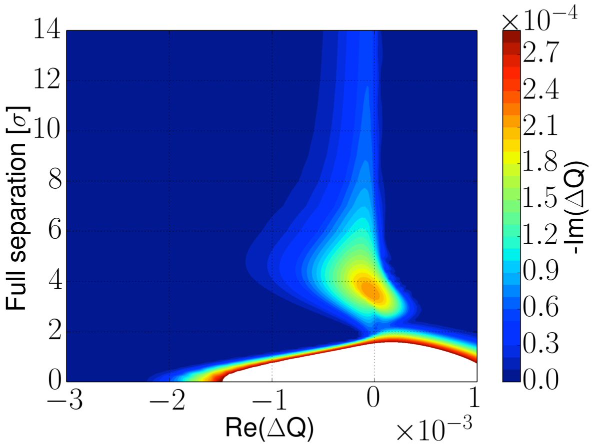

Fig. 62. Evolution of the stability diagram while varying the separation between the beams at the interaction point.

During the 2012 run of the LHC, the luminosity was leveled with a transverse offset in IP8. While not harmful for most bunches with head-on interactions in IP1 and 5, this technique turned out to be critical for a subset of bunches without head-on collision in other experiments. Indeed, the situation of these bunches is similar to the one described in Fig. 62. Observations of such instabilities during a fill dedicated to luminosity production are shown in Fig. 63. Many bunches experience an instability at the very beginning of luminosity production, during the adjustment of the orbit at the IP, while the separation is larger than 3 σ. Yet, most bunches lose their intensities in a normal way during 5 hours of luminosity production and, suddenly, lose a significant fraction of their intensity on a time scale of a second. Simultaneously, a coherent oscillation of the beam was measured. It is important to note that a coherent signal is observed only in a single beams, the other beam is not affected by the instability. This excludes the coupled coherent beam-beam modes as an explanation for these instabilities [273]. A mechanism similar to the one described above, based on the destructive interplay of the lattice non-linearities and the octupolar component of the beam-beam interaction, was suggested to explain beam losses when bringing the beams into collision at CERN's Intersecting Storage Rings [274]. It is however likely that these losses were of a similar nature of those observed when levelling the luminosity with a transverse offset at the LHC.

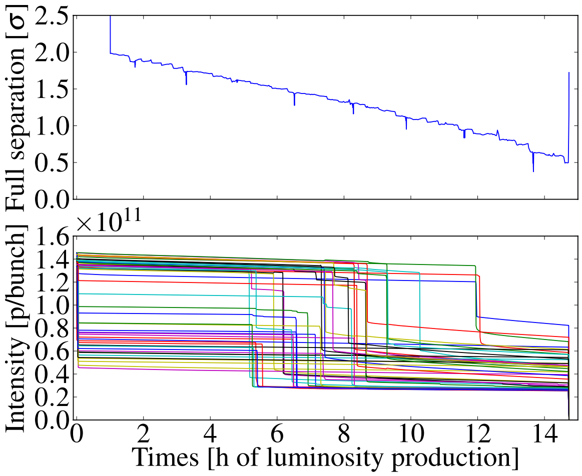

Fig. 63. Above, separation between the beams at the interaction point during luminosity leveling with a transverse offset in IP8, derived from measured luminosity in IP1,5 and 8, expressed in units of the transverse beam size. Below, the intensity of the 49 bunches colliding only in IP8, the other 1331 bunches follow a standard quasi-exponential decay.

Due to its derivative in the nominator of the dispersion integral, variations of the beam distribution significantly impact the stability diagram. This parameter is unfortunately poorly measured in hadron colliders. In particular the presence of under or over populated tails in the beam distribution have a great impact on the stability diagram [275]. The presence of diffusion mechanisms acting on specific parts of the distribution can have an even greater impact on the stability diagram for small distortions of the distribution. Let us illustrate this phenomenon, by considering the distribution of particles in a beam experiencing a linear amplitude detuning and an external source of noise, modelled by a harmonic excitation of frequency within the beam frequency spread and a finite correlation time. Such noise enhances the diffusion of resonant particles, as confirmed by a multiparticle tracking simulation. Indeed, the depletion of the distribution at the action of resonant particles is visible, as well as the overpopulation for slightly larger actions. This effect has been studied for a different purposes, e.g. in [276]. The measurable effect on the distribution in real space is beyond available measurement accuracy. Nevertheless, the effect on the stability diagram is significant, as illustrated by the comparison of the stability diagram obtained using the initial and perturbed distributions (see Fig.64).

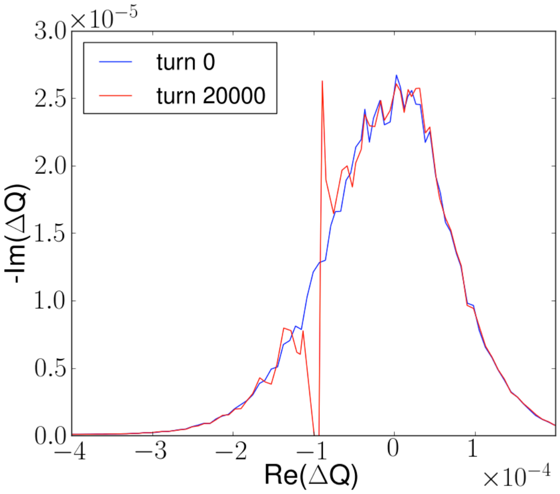

Fig. 64. Comparison of the stability diagram for a distribution perturbed by an external source of noise (red) to the one obtained with a Gaussian distribution (blue).

While the presence of such a source of noise is unlikely in a machine like the LHC, there are other mechanisms that could lead to a similar distortion of the distribution. In the presence of a wideband source of noise, e.g. from the power supply ripples, the ground motion or the noise in the transverse feedback, the beam response will be higher at the frequency of the coherent modes excited by the beam coupling impedance. Such excitation can enhance the diffusion of the resonant particles responsible for the Landau damping of these modes, eventually leading to a loss of Landau damping [277].

The strong non-linearities of beam-beam interactions also provoke the diffusion of the particle in specific areas of phase space. In particular, single particle tracking studies have revealed that the LHC configuration in the second part of the 2012 run featured a dynamic aperture around 4 σ at the end of the betatron squeeze [278]. The corresponding frequency map analysis of the single particle motion revealed significant diffusion mechanisms for particles with even lower amplitudes, which could have a strong impact on the beam distribution and consequently on the stability diagram. Such a mechanism could explain the discrepancy discussed before, studies are on going to quantify the behaviour of the beam distribution under the influence of strong non-linearities and its impact on the stability diagram.

In summary, beam-beam interactions have an impact on both the amplitude detuning and the beam distribution, the strength of the Landau damping on head-tail modes is greatly affected by these modifications. A good knowledge of the different contributions, as well as their variation during the different operational procedures is crucial in order to ensure the beam stability during the full cycle.

2) Strong-Strong: Coherent modes of oscillation due to beam-beam interactions and the beam coupling impedance

In high brightness circular colliders, the coherent and incoherent beam dynamics are dominated by beam-beam interactions. It is generally assumed that the incoherent tune spread introduced by the beam-beam interactions is sufficient to prevent any instability driven by the beam coupling impedance. However, as the two counter-rotating beams interact they can give rise to coherent dipole modes and therefore modify the coherent beam dynamics. The stability of the beams under the influence of both beam-beam interactions and the beam-coupling impedance is investigated using a linearized model and macro-particle simulations.

As they interact with each other, the two beams will couple, resulting in coherent oscillations. In the case of equal bunches and tunes these coherent oscillations can be described by two eigenmodes, corresponding to either in-phase or out-of-phase oscillations, respectively the σ and π modes. The tune shift between σ and π modes is equal to $Y\xi$, where Y is the Yokoya factor and ξ the beam-beam parameter [279]. These coherent modes have been routinely observed in various colliders and are generally not self-excited [280,281]. However, the frequency of these modes may be well separated from the incoherent tune spread and consequently they do not profit from the large intrinsic Landau damping properties of the beam-beam interactions [282]. Under external excitation, such as machine impedance, these modes could therefore become unstable. Assessing the stability of colliding beams therefore requires considering these two processes simultaneously and in a self-consistent way. Past studies have shown that the combination of beam-beam interactions and impedance could lead to coherent instabilities. However, these studies were either performed using a linearized model [283], i.e. not including Landau damping, or for very specific cases applied to the Tevatron [284]. During the 2012 proton run of the LHC, coherent instabilities of colliding beams were routinely observed [285], triggering a renewed interest to pursue these studies in a more general scope. This section will give a review of the recent progress made regarding multi-particle strong-strong simulations of the interplay of beam-beam and impedance. A complete study of these effects and benchmarking of the numerical tools presented in the following can be found in [286] and the reader may refer to this paper for details. The motivation for this study being mainly driven by LHC observations, the LHC impedance model and beam parameters will be used, the numerical tools developed are however applicable to any configurations and the results should be qualitatively similar for other designs.

a) Numerical Models

Two models were developed or more precisely extended to characterize the interplay of beam-beam and impedance:

- a linearized model based on the circulant matrix approach introduced in [287];
- a fully self-consistent multi-particle tracking model. Single bunch effects were studied with the code BEAM-BEAM3D [233] and multi-bunch effects with the code COMBI [288].

The Circulant Matrix Model (CMM) was introduced in [287] and later extended to include single bunch head-on beam-beam interactions in [283]. More recently, this method was extended to an arbitrary number of bunches and IPs including long-range interactions and bunch train structures [286]. Transverse damper, chromaticity and arbitrary wake function were also included in our implementation. The two parallelized tracking codes used for this study, BEAMBEAM3D and COMBI, feature very similar implementations. The main differences reside in the field solver and the parallelization concepts. The field solvers are well documented in Refs. [289] and [290]. BEAMBEAM3D is intended for single bunch simulations allowing for longitudinal slicing at the collision point while COMBI allows for multi-bunch simulation but the beam-beam kick is computed with a 4D lens to optimize the computation time. Both codes were extended to include self-consistent impedance calculation following similar implementation as the wake fields tracking code HEADTAIL. The bunches are modeled as an ensemble of particles initialized with random Gaussian distributions in the 6 dimensions. After each turn the bunches are sliced longitudinally and the dipole moments of each of the slices as well as their charge is computed, such as to compute wake fields and apply the corresponding kicks. Similarly to the CMM, transverse damper, chromaticity and in addition, non-linear fields are available for stability studies. Figure 65 and 66 illustrate benchmarking simulations comparing the results of the CMM and the multi-particle tracking codes, a perfect agreement is observed.

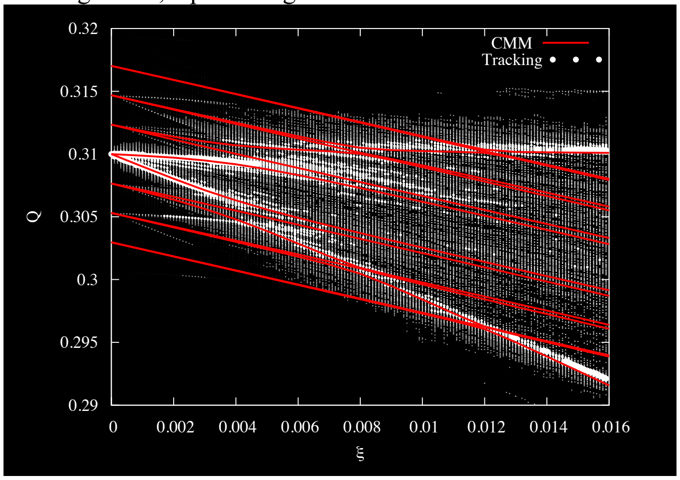

Fig. 65. Synchro-betatron modes as a function of the beam-beam parameter for Q' = 0 and $\beta^* / \sigma_s \approx 1$. Impedance was not included in this case. The white dots are the results from the tracking and the red lines from the CMM.

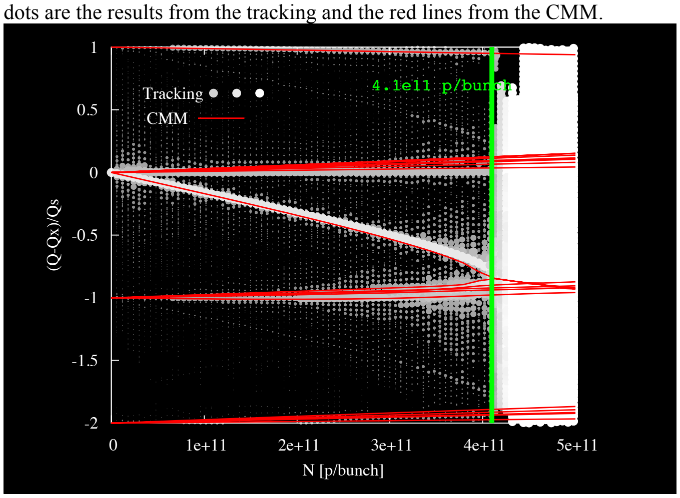

Fig. 66. Intensity scans at Q' = 0. The red lines are from the CMM and the colored spectrogram from multi-particle tracking.

b) Single-bunch simulations

The main result obtained with these simulation codes was the demonstration of the existence of an impedance driven transverse mode coupling instability involving the beam-beam coherent modes. As the beam-beam π mode approaches the headtail mode -1 ($\xi \approx Q_s$), their frequencies become equal and they couple leading to strong instabilities with similar rise times and characteristics to the classical impedance driven Transverse Mode Coupling Instability (TMCI). This is observed both in the tracking and CMM with comparable rise times as shown in Figs. 67 and 68 illustrating scan in beam-beam parameter at constant impedance.

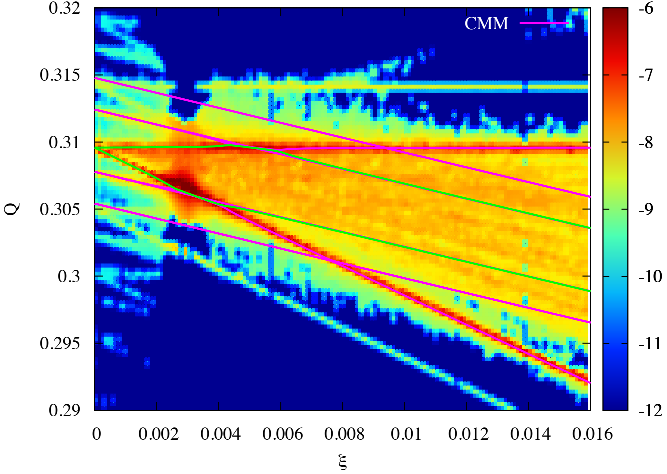

Fig. 67. Synchro-betatron modes as a function of the beam-beam parameter for Q' = 0 and $\beta^* / \sigma_s \approx 90$. The colors correspond to the amplitude of the spectral line. Impedance effects were kept constant over the whole scan. The most unstable modes are shown in green.

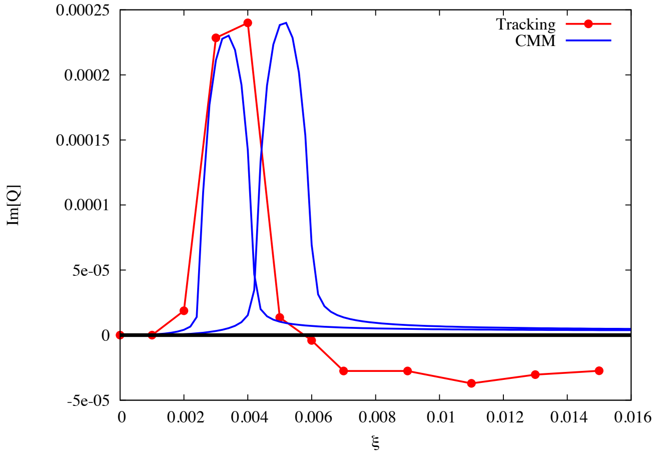

Fig. 68. Imaginary part of the tune shift of the most unstable modes as a function of the beam-beam parameter for Q' = 0 and $\beta^* / \sigma_s \approx 90$. Impedance effects were kept constant over the whole scan.

These results were later confirmed in a dedicated experiment performed at the LHC. Applying a transverse offset is an efficient way to vary the beam-beam parameter without having to re-inject bunches of different intensities. This experimental setup was therefore chosen to efficiently verify the simulation results. Figure 69 shows a spectrogram of the vertical plane of Beam 1 over the duration of the whole experiment.

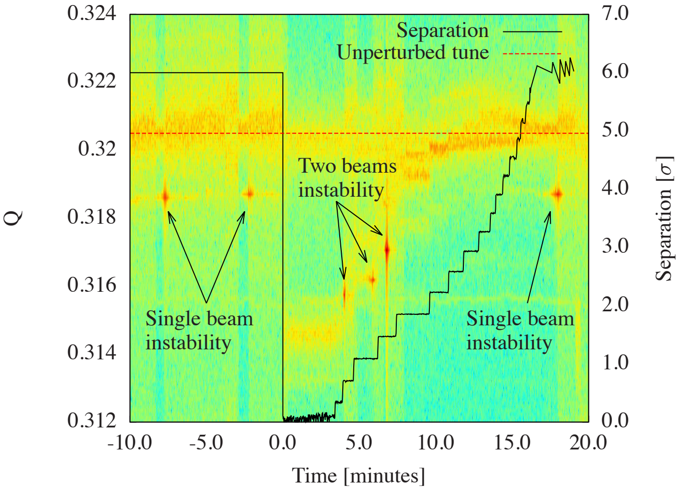

Fig. 69. Spectrogram from turn-by-turn data for the vertical plane of beam 1. The separation is derived from luminosity data.

When separated by 6 σ, the vertical plane of beam 1 was found to be unstable without transverse damper for an octupole current up to 480 A. These single beam instabilities can be observed before t = 0 when the octupole current was raised in steps in an attempt to stabilize the beam without transverse damper and at the end of the separation scan when the separation is back to 6 σ. The measured rise time for these single beam instabilities was estimated to 5.9 s. In this case the frequency of the unstable mode appears to correspond to the first lower synchrotron sideband (headtail mode -1). Bringing the beams into collision in one of the two IPs, at t = 0, provides stability even in the absence of transverse damper. This was expected from the large beam-beam tune spread and the absence of mode coupling instabilities at $\xi >> Q_s$. As the vertical separation is increased in steps we observed the appearance of instabilities for intermediate separations between 0.7 σ and 1.4 σ corresponding to $\xi \approx Q_s$ (Q_s being shifted by the quadrupolar part of the beam-beam force). These instabilities have quite different characteristics than the ones observed at large separation. They appear to involve both beams at the same time and their rise-time was measured to be approximately 1.8 s, which is approximately a factor 3 faster than the single beam instabilities. Finally the frequency of the unstable mode is different and is consistent with the beam-beam π mode. It should be noted that in all instances turning ON the transverse damper restored the beam stability. A full set of simulations were performed to confirm the observation of a mode coupling instability and provided strong arguments in this direction, the details of the calculations can be found in [273]. Although this instability may seem very harmful for high bunch intensity operation of a collider, it was shown from CMM calculation and tracking simulation that both chromaticity and transverse damper can mitigate the transverse mode coupling instability. The transverse damper appears to be very efficient, while very high chromaticity would be required in the absence of transverse damper. This result is consistent with experimental data which showed that the transverse damper was very efficient to cure these instabilities.

c) Multi-bunch simulations

In the LHC, for 25 ns bunch spacing, individual bunches can experience up to 32 long-range interactions per IP (this number goes down by a factor 2 for 50 ns bunch spacing), where the separation between the two beams is approximately 10 σ. In some cases, the accumulated tune shifts from these interactions can become larger than the synchrotron frequency, potentially leading to mode coupling instabilities. In our model, each interaction region is modeled as a series of long-range interactions with constant separation located at phase advances of ± π / 2 from the IP. Once in collision, the beam dynamics is dominated by the head-on interactions. We will therefore concentrate on the case with long-range interactions only which corresponds to the LHC once the β-function at the IP has been reduced, i.e. after the so-called betatron squeeze. Over this period the separation at the IP is of the order of 40 σ. This additional long-range encounter is therefore neglected in the following analysis. At the locations of the long-range encounters $\beta / \sigma_s >> 1$ and the beam-beam interaction can be reduced to the 4D case. Due to their train structure, the LHC beams suffer the so-called PACMAN effects: bunches along the trains will experience different number of long-range encounters and hence have different tune shifts leading to a large variety of coherent modes with nearby frequencies.

Figure 70 illustrates the impact of PACMAN effects for a simplified case. Two trains of 8 bunches are colliding in a single IP, the PACMAN effects are artificially enhanced by allowing collisions only on one side of the IP. Each bunch therefore experiences up to 7 long-range interactions. Even for this simplified case a large number of mode coupling instabilities are observed involving various modes. As the separation is reduced, and hence the beam-beam tune shift is increased, the probability for two modes to overlap become higher and in some cases multiple mode coupling instabilities can occur simultaneously.

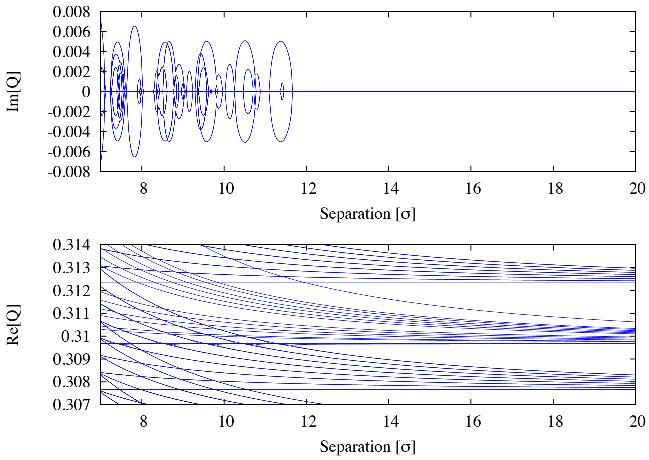

Fig. 70. Real (bottom) and imaginary (top) part of the coherent tunes of the modes obtained with the CMM for two trains of 8 bunches colliding in one IP with $Q' = 0$ and no transverse feedback. The PACMAN effects are enhanced by allowing collisions only on one side of the IP.

Figure 71 shows the imaginary part of the tune of the most unstable mode derived with the CMM as a function of both chromaticity and damper gain. The separation was set to 13 σ for which strong mode coupling instabilities are observed. Above 500 turns damping time or a chromaticity of 10 a significant decrease of the growth rate is observed indicating a mitigation of the mode coupling instability.

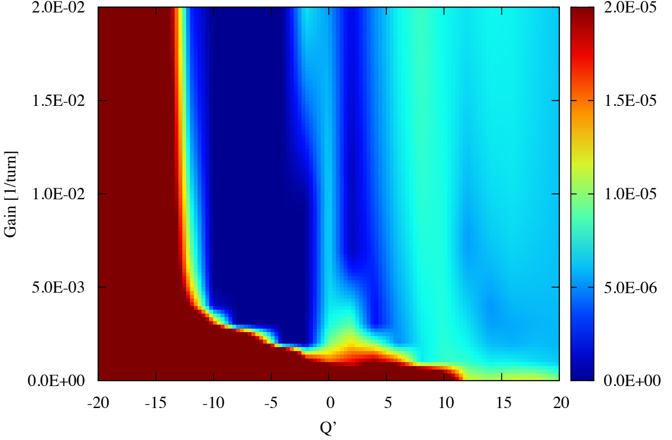

Fig. 71. Imaginary part of the tune of the most unstable mode obtained with the CMM for two trains of 16 bunches colliding in one IP, for different chromaticity and damper gain at separations of 13 σ.

D. Three-Beam Instability?

An electron cloud influences proton oscillations in two aspects. First, it works as a static lens, shifting up all coherent and incoherent tunes. This lens is nonlinear; the tune shifts of the transverse tails are smaller than those of the core, so, contrary to the linear part, the nonlinearity of e-clouds is *defocusing*. E-cloud nonlinearity changes the incoherent spectrum, i.e. it modifies Landau damping; taken by itself, it is a stabilizing factor. The second aspect of e-cloud is that it is a reactive medium, whose response to proton perturbations is similar to a low-Q impedance [291-293]. Collective response of the electron cloud introduces the growth rates and coherent tune shifts of the circulating beam, so by itself it is a destabilizing factor. This brief qualitative analysis already shows that e-cloud is a controversial entity: it introduces both stabilizing and destabilizing factors.

Each of these factors is definitely stabilizing or destabilizing only by itself. When e-clouds are combined with other nonlinearities and impedances, these factors may work in the opposite direction [294]. The cloud nonlinearity could partially cancel one of the octupoles or beam-beam, thus reducing the stability area. The coherent tune shift of the electron cloud, in its turn, could partially compensate one of the regular impedance, thus reducing the amount of nonlinearity needed for the stabilization.

One more agent able to modify e–cloud effects is the beam space charge. If the space charge tune shift exceeds ones of e-cloud, the latter would not play any role in the Landau damping, so e-cloud would be purely destabilizing. However, there are some reasons to speculate that e-cloud nonlinearity may be sufficient to suppress the instability driven by its impedance. If it is true, then without space charge and by itself e-cloud may let the beam to remain stable. In this case, in the presence of space charge, conditions for e-cloud instability limit the electron intensity not only from below but also from above [295].

Electron cloud instabilities may have special features at the LHC as a proton-proton collider. Since the two beams share the same vacuum chamber at the vicinity of detectors, the build–up of e-cloud could be stronger in these areas, being affected by two beams. This enhanced build–up allows to speculate about the “three–beam instability”, or the “beam-beam-beam effect” [294] as a possible explanation of the end-of-the-squeeze instability regularly observed during the Run I [238]. Due to the betatron squeeze, the beam sizes increased at the sensitive areas, slowing fast oscillations of the electron wake along the proton bunch, and thus making the beam more prone to the instability. Together with this impedance growth, another important effect of the electron cloud may happen at certain cloud intensity: its nonlinearity may partially compensate one of the machine octupoles, leading to a partial collapse of the stability diagram. Thus, impedance and nonlinearity factors of the electron cloud may be reasons for the end-of-the-squeeze instability at the LHC. Is it really so or not is an open question so far.

VI. CONCLUSION

Beam instabilities have been studied for several decades and many intricate phenomena have been revealed. They were very often treated separately in the past but since some time the need to study several mechanisms together appeared, to try and better explained the reality of our accelerators. With the increasing power of our computers this becomes easier but the need to continue and develop theories remains, to have a better understanding of the interplays between all these effects, which is the current challenge in the study of beam instabilities.

REFERENCES

[1] A.W. Chao, Physics of Collective Beam Instabilities in High Energy Accelerators, New York: Wiley, 371 p, 1993.

[2] K.Y. Ng, Physics of Intensity Dependent Beam Instabilities, World Scientific, 776 p, 2006.

[3] S. Myers and H. Schopper (Editors), Elementary Particles – Accelerators and Colliders, Landolt-Börnstein, Springer, 2013 (Chapter 4).

[4] B. Zotter, Betatron Frequency Shifts due to Image and Self Fields, CERN Accelerator School: General Accelerator Physics, CERN 85-19, Vol. I, p. 253, 1985.

[5] K. Schindl, Space Charge, CERN-PS-99-012-DI, 1999.

[6] L.J. Laslett, On Intensity Limitations Imposed by Space Charge Effects in Circular Particle Accelerators, in Proc. Summer Study on Storage Rings, Accelerators and Instrumentation at Super High Energies, BNL Report 7534, p. 324, 1963.

[7] K. Yokoya, Resistive Wall Impedance of Beam Pipes of General Cross Section, Part. Accel., vol. 41, 3-4, p. 221, 1993.

[8] A. Sessler and V. Vaccaro, CERN Report ISR-RF/67-2 (1967).

[9] H. Tsutsui, On single Wire Technique for Transverse Coupling Impedance Measurement, CERN-SL-Note-2002-034 AP, 2002.

[10] A. Burov and V. Danilov, Suppression of Transverse Bunch Instabilities by Asymmetries in the Chamber Geometry, Phys. Rev. Lett. 82, 2286-2289 (1999).

[11] N. Mounet and E. Métral, Impedances of Two Dimensional Multilayer Cylindrical and Flat Chambers in the Non-Ultrarelativistic case, Proc. Of ICFA HB2010, Morschach, Switzerland, Sept. 27 – Oct. 1, 2010.

[12] CST Particle Studio (http://www.cst.com/Content/Products/PS/Overview.aspx).

[13] F. Caspers, Bench Measurements, in Handbook of Accelerator Physics and Engineering, 2nd Printing, Edited by A.W. Chao and M. Tigner, p. 574.

[14] Ansoft – HFSS (http://www.ansoft.com/products/hf/hfss/).

[15] E. Métral et al., Kicker Impedance Measurements for the Future Multiturn Extraction of the CERN Proton Synchrotron, Proc. Of EPAC2006, Edinburgh, UK, 26-30 June 2006.

[16] H. Day et al., Simulations of Coaxial Wire Measurements of the Impedance of Asymmetric Structures, Proc. IPAC11, San Sebastian, Spain, September 4-9, 2011.

[17] L.J. Laslett, V.K. Neil and A.M. Sessler, Transverse Resistive Instabilities of Intense Coasting Beams in Particle Accelerators, R.S.I, 36(4), 436-448, 1965.

[18] B. Zotter, New Results on the Impedance of Resistive Metal Walls of Finite Thickness, CERN-AB-2005-043, 2005.

[19] E. Métral, Transverse Resistive-Wall Impedance from Very Low to Very High Frequencies, CERN-AB-2005-084, 08 August 2005.

[20] A.M. Al-Khateeb et al., Transverse Resistive Wall Impedances and Shielding Effectiveness for Beam Pipes of Arbitrary Wall Thickness, Phys. Rev. ST Accel. Beams 10, 064401 (2007).

[21] F. Roncarolo et al., Comparison Between Laboratory Measurements, Simulations, and Analytical Predictions of the Transverse Wall Impedance at Low Frequencies, Phys. Rev. ST Accel. Beams 12, 084401 (2009).

[22] N. Mounet and E. Métral, Impedances of an Infinitely Long and Axisymmetric Multilayer Beam Pipe: Matrix Formalism and Multimode Analysis, Proc. Of the 1st International Particle Accelerator Conference, Kyoto, Japan, 23 – 28 May 2010.

[23] N. Mounet and E. Métral, Generalized Form Factors for the Beam Coupling Impedances in a Flat Chamber, Proc. Of the 1st International Particle Accelerator Conference, Kyoto, Japan, 23 – 28 May 2010.

[24] B. Salvant et al., Quadrupolar Transverse Impedance of Simple Models of Kickers, Proc. Of the 1st International Particle Accelerator Conference, Kyoto, Japan, 23 – 28 May 2010.

[25] C. Zannini et al., Electromagnetic Simulations of Simple Models of Ferrite Loaded Kickers, Proc. Of the 1st International Particle Accelerator Conference, Kyoto, Japan, 23 – 28 May 2010.

[26] E. Métral, Beam Screen Issues (with 20 T dipole magnets instead of 8.3 T), Proc. Of the High-Energy LHC workshop, Malta, 14-16 October 2010.

[27] E. Métral and G. Rumolo, USPAS course on collective effects, Albuquerque, USA (June 2009).

[28] B. Zotter, “Transverse oscillations of a relativistic particle beam in a laminated vacuum chamber,” 1969, report No. CERN-69-15.

[29] E. Keil and B. Zotter, “The impedance of layered vacuum chambers,” in 6th European Particle Accelerator Conference, Stockholm, Sweden, 1998, pp. 963–965.

[30] E. Métral, B. Zotter, and B. Salvant, “Resistive-wall impedance of an infinitely long multi-layer cylindrical beam pipe,” in 22nd Particle Accelerator Conference, Albuquerque, USA, 2007, pp. 4216–4218.

[31] N. Mounet and E. Métral, “Electromagnetic fields created by a macroparticle in an infinitely long and axisymmetric multilayer beam pipe,” 2009, report No. CERN-BE-2009-039.

[32] A. Burov and V. Lebedev, “Tranverse resistive wall impedance for multi-layer round chambers,” in 8th European Particle Accelerator Conference, Paris, France, 2002, pp. 1452–1454.

[33] N. Wang and Q. Qin, “Resistive-wall impedance of two-layer tube,” Phys. Rev. ST Accel. Beams, vol. 10, no. 111003, 2007.

[34] H. Hahn, “Matrix solution of coupling impedance in multi-layer circular cylindrical structures,” in 23rd Particle Accelerator Conference, Vancouver, Canada, 2009.

[35] M. Ivanyan, E. Laziev, V. Tsakanov, A. Vardanyan, S. Heifets, and A. Tsakanian, “Multilayer tube impedance and external radiation,” Phys. Rev. ST Accel. Beams, vol. 11, no. 084001, 2008.

[36] H. Hahn, “Matrix solution to longitudinal impedance of multi-layer circular structures,” 2008, report No. BNL-81867-2008-IR.

[37] R. L. Gluckstern, J. van Zeijts, and B. Zotter, “Coupling impedance of beam pipes of general cross section,” Phys. Rev. E, vol. 47, pp. 656–663, 1993.

[38] B. Salvant, N. Mounet, C. Zannini, E. M´etral, and G. Rumolo, “Quadrupolar transverse impedance of simple models of kickers,” in 1st International Particle Accelerator Conference, Kyoto, Japan, 2010, pp. 2054–2056.

[39] A. Piwinski, “Wake fields and ohmic losses in flat vacuum chambers,” 1992, report No. DESY-HERA 92-04.

[40] K. Bane, Y. Cai, A. Drozhdin, R. Helm, L. Keller, J. Irwin, R. Messner, R. Nelson, T. Raubenheimer, G. Stupakov, F. Tian, D.Walz, M.Woodley, Y. Yan, and F. Zimmermann, “Chap. 9: Collimation systems,” in Zeroth- Order design report for the Next Linear Collider. SLAC, 1996, p. 571, report No. LBNL-5424, SLAC-R-474, UC-414, UCRL-ID-124161; http: //www.slac.stanford.edu/accel/nlc/zdr/Snowmass96/ZDRCH09.PDF.

[41] F. Zimmermann, “Coherent and incoherent tune shift induced by the nonlinear flat-chamber resistive-wall wake field with an application to the LHC collimator experiment in the SPS,” 2006, cERN-AB-Note-

2006-007 ABP.

[42] H. Henke and O. Napoly, “Wake fields between two parallel resistive plates,” in 2nd European Particle Accelerator Conference, Nice, France, 1990, pp. 1046–1048.

[43] A. Piwinski, “Longitudinal and transverse wake fields in flat vacuum chambers,” 1984, report No. DESY 84-097.

[44] A. Burov and V. Lebedev, “Tranverse resistive wall impedance for multilayer flat chambers,” in 8th European Particle Accelerator Conference, Paris, France, 2002, pp. 1455–1457.

[45] K. L. F. Bane, “The short range resistive wall wakefields,” 1991, sLAC/AP-87.

[46] O. Henry and O. Napoly, “The resistive-pipe wake potentials for short bunches,” 1991, cLIC Note 142.

[47] N. Mounet, “The LHC transverse coupled-bunch instability,” Ph.D. dissertation, EPFL, 2012, thesis No 5305.

[48] H. Tsutsui, “Resistive wall impedance of an LHC collimator,” 2003, LHC Project Note 318.

[49] R. L. Gluckstern and B. Zotter. Transverse impedance of a resistive cylinder of finite length. Technical Report CERN-AB-Note-2008-045, CERN, Geneva, Jul 2008.

[50] S. Krinsky, B. Podobedov, and R. L. Gluckstern. Impedance of finite length resistive cylinder. Phys. Rev. ST Accel. Beams, 7:114401, Nov 2004.

[51] G. Stupakov. Resistive wall impedance of an insert. Phys. Rev. ST Accel. Beams, 8:044401, Apr 2005.

[52] Y. Shobuda, Y. H. Chin, and K. Takata. Coupling impedances of a resistive insert in a vacuum chamber. Phys. Rev. ST Accel. Beams, 12:094401, Sep 2009.

[53] Y. Shobuda, Y. H. Chin, and K. Takata. Impedance of a ceramic break and its resonance structures. Phys. Rev. ST Accel. Beams, 17:091001, Sep 2014.

[54] V. G. Vaccaro, “Longitudinal Instability of a Coasting Beam above Transition, due to the action of Lumped Discontinuities,” CERN report ISR-RF/66-35, Tech. Rep., 1966.

[55] V. Balakin, I. Koop, A. Novokhatsky, A. Skrinsky, and V. Smirnov, “Beam Dynamics of a Colliding Linear Electron-Positron Beam (VLEPP),” Tech. Rep. SLAC Trans 188, 1978.

[56] T. Weiland, “Transient Electromagnetic Fields Excited by Bunches of Charged Particles in Cavities of Arbitrary Shape,” CERN ISR-TH/80-24, Tech. Rep., 1980.

[57] K. L. F. Bane, P. B. Wilson, and T. Weiland, “Wake Fields and Wake Field Acceleration,” SLAC-PUB-3528, Tech. Rep. December 1984.

[58] K. L. F. Bane and T. Weiland, “Wake Force Computation in the Time Domain for long Structures,” SLAC-PUB-3173, Tech. Rep., 1983.

[59] K. Yee, “Numerical solution of initial boundary value problems involving Maxwell’s equations in isotropic media,” Antennas and Propagation, IEEE Transactions on, vol. 14, no. 3, pp. 302–307, 1966.

[60] T. Weiland, “A discretization method for the solution of Maxwells equations for six-component fields,” Electronics and Communication (AEU¨), vol. 31, pp. 116–120, 1977.

[61] H. Kawaguchi and T. Honma, “On the wake fields reaction force which acts on electrons in an accelerator cavity,” Nucl. Instrum. Meth. Section A, vol. 363, no. 12, pp. 145–152, 1995. [Online]. Available: http://www.sciencedirect.com/science/article/pii/0168900295003649.

[62] K. Fujita, H. Kawaguchi, I. Zagorodnov, and T. Weiland, “Time domain wake field computation with boundary element method,” IEEE Trans. Nuclear Science, vol. 53, no. 2, 2006.

[63] K. Fujita, H. Kawaguchi, and S. Nishiyama, “Scattered-Field Time Domain Boundary Element Method and Its Application to Transient Electromagnetic Field Simulation in,” IEICE Trans. Electron., vol. 90, no. 2, pp. 265–274, 2007.

[64] E. Gjonaj, T. Lau, T. Weiland, and D. Darmstadt, “Wakefield Computations with the PBCI Code using a Non-Split finite Volume Method,” in PAC 2009, 2009.

[65] P. Thoma, “Zur numerischen L¨osung der Maxwellschen Gleichungen im Zeitbereich,” Ph.D. dissertation, TU-Darmstadt, 1997.

[66] R. Courant, K. Friedrichs, and H. Lewy, “U¨ ber die partiellen Differenzengleichungen der mathematischen Physik,” Mathematische Annalen, vol. 100, no. 1, pp. 32–74, 1928.

[67] I. Zagorodnov and T. Weiland, “TE/TM field solver for particle beam simulations without numerical Cherenkov radiation,” Physical Review Special Topics - Accelerators and Beams, vol. 8, no. 4, p. 042001, Apr. 2005.

[68] E. Gjonaj and T. Weiland, Impedance Calculation, Time Domain, Handbook of Accelerator Physics and Engineering, 2nd ed., A. Chao, K. H. Mess, M. Tigner, and F. Zimmermann, Eds. World Scientific Publishing Co. Pte. Ltd., 2013.

[69] E. Gjonaj, X. Dong, R. Hampel, M. K¨arkk¨ainen, T. Lau, W. F. O. Müller, T. Weiland, T. U. Darmstadt, and T. Elektromagnetischer, “Large Scale Parallel Wake Field Computations for 3D- Accelerator Structures With the PBCI Code,” in ICAP, 2006, pp. 29–34.

[70] B. Krietenstein, R. Schuhmann, P. Thoma, and T. Weiland, “The Perfect Boundary Approximation Technique Facing the Big Challenge of High Precision Field Computation,” in LINAC, Chicago, 1998.

[71] R. L. Gluckstern and S. S. Kurennoy, Impedance Calculation, Frequency Domain, Handbook of Accelerator Physica and Engineering, 2nd ed., A. Chao, K. H. Mess, M. Tigner, and F. Zimmermann, Eds. World Scientific Publishing Co. Pte. Ltd., 2013.

[72] E. Gjonaj, T. Lau, and T. Weiland, “Computation of Short Range Wake Fields with PBCI,” ICFA Beam Dynamics Newsletter, no. 37, 2005.

[73] W. K. H. Panofsky and W. A.Wenzel, “Some Considerations Concerning the Transverse Deflection of Charged Particles in Radio Frequency Fields,” Review of Scientific Instruments Volume 27, no. May 2011, pp. 967–968, 1956.

[74] T. Weiland and R. Wanzenberg, Wake Fields and Impedances. CERN Accelerator School (CCAS), 1993.

[75] T. Weiland, “Comment on Wake Field Computation in the Time Domain,” NIM, vol. 216, pp. 31–34, 1983.

[76] O. Napoly, “The Wake Potentials from the Fields on the Cavity Boundary,” Particle Accelerators, vol. 36, pp. 15–23, 1991.

[77] O. Napoly, Y. H. Chin, and B. Zotter, “A generalized method for calculating wake potentials,” Nucl. Instrum. Meth. Section A, vol. 334, no. 2-3, pp. 255–265, Oct. 1993.

[78] H. Henke and W. Bruns, “Calculation of Wake Potentials in general 3D structures,” in Proc. of ECAP, no. 8, 2006, pp. 2170–2172.

[79] X. Dong, E. Gjonaj, W. F. O. Mueller, and T. Weiland, “Mode Expansion Method in the Indirect Calculation of Wake Potential in 3D Structures,” pp. 148–151, 2006.

[80] I. Zagorodnov, “Indirect methods for wake potential integration,” Physical Review Special Topics - Accelerators and Beams, vol. 9, no. 10, p. 102002, Oct. 2006.

[81] M. Balk, “Feldsimulationen starrer Teilchenstrahlen beliebiger Geschwindigkeit und deren Anwendung in der Schwerionenbeschleunigerphysik,” Ph.D. dissertation, TU-Darmstadt, Cuvillier Verlag Göttingen, 2005.

[82] M. Balk, R. Schuhmann, and T. Weiland, “Open boundaries for particle beams within fit-simulations,” Nucl. Instrum. Meth. Section A, vol. 558, no. 1, pp. 54–57, Mar. 2006.

[83] T. Weiland, “On the unique numerical solution of Maxwellian Eigenvalue Problems in Three Dimensions,” Particle Accelerators, vol. 17, pp. 227–242, 1985.

[84] W. Ackermann and T. Weiland, “High precision cavity simulations,” in Proceedings of the 11th International Computational Accelerator Physics Conference, Rostock, 2012, pp. 1–5.

[85] K. Klopfer, W. Ackermann, and T. Weiland, “Computation of Complex Eigenmodes for Resonators Filled With Gyrotropic Materials,” IEEE Transactions on Magnetics, vol. 51, no. 1, 2015.

[86] U. V. Rienen and T. Weiland, “Impedance Calculation above Cut-Off with URMEL-I,” in EPAC, 1988.

[87] B. Doliwa, E. Arevalo, and T. Weiland, “Numerical calculation of transverse coupling impedances: Comparison to Spallation Neutron Source extraction kicker measurements,” Physical Review Special Topics - Accelerators and Beams, vol. 10, p. 102001, 2007.

[88] U. Niedermayer and O. Boine-Frankenheim, “Numerical Calculation of Beam Coupling Impedances in the Frequency Domain using FIT,” in Proc. of ICAP 2012, Rostock, 2012.

[89] H. Hahn, “Matrix solution for the wall impedance of infinitely long multilayer circular beam tubes,” Physical Review Special Topics - Accelerators and Beams, vol. 13, no. 1, p. 012002, Jan. 2010. [Online]. Available: http://link.aps.org/doi/10.1103/PhysRevSTAB.13.012002

[90] U. Niedermayer and O. Boine-Frankenheim, “Analytical and numerical calculations of resistive wall impedances for thin beam pipe structures at low frequencies,” Nucl. Instrum. Meth. Section A, vol. 687, pp. 51–61, 2012.

[91] B. Doliwa, H. De Gersem, T. Weiland, and T. Boonen, “Optimised electromagnetic 3D field solver for frequencies below the first resonance,” IET Sci. Meas. Technol., pp. 53–56, 2007.

[92] U. Niedermayer, O. Boine-Frankenheim, and H. De Gersem, “Space charge and resistive wall impedance computation in the frequency domain using the finite element method,” Physical Review Special Topics - Accelerators and Beams, vol. 18, no. 3, pp. 1–10, 2015.

[93] A. Macridin, P. Spentzouris, and J. Amundson, “Nonperturbative algorithm for the resistive wall impedance of general cross-section beam

pipes," Physical Review Special Topics - Accelerators and Beams, vol. 16, no. 12, p. 121001, Dec. 2013.

[94] A. Hofmann et al. (1985, October). The ISR Impedance between 40 kHz and 40 GHz. IEEE Transactions on Nuclear Science, Vol. A&32. No. 5. October 1985.

[95] D. Möhl (1974), Equipment Responsible for Transverse Beam Instability in the PS, CERN MPS/DL/Note 74-6.

[96] R. Cappi (1995), Observations of High-Order Head-Tail Instabilities at the CERN-PS, CERN/PS 95-02 (PA).

[97] S. Persichelli (2015, February), The beam coupling impedance model of CERN Proton Synchrotron, PhD thesis, University of Rome la Sapienza, Dipartimento di Scienze di Base e Applicate per l'Ingegneria.

[98] C. Zannini et al (2015, May), Transverse Impedance Model of the CERN PSB, Presented at the 6th International Particle Accelerator Conference, Richmond, VA, USA.

[99] P. Collier et al (1997, March), The SPS as injector for LHC: a conceptual design, CERN report, CERN-SL-97-07-DI.

[100] B. Salvant (2010, March), Impedance Model of the CERN SPS and aspects of LHC Single Bunch Stability, EPFL PhD thesis 4585.

[101] C. Zannini et al (2015, May), Benchmarking the CERN-SPS Transverse Impedance Model with Measured Headtail Growth Rates, Presented at the 6th International Particle Accelerator Conference, Richmond, VA, USA.

[102] J.E. Varela et al (2015, May), An Extended SPS Longitudinal Impedance Model, Presented at the 6th International Particle Accelerator Conference, Richmond, VA, USA.

[103] D. Brandt et al (May 1993) Presented at 15th IEEE Particle Accelerator Conference, Washington, DC, USA, pp.3429-3431.

[104] O. Brüning (1997, May), An Impedance Database program for LEP2 and the LHC, Presented at 19th IEEE Particle Accelerator Conference, Vancouver, BC, Canada.

[105] N. Mounet (2012, January), The LHC Transverse Coupled Bunch Instability, EPFL PhD thesis 5305.

[106] S. Peggs et al (June 1994), An Impedance Model of the Relativistic Heavy Ion Collider, RHIC, Presented at the 4th European Particle Accelerator Conference, London, UK, pp.1102.

[107] Fermilab report (1998), "Run II Handbook", p. 6.58, http://www-bd.fnal.gov/lug/runII_handbook/.

[108] F. Gallucio (1994, December), The impedance budget of HERA-p: a preliminary selection of contributing elements, Internal Report DESY M-94-10.

[109] Y. H. Chin and K. Satoh, Impedance Budget for the KEK B-Factory (1995, May), Presented at the 18th IEEE Particle Accelerator Conference, Dallas, TX, USA.

[110] A. Blednykh, and S. Krinsky (2007, June), Preliminary Impedance Budget for NSLS-II Storage Ring, BNL report BNL-79153-2007-CP.

[111] R. Wanzenberg et al (2005, May), The Impedance of Selected Components of the Synchrotron Light Source Petra III, Presented at the 21st IEEE Particle Accelerator Conference, Knoxville, TN, USA.

[112] R. Nagaoka (2004, July), Numerical Evaluation of Geometric impedance for SOLEIL, Presented at the European Particle Accelerator Conference, Lucerne, Switzerland.

[113] T. Gunzel et al (2008), Impedance and Instabilities for the ALBA Storage Ring, Presented at the European Particle Accelerator Conference, Genova, Italy.

[114] Handbook of Accelerator Physics and Engineering (1999), 3rd edition, Edited by: A. W. Chao and M. Tigner.

[115] B. Podobedov and S. Krinsky (2007), Transverse impedance of tapered transitions with elliptical cross section, Phys. Rev. ST Accel. Beams 10, 074402.

[116] Y. H. Chin, ABCI home page, http://abci.kek.jp/abci.htm.

[117] ACE3P simulation suite webiste SLAC, https://confluence.slac.stanford.edu/display/AdvComp/ACE3P+-+Advanced+Computational+Electromagnetic+Simulation+Suite.

[118] TE/TM field solver for particle beam simulations without numerical Cherenkov radiation (2005) I.A. Zagorodnov and T. Weiland,Phys. Rev. ST Accel.Beams8, 042001.

[119] GdfidL, http://www.gdfidl.de/.

[120] A. Mostacci and F. Caspers (2014, April), History and development of bench measurement techniques for impedance evaluation, Presented at the ICFA mini-Workshop on Electromagnetic wake fields and impedances in particle accelerators.

[121] B. Podobedov and G. Stupakov (2013, February), Point-charge wakefield calculations from finite length bunch wake potentials, Phys. Rev. ST Accel. Beams 024401.

[122] Computational electrodynamics - State of the art and future (2014, April), T. Weiland, Presented at the ICFA mini-Workshop on Electromagnetic wake fields and impedances in particle accelerators.

[123] LHC Design Report, v.1: the LHC Main Ring (2004), CERN-2004-003-V-1.

[124] E. Métral et al., "Beam-Induced Heating / Bunch Length / RF and Lessons for 2012", Proc. of the LHC Performance workshop, Chamonix, France, 06-10/02/2012.

[125] E. Métral, RF Heating from Wake Losses in Diagnostics Structures, Proc. of IBIC'13, Oxford, UK, 16-19/09/2013.

[126] B. Salvant et al., "Beam Induced RF Heating", Proc. of the LHC Beam Operation workshop, Evian, France, 17-20/12/2012.

[127] M. Furman et al., "Energy Loss of Bunched Beams in SSC RF Cavities", SSC-116, March 1987.

[128] E. Métral et al., "Lessons Learnt and Mitigation Measures for the CERN LHC Equipment with RF Fingers", Proc. of the IPAC'13 conference, Shanghai, China, 12-17 May, 2013.

[129] E. Métral and C. Zannini, "Temperature Effects on Image Current Losses in the HL-LHC Triplets, - Part 2", CERN HL-LHC WP2 Task Leaders meeting, 05/09/2014.

[130] E.D. Courant and A.M. Sessler, Transverse Coherent Resistive Instabilities of Azimuthally Bunched Beams in Particle Accelerators, R.S.I, 37(11), 1579-1588, 1966.

[131] C. Pellegrini, Nuovo Cimento, 64°, 477, 1969.

[132] M. Sands, The Head-Tail Effect: an Instability Mechanism in Storage Rings, SLAC-TN-69-8, 1969.

[133] M. Sands, Head-Tail Effect II: From a Resistive-Wall Wake, SLAC-TN-69-10, 1969.

[134] F. Sacherer, Single beam collective phenomena-transverse (bunched beams), Proc. First Course Int. School on Accelerators, Erice, 1976: Theoretical Aspects of the Behaviour of Beams in Accelerators and Storage Rings, CERN 77-13, p. 210, 1977

[135] J.L. Laclare, Bunched Beam Coherent Instabilities, CERN Accelerator School, Oxford, CERN 87-03, p. 264, 1987.

[136] K.W. Robinson, Cambridge Electron Accel. Report CEAL-1010 (1964).

[137] J.L. Laclare, Introduction to Coherent Instabilities – Coasting Beam Case, CERN Accelerator School: General Accelerator Physics, CERN 85-19, Vol. II, p. 377, 1985.

[138] E. Keil and W. Schnell, CERN Report ISR-TH-RF/69-48, 1969.

[139] D. Boussard, Observation of Microwave Longitudinal Instabilities in the CPS, CERN Report LabII/RF/Int./75-2, 1975.

[140] F.J. Sacherer, Bunch Lengthening and Microwave Instability, IEEE Trans. Nucl. Sci., Vol. NS-24, No. 3, June 1977.

[141] K. Ng, Potential-Well Distortion and Mode-Mixing Instability in Proton Machines, FERMILAB-FN-630, 1995.

[142] E. Métral, Stability Criterion for the Longitudinal Mode-Coupling Instability in the Presence of Both Space-Charge and Resonator Impedances, CERN/PS 2001-063 (AE), 2001.

[143] E. Shaposhnikova, Signatures of Microwave Instability, CERN-SL-99-008 HRF, 1999.

[144] J.S. Berg and R.D. Ruth, Transverse Instabilities for Multiple Nonrigid Bunches in a Storage Ring, Physical Review E, Vol. 52, N. 3, September 1995.

[145] H. Hereward, Rutherford Lab. Reports RL-74-062, EPIC/MC/48 (1974), and RL-75-021, EPIC/MC/70 (1975). See also B. Chen and A. W. Chao, SSCL Report 606 (1992).

[146] D. Boussard and T. Linnecar, Proc. 2nd Euro. Part. Accel. Conf , Nice, 1990, p. 1560.

[147] R.D. Kohaupt, Head Tail Turbulence and the Transverse PETRA Instability, DESY 80/22, 1980.

[148] E. Métral, Stability Criteria for High-Intensity Single-Bunch Beams in Synchrotrons, Proc. 8th EPAC, Paris, France, 3-7 June 2002.

[149] Y.H.Chin and K. Satoh, "Transverse mode coupling in a bunched beam", IEEE Trans. Nucl. Sci., No 4, 2566 (1983) and Nucl. Instrum. Methods 207, 309(1983).

[150] G. Rumolo and F. Zimmermann, Practical user guide for HEADTAIL, CERN-SL-Note-2002-036-AP, 2002.

[151] B. Salvant, Impedance Model of the CERN SPS and Aspects of LHC Single-Bunch Stability, PHD Thesis, Ecole Polytechnique Fédérale de Lausanne (Switzerland), 2010.

[152] E. Métral and G. Rumolo, Simulation Study on the Beneficial Effect of Linear Coupling for the Transverse Mode Coupling Instability in the CERN Super Proton Synchrotron, Proc. Of EPAC 2006, Edinburgh, UK, 26-30 June 2006.

[153] S. Myers, LEP Note 436, 1983.

[154] R. Ruth, CERN LEP-TH/83-22, 1983.

[155] R. Ruth, Proc. of the 12th Inter. Conf. on High Energy Accelerators, Fermilab, Batavia, August 11-16, 1983, p. 389.

[156] S. Myers, J. Vancraeynest, CERN LEP-RF/84-13, 1984.

[157] S. Myers, CERN LEP-RF/85-22, 1985.

[158] S. Myers, Proc. of the IEEE PAC, Washington D.C., March 16, 1987, p. 503-507.

[159] M. Karliner, K. Popov, Theory of a Feedback to Cure Transverse Mode Coupling Instability, NIM A537 (2005), p. 481-500.

[160] H.G. Hereward, Landau Damping by Non-Linearity, CERN/MPS/DL 69-11, 1969.

[161] S. Nagaitsev et al., Nonlinear Optics as a Path to High-Intensity Circular Machines, Proc. of ICFA HB2010, Morschach, Switzerland, Sept. 27 – Oct. 1, 2010.

[162] E. Métral, Theory of Coupled Landau Damping, Part. Accelerators, 62(3-4), p. 259, 1999.

[163] E. Métral et al., Destabilising Effect of Linear Coupling in the HERA Proton Ring, Proc. of 8th EPAC, Paris, France, 3-7 June 2002.

[164] E. Métral, Simple Theory of Emittance Sharing and Exchange due to Linear Betatron Coupling, CERN/PS 2001-066 (AE), December 2001.

[165] A. Franchi, E. Métral and R. Tomás, Emittance Sharing and Exchange Driven by Linear Betatron Coupling in Circular Accelerators, Phys. Rev. ST Accel. Beams 10, 064003 (2007).

[166] T. P. R. Linnecar, E. Shaposhnikova, Microwave instability and impedance measurements in the CERN SPS, Part. Accel. 58, p.241-255, 1997.

[167] J. M. Wang and C. Pellegrini, On the condition for a single bunch high frequency fast blow-Up, Proc.XI Int. Conf. on H.E.Ac, p.554, 1980.

[168] BLonD - Beam Longitudinal Dynamics code, http://blond.web.cern.ch/.

[169] A. Burov, Van Kampen modes for bunch longitudinal motion, Proc. HB2010, Morschach, Switzerland, 2010 and Dancing bunches as van Kampen modes, Proc. PAC'11, New York, NY, USA, 2011.

[170] T. Argyropoulos, A. Burov. E. Shaposhnikova, Loss of Landau damping for inductive impedance in a double RF system, IPAC'13, Shanghai, China, May 2013.

[171] V. I. Balbekov, S. V. Ivanov, Methods for suppressing the longitudinal instability of a bunched beam with the help of landau damping, Atomnaya Energiya, 62 (2), p.117-125, 1987.

[172] E. Shaposhnikova, Bunched beam transfer matrices in single and double rf systems, CERN-SL-94-19. CERN-SL-94-19-RF, 1994.

[173] A. Blas, S. Koscielniak, F. Pedersen, Explanation of Sextupole Instability in CERN PS Booster, EPAC98, Stockholm, Sweden, Jun., p.969-971, 1998.

[174] E. Shaposhnikova, T. Bohl, T. Linnecar, Beam transfer functions and beam stabilisation in a double RF system, Proc. PAC'05, Knoxville TN, USA, May, 2005.

[175] T. P. Linnecar, E. Shaposhnikova, Analysis of the voltage programs for the SppS double frequency RF system, SL-Note-92-44-RFS, Feb, 1992.

[176] N. Matsunaga and T. Yamamoto, Journal of Computational and Applied Mathematics 116 – 2000, pp. 263–273.

[177] G. Iadarola, "Electron cloud studies for CERN particle accelerators and simulation code development", CERN-THESIS-2014-047 - 203 p.

[178] F. M. Mako and P. Weilhammer, "A High-Current Micro-Pulse Electron Gun," Proceedings of the 15th IEEE Particle Accelerator Conference, Washington, DC, USA, , 1993.

[179] J. Vaughan, "Multipactor," Electron Devices, IEEE Transactions on, vol. 35, no. 7, pp. 1172–1180, Jul 1988.

[180] R. A. Kishek, Y. Y. Lau, L. K. Ang, A. Valfells, and R. M. Gilgenbach, "Multipactor discharge on metals and dielectrics: Historical review and recent theories," Physics of Plasmas (1994- present), vol. 5, no. 5, pp. 2120–2126, 1998. [Online]. Available: http://scitation.aip.org/content/aip/journal/pop/5/5/10.1063/1.872883.

[181] A.Woode and J. Petit, "Investigations into multipactor breakdown in satellite microwave payloads," ESA Journal, vol. 14, pp. 467–478, 1990.

[182] "Proceedings of ECLOUD'02: Mini Workshop on Electron Cloud Simulations for Proton and Positron Beams, Geneva, Switzerland, edited by G.Rumolo and F.Zimmermann," CERN-2002-001, 2002.

[183] "Proceedings of ECLOUD'04: 31st Advanced ICFA Beam Dynamics Workshop on Electron-Cloud Effects, Napa, CA, USA , edited by M. Furman, S. Henderson and F. Zimmermann," CERN-2005- 001, 2005.

[184] "Proceedings of ECLOUD'07: International Workshop on Electron Cloud Effects, Ithaca, New York, edited by H. Fukuma, E. S.Kim and K. Ohmi," 2007.

[185] "Proceedings of ECLOUD'10: ICFA Advanced Beam Dynamics Workshop on electron cloud physics, Ithaca, New York, edited by K. Smolenski," 2010.

[186] "Proceedings of ECLOUD'12: Joint INFN-CERN-EuCARDAccNet Workshop on Electron-Cloud Effects, La Biodola, Isola d'Elba, Italy, edited by R. Cimino, G.Rumolo and F.Zimmermann," CERN-2013-02, 2013.

[187] W. Fischer, M. Blaskiewicz, J. Brennan, H. Huang, H.-C. Hseuh, V. Ptitsyn, T. Roser, P. Thieberger, D. Trbojevic, J. Wei, S. Y. Zhang, and U. Iriso, "Electron cloud observations and cures in the relativistic heavy ion collider," Physical Review Special Topics- Accelerators and Beams, vol. 11, no. 4, p. 041002, 2008.

[188] H. Fukuma, "Electron Cloud Observations and Predictions at KEKB, PEP-II and SuperB Factories," Proceedings of ECLOUD12: Joint INFN-CERN-EuCARD-AccNet Workshop on Electron-Cloud Effects, La Biodola, Isola d'Elba, Italy, 2012.

[189] M. Zobov, D. Alesini, A. Drago, A. Gallo, S. Guiducci, C. Milardi, A. Stella, S. De Santis, T. Demma, and P. Raimondi, "Operating experience with electron cloud clearing electrodes at DAFNE," Proceedings of ECLOUD12: Joint INFN-CERN-EuCARD-AccNet Workshop on Electron-Cloud Effects, La Biodola, Isola d'Elba, Italy, 2012.

[190] G. Iadarola, "Electron cloud studies for CERN particle accelerators and simulation code development," CERN-THESIS-2014 047, 2014.

[191] G. Rumolo, F. Ruggiero, and F. Zimmermann, "Simulation of the electron-cloud build up and its consequences on heat load, beam stability, and diagnostics," Phys. Rev. ST Accel. Beams, vol. 4, p. 012801, Jan 2001. [Online]. Available: http://link.aps.org/doi/10.1103/PhysRevSTAB.4.012801.

[192] A. Chao, Physics of Collective Beam Instabilities in High Energy Accelerators, ser. Wiley Series in Beam Physics and Accelerator Technology. Wiley, 1993. [Online]. Available: http://books.google.fr/books?id=MjRoQgAACAAJ.

[193] K. Li and G. Rumolo, "Review of Beam Instabilities in the Presence of Electron Clouds in the LHC," Proceedings of the IPAC11 International Particle Accelerator Conference, San Sebastian, Spain, 2011.

[194] K. Li, H. Bartosik, X. Buffat, W. H¨ofle, G. Iadarola, M. Kuhn, N. Mounet, and G. Rumolo, "LHC injection instabilities," Presentation at 2-day internal review of LHC performance limitations during run I, 25-26. September 2013, CERN.

[195] G. Bregliozzi, G. Lanza, V. Baglin, and J. M. Jimenez, "Vaccum Pressure Observations during 2011 Proton Run," Proceedings of the Evian 2011 LHC Beam Operation Workshop, Evian, France, 2011.

[196] L. Tavian, "Performance Limitations of the LHC Cryogenics: 2012 Review and 2015 Outlook," Proceedings of the Evian 2012 LHC Beam Operation Workshop, Evian, France, 2012.

[197] W. H¨ofle, "Observations of the electron cloud effect on pickup signals in the SPS," 10th Workshop on LEP-SPS Performance, Chamonix, France, 2000.

[198] F. Zimmermann, "A Simulation Study of Electron-Cloud Instability and Beam-Induced Multipacting in the LHC," LHC Project Report 95, 1997.

[199] F. Zimmermann, "Electron Cloud Simulations for SPS and LHC," Proceedings of the Chamonix X LHC workshop, Chamonix, France, 2000.

[200] G. H. Shortley and R. Weller, "The Numerical Solution of Laplace's Equation," Journal of Applied Physics, vol. 9, no. 5, pp. 334–348, 1938. [Online]. Available: http://scitation.aip.org/content/aip/journal/jap/9/5/10.1063/1.1710426.

[201] M. G. Billing, J. Conway, E. E. Cowan, J. A. Crittenden, W. Hartung, J. Lanzoni, Y. Li, C. S. Shill, J. P. Sikora, and K. G. Sonnad, "Measurement of electron trapping in the Cornell Electron Storage Ring," Phys. Rev. ST Accel. JOURNAL 5 Beams, vol. 18, p. 041001, Apr 2015. [Online]. Available: http://link.aps.org/doi/10.1103/PhysRevSTAB.18.041001.

[202] H. Qin, S. Zhang, J. Xiao, J. Liu, Y. Sun, and W. M. Tang, "Why is boris algorithm so good?" Physics of Plasmas (1994-present), vol. 20, no. 8, pp. –, 2013. [Online]. Available: http://scitation.aip.org/content/aip/journal/pop/20/8/10.1063/1.4818428

[203] G. Iadarola and G. Rumolo, "Electron cloud in the CERN accelerators (PS, SPS, LHC)," Proceedings of ECLOUD12: Joint INFN-CERNEuCARD-AccNetWorkshop on Electron-Cloud Effects, La Biodola, Isola d'Elba, Italy, 2012.

[204] G. Maury Cuna, G. Rumolo, F. Zimmermann, and G. Iadarola, "Simulation of electron-cloud heat load for the cold arcs of the Large Hadron Collider," Proceedings of the IPAC12 International Particle Accelerator Conference, New Orleans, USA, 2012.

[205] F. Caspers, S. Gilardoni, E. Mahner, G. Rumolo, C. Yin Vallgren, and G. Iadarola, "Comparison between electron cloud build-up measurements and simulations at the cern ps," Proceedings of the IPAC12 International Particle Accelerator Conference, New Orleans, USA, 2012.

[206] C. M. Bhat, H. Damerau, S. Hancock, E. Mahner, F. Caspers, G. Iadarola, T. Argyropoulos, and F. Zimmermann, "Dependence of e-cloud on the longitudinal bunch profile: studies in the PS & extension to the HL-LHC,"

Proceedings of ECLOUD12: Joint INFN-CERN-EuCARD-AccNet Workshop on Electron-Cloud Effects, La Biodola, Isola d'Elba, Italy, 2012.

[207] H. Bartosik, W. H¨ofle, G. Iadarola, Y. Papaphilippou, and G. Rumolo, "Benchmarking HEADTAIL with electron cloud instabilities observed in the LHC," Proceedings of ECLOUD12: Joint INFN-CERN-EuCARD-AccNet Workshop on Electron-Cloud Effects, La Biodola, Isola d'Elba, Italy, 2012.

[208] H. Bartosik, "Beam dynamics and optics studies for the LHC injectors upgrade", PhD thesis, CERN-THESIS-2013-257, CERN, Geneva, Switzerland, 2013.

[209] B. Salvant et al., "Probing intensity limits of LHC-type bunches in SPS with nominal optics", in Proceedings of the International Particle Accelerator Conference IPAC11, San Sebastian, Spain, 2011.

[210] C. Zannini, "Electromagnetic Simulation of CERN accelerator Components and Experimental Applications", PhD thesis, CERN-THESIS-2013-076, CERN, Geneva, Switzerland, 2013.

[211] C. Zannini et al., "Effect of the TEM mode on the kicker impedance", IPAC12, New Orleans, USA, 2012.

[212] B. Salvant et al., "Update of the SPS Impedance Model", IPAC10, Kyoto, Japan, 2010.

[213] C. Zannini, "SPS: impedance model and instability in the transverse plane, "Presented at the LIU day 2014, https://indico.cern.ch/event/299470/.

[214] C. Zannini, "Benchmarking the SPS impedance model: Headtail growth rates, "Presented at the CERN SPS Upgrade Working Group, http://pafspsu.web.cern.ch/ (2014).

[215] LHC injectors upgrade, Technical Design Report, Vol.I: Protons, edited by J. Coupard et al., CERN-ACC-2014-0337 (CERN, Geneva, 2014).

[216] T. Argyropoulos, E. Shaposhnikova, J. E. Varela, Proc. of LHC performance workshop Chamonix 2014.

[217] J. E. Varela, Longitudinal impedance charecterization of the CERN SPS vacuum flanges, Proc. of IPAC2015, Richmond, USA (2015).

[218] E. Shaposhnikova et al., Identification of high-frequency resonant impedance in the CERN SPS, Proc. of IPAC2014, Dresden, Germany (2014).

[219] T. Argyropoulos, Longitudinal microwave instability in a multi-RF system, Proc. of HB2014, East-Lansing, MI, USA (2014).

[220] E. Shaposhnikova, Longitudinal stability of the LHC beam in the SPS, CERN SL-Note-2001-031 HRF, 2001.

[221] T. Argyropoulos et al., Controlled longitudinal emittance blow-up in double harmonic RF system at CERN SPS, Proc. of HB2010, Morschach, Switzerland (2010).

[222] F. J. Sacherer, A longitudinal stability criterion for bunched beams, IEEE Trans. Nucl. Sci. NS-20, p. 825, 1973.

[223] LHC Design Report, v.1: the LHC Main Ring (2004), CERN-2004-003-V-1 (chapter 5, p.101).

[224] E. Shaposhnikova et al., "Loss of Landau Damping in the LHC," in IPAC'11, San Sebastian, Spain (2011).

[225] E. Shaposhnikova, "Longitudinal beam parameters during acceleration in the LHC," LHC-PROJECT-NOTE-242 (2000).

[226] V. I. Balbekov and S. V. Ivanov, "Thresholds of Longitudinal Instability of Bunched Beam in the Presence of Dominant Inductive Impedance," IHEP Preprint 91-14 (1991).

[227] F. J. Sacherer et al., "A Longitudinal Stability Criterion for Bunched Beams," IEEE Trans. Nucl. Sci. NS-20, p.825 (1973).

[228] J. F. Esteban Müller et al., "Beam Measurements of the LHC Impedance and Validation of the Impedance Model," in IPAC'14, Dresden, Germany (2014).

[229] E. Shaposhnikova, T. Bohl, and T. Linnecar, "Longitudinal peak detected Schottky spectrum," HB2010, Morschach, Switzerland (2010).

[230] E. Shaposhnikova et al., "Flat bunches in the LHC," in IPAC'14, Dresden, Germany (2014).

[231] J. F. Esteban Müller et al., "High-accuracy Diagnostic Tool for Electron Cloud Observation in the LHC based on Synchronous Phase Measurements," in IPAC'14, Dresden, Germany (2014).

[232] J. F. Esteban Müller et al., "Measurements of the LHC longitudinal resistive impedance with beam," HB2012, Beijing (2012).

[233] J. Qiang, M.A. Furman, R.D. Ryne, "A parallel particle-in-cell model for beam–beam interaction in high energy ring colliders", Journal of Comp. Phys., 198, pp. 278–294 (2004).

[234] A. Burov, "Nested Head-Tail Vlasov Solver", CERN AP Forum talk, CERN, Dec. 4, 2012; A. Burov, "Beam-beam, impedance and damper", ICFA Beam-Beam workshop, CERN, March 19, 2013; A. Burov, "Interplay of collective effects and beam-beam", Joint LARP CM20/HiLumi Meeting, April 10, 2013, Napa Valley, CA.

[235] J.S. Berg, F. Ruggiero, "Landau damping with two-dimensional betatron tune spread", CERN-SL-AP-96-071-AP (1996).

[236] S. White, "Update on long-range instabilities", ICE section meeting, CERN, Nov. 7, 2012.

[237] X. Buffat, "Long-range beam-beam contribution to stability diagrams", talk at ICE section meeting, Apr 24, 2013, CERN.

[238] E. Metral, "Review of the instabilities", talk at the LHC Beam Operation Workshop, Evian, 2012.

[239] A. Burov, "ADT suppression of coherent beam-beam", ICE meeting, CERN, Oct. 30, 2012

[240] S. Fartoukh, E. Metral, A. Burov, conclusions of the "Two-Beam Impedance / Cogging" MD, Dec. 2012.

[241] A. Burov, "Three-beam instability in the LHC", FERMILAB-PUB-13-005-AD.

[242] N. Mounet, DELPHI: an analytic Vlasov solver for impedance-driven modes, CERN HSC meeting, 07/05/2014.

[243] B. Zotter, "The equivalent broad-band impedance in LEP: Updated estimates of the current thresholds due to transverse mode-coupling," Tech. Rep. CERN-LEP-TH-87-34, 1987.

[244] G. Sabbi, "Simulation of single-bunch collective effects in LEP by linear expansion of the distribution moments," Tech. Rep. CERN-SL-95-25 (AP), 1995.

[245] J. M. Jowett, "Beam dynamics at LEP," Tech. Rep. CERN/SL/98-029 (AP), 1998.

[246] N. Mounet, 2014, IRIS repository. [Online]. Available: https://git.cern.ch/web/IRIS.git.

[247] M. Blaskiewicz, Phys. Rev. ST Accel. Beams 1, 044201 (1998).

[248] M. Blaskiewicz, Phys. Rev. ST Accel. Beams 6, 014203 (2003).

[249] A. Burov, Phys. Rev. ST Accel. Beams 12, 044202 (2009).

[250] A. Burov, "Damping factors for head-tail modes at strong space charge", http://arxiv.org/abs/1505.07704 (2015).

[251] V. Balbekov, Phys. Rev. ST Accel. Beams 12, 124402 (2009).

[252] V. Kornilov and O. Boine-Frankenheim, Phys. Rev. ST Accel. Beams 13, 114201 (2010).

[253] V. Kornilov, O. Boine-Frankenheim, D.J. Adams, B. Jones, B.G. Pine, C.M. Warsop, R.E. Williamson, "Thresholds of the Head-Tail Instability in Bunches with Space Charge", HB'2014 workshop, East Lansing, MI, USA.

[254] Synergia2, Accelerator Modeling, https://cdcvs.fnal.gov/redmine/projects/synergia2/wiki.

[255] A. Macridin, A. Burov, E. Stern, J. Amundson, and P. Spentzouris, "Simulation of transverse modes with their intrinsic Landau damping for bunched beams in a presence of space charge", to be published.

[256] A. Burov and T. Zolkin, "SChargeV: Vlasov solver for transverse oscillations of bunched beams with strong space charge", presented at the Space–Charge 2015 workshop, Oxford, UK.

[257] T. Zolkin, "Analysis of beam transverse instabilities at Fermilab", IPAC 2015, Richmond, VA, USA.

[258] O.Boine-Frankenheim, V.Kornilov, Proc. of ICAP2006, Chamonix Mont-Blanc, Oct 2-6 (2006).

[259] V. Kornilovand, O. Boine-Frankenheim, Phys. Rev. STAccel. Beams 15, 114201 (2012).

[260] R. Singh, et. al., Phys. Rev. ST Accel. Beams 16, 034201 (2013).

[261] E. Metral, F. Ruggiero, CERN Report CERN-AB-2004-025 (2004).

[262] V. Kornilov, et.al., Proc. of HB2014, East Lansing, USA, November 10-14 (2014).

[263] V. Kornilov, O. Boine-Frankenheim, Space Charge 2015 Workshop, Oxford, March 23-27, https://www.cockcroft.ac.uk/events/SpaceCharge15/index.html (2015).

[264] D. Möhl and H. Schönauer, Landau Damping by Non-Linear Space-Charge Forces and Octupoles, Proc. IX Int. Conf. High Energy Acc., Stanford, 1974 (AEC, Washington, D.C., 1974), [CONF 740522] p. 380.

[265] D. Möhl, On Landau Damping of Dipole Modes by Non-Linear Space Charge and Octupoles, CERN/PS 95-08 (DI), 1995.

[266] D. Neuffer and S. Peggs, "Tune shifts and spreads in the SSC - Headon, long-range and PACMAN conditions," SSC, Tech. Rep. SSC-63, Apr 1986.
JOURNAL OF LATEX CLASS FILES, VOL. 13, NO. 9, SEPTEMBER 2014 5.

[267] A. W. Chao, Lecture notes on special topics in accelerator physics. SLAC-PUB-9574, 2002, ch. 9 Lie Algebra Technique for nonlinear Dynamics.

[268] W. Herr and L. Vos, "Tune distributions and effective tune spread from beam-beam interactions and the consequences for Landau damping in the LHC," CERN, Geneva, Switzerland, Tech. Rep. LHC project note 316, Apr 2003.

[269] X. Buffat, W. Herr, N. Mounet, T. Pieloni, and S. White, "Stability diagrams of colliding beams in the large hadron collider," Phys. Rev. ST Accel. Beams, vol. 17, p. 111002, Nov 2014. [Online]. Available: http://link.aps.org/doi/10.1103/PhysRevSTAB.17.111002.

[270] J. Gareyte, J.-P. Koutchouk, and F. Ruggiero, “Landau damping, dynamic aperture and octupole in LHC,” CERN, Geneva, Switzerland, Tech. Rep. LHC Project Report 91, Feb 1997.

[271] S. Fartoukh, .. The sign of the LHC octupoles, CERN-ACC-SLIDES-2014-0113.

[272] E. Métral et al., Tune spread and stability diagram in the presence of both octupoles and beam beam long range, CERN HSC meeting, 27/08/2014.

[273] X. Buffat, W. Herr, M. Lamont, S. Redaelli, and J. Wenninger, “Squeezing with colliding beams,” in Proceedings of the 2012 Evian workshop on LHC beam operation, B. Goddard and S. Dubourg, Eds., CERN, Geneva, Switzerland, 18-22 March 2013 2012, pp. 27–32.

[274] V. Shiltsev, V. Danilov, D. Finley, and A. Sery, “Considerations on compensation of beam-beam effects in the tevatron with electron beams,” Phys. Rev. ST Accel. Beams, vol. 2, p. 071001, Jul 1999. [Online]. Available: http://link.aps.org/doi/10.1103/PhysRevSTAB.2.071001.

[275] X. Buffat, “Transverse beams stability studies at the large hadron collider,” Ph.D. dissertation, EPFL, 2015.

[276] S. Myers, “A mechanism for beam loss during vertical steering,” CERN, Geneva, Switzerland, Tech. Rep. ISR-RF/SM/ps, 1979.

[277] E. Métral and A. Verdier, “Stability diagram for Landau damping with a beam collimated at an arbitrary number of sigmas,” CERN, Geneva, Switzerland, Tech. Rep. CERN-AB-2004-019-ABP, Feb 2004.

[278] A. Bazzani and L. Beccaceci, “Diffusion in hamiltonian systems driven by harmonic noise,” Journal of Physics A: Mathematical and General, vol. 31, no. 28, p. 5843, 1998. [Online]. Available: http://stacks.iop.org/0305-4470/31/i=28/a=004.

[279] X. Buffat, W. Herr, N. Mounet, and T. Pieloni, “Stability diagram of colliding beams,” in Proceedings of the ICFA Mini-workshop on beambeam effects in hadron colliders, W. Herr and G. Papotti, Eds., CERN, Geneva, Switzerland, 18-22 March 2013 2014, pp. 57–62.

[280] T. Pieloni, D. Banfi, J. Barranco, X. Buffat, N. Mounet, J. Qiang, C. Tambasco, S. White, E. Métral, and G. Arduini, “Two beam effects,” in Proceedings of the 2014 Evian workshop on LHC beam operation, B. Goddard and S. Dubourg, Eds. Geneva, Switzerland: CERN, 2-4 June 2014.

[281] K. Yokoya, “Tune shift of coherent beam-beam oscillations,” Part. Acc., vol. 27, p. 181, 1990.

[282] A. Piwinski, “Observation of beam-beam effects in PETRA,” IEEE Trans.Nucl.Sci., vol. 26, pp. 4268–4270, 1979.

[283] K. Hirata, “Coherent betatron oscillation modes due to beam-beam interaction,” Nucl. Instrum. Meth., vol. A269, p. 7, 1988.

[284] Y. Alexahin, “A study of the coherent beam-beam effect in the framework of the Vlasov perturbation theory,” Nucl. Instrum. Meth., vol. A480, pp. 253–288, 2002.

[285] E. A. Perevedentsev and A. A. Valishev, “Simulation of the head-tail instability of colliding bunches,” Phys. Rev. ST Accel. Beams, vol. 4, p. 024403, 2001.

[286] E. G. Stern, J. F. Amundson, P. G. Spentzouris, and A. A. Valishev, “Fully 3D multiple beam dynamics processes simulation for the Fermilab Tevatron,” Phys. Rev. ST Accel. Beams, vol. 13, p. 024401, 2010.

[287] T. Pieloni, G. Arduini, X. Buffat, R. Giachino, W. Herr, M. Lamont, E. Metral, N. Mounet, G. Papotti, B. Salvant, J.Wenninger, and S. White, “Observations of two-beam instabilities during the 2012 LHC physics run,” IPAC’13 conference proceeding , 2013.

[288] S. White, X. Buffat, N. Mounet, and T. Pieloni, “Transverse mode coupling instability of colliding beams,” Phys. Rev. ST Accel. Beams, vol. 17, p. 041002, 2014.

[289] V. V. Danilov and E. A. Perevedentsev, “Feedback system for elimination of the transverse mode coupling instability,” Nucl. Instrum. Meth., vol. A391, pp. 77–92, 1997.

[290] T. Pieloni, “A study of beam–beam effects in hadron colliders with a large number of bunches,” EPFL PhD Thesis 4211 , 2008.

[291] J. Qiang, M. A. Furman, R. D. Ryne, W. Fischer, and K. Ohmi, “Recent advances in strong-strong beam-beam simulation,” Nucl. Instrum. Meth., vol. A558, pp. 351–355, 2006.

[292] W. Herr, M. Zorzano, and F. Jones, “A hybrid fast multipole method applied to beam-beam collisions in the strong-strong regime,” CERNLHC project report , vol. 466, 2001.

[293] A. Burov, N. Dikansky, “Electron Cloud Instabilities”, Proc. of Int. Workshop on Multibunch Instabilities in Future Electron and Positron Accelerators, Tsukuba, KEK, 1997.

[294] K. Ohmi and F. Zimmermann, “Head-Tail Instability Caused by Electron Clouds in Positron Storage Rings”, Phys. Rev. Lett. 85, 3821–3824, 2000.

[295] K. Ohmi, F. Zimmermann, E. Perevedentsev, “Wake-field and fast head-tail instability caused by an electron cloud”, Phys. Rev. E 65, 016502, 2001.

[296] A. Burov, “Three-beam instability in the LHC”, FERMILAB-PUB-13-005-AD (2013).

[297] A. Burov, “Electron Cloud Instability”, talk given at CERN ICE meeting, Aug. 8 2012.